UNIVERSITY OF NAPLES
“PARTHENOPE”

Department of Engineering

PhD Program in
Energy Science and Engineering
XXXVIII Cycle

Multi-Scale Experimental and System-level Analysis of Solid Oxide Cells: Studies and Applications for Energy Storage Purposes

TUTOR
Chiar.mo Prof
Elio Jannelli

CANDIDATE
Francesco Marino

PhD course coordinator
Prof Laura Vanoli

ABSTRACT

The transition to low-carbon energy systems requires efficient and scalable technologies capable of addressing the challenges of the current global energy scenario. Solid Oxide Cells (SOCs) represent a promising solution for efficient energy conversion and long-duration energy storage. Thanks to their intrinsic properties such as reversibility and high efficiency, SOCs can play a strategic role in the transition toward hydrogen-based and low-carbon energy systems. However, their widespread deployment remains limited by degradation phenomena and by the limited understanding, at a detailed level, of their behavior under realistic operating conditions.
This doctoral research investigates the potential of SOC technology through a multi-scale approach that combines theoretical modeling, simulation of renewable energy integration, and experimental validation. A detailed thermodynamic framework has been developed to describe the electrochemical behavior of the cell, alongside a comprehensive analysis of its materials, design, and main degradation mechanisms.

A few innovative methodologies and experimental studies have been proposed. The first concerns the development of an in-house-built multisampling test bench for localized in-operando characterization of single SOCs. This setup enables simultaneous measurements of gas composition and temperature at eleven points along the fuel electrode surface, providing direct insights into spatial electrochemical and thermal gradients that are typically inaccessible through conventional inlet-outlet analysis. The resulting chemical and thermal mappings reveal non-uniform reaction kinetics along the electrode, identifying high-activity zones near the inlet and highlighting the influence of fuel utilization and steam conversion on local performance and degradation. A coupled modeling study was then conducted to verify the correlation between experimental and simulated data, allowing the estimation of key local parameters such as current density and cell voltage from the measured gas composition profiles.

The second experimental activity focuses on a short-stack campaign performed on a 15-cell SOC stack operated with various fuel mixtures representative of current and future gas-grid scenarios. The results demonstrate the fuel flexibility of SOC technology, capable of efficient operation with pure hydrogen, natural gas, or intermediate blends. Formulations of electrical and thermal efficiency are proposed and compared, establishing harmonized criteria for the evaluation of stack and system performance under different operating regimes.

At system-level, a reversible SOC (rSOC) was coupled with a photovoltaic (PV) installation and a residential energy load to assess its suitability for seasonal storage applications. The cell was tested dynamically under variable power input and output, simulating the real behavior of a domestic renewable energy system. The test campaign was designed to accurately reproduce, at laboratory scale, the load fluctuations experienced by a real rSOC stack. The results demonstrated excellent responsiveness and operational stability during transient conditions, confirming the technology's potential for flexible energy management and effective coupling with intermittent renewable sources.

Another system level analysis has been carried out, and a >10 kW reversible SOC (rSOC) was tested at constant load, and the enthalpy flow analysis and efficiency calculations confirmed stack efficiencies

above 95% and system efficiencies up to 92% under optimized thermal integration scenarios, highlighting the decisive role of steam generation and heat recovery strategies in determining overall performance. These results validate the scalability of SOC technology and highlight its potential for flexible energy management, seasonal storage, and integration into hybrid energy systems.

Overall, this work provides a comprehensive understanding of SOC behavior across multiple scales, from local electrochemical phenomena to integrated system operation. The findings contribute to advancing diagnostic methods, optimizing operating strategies and improving the efficiency and durability of SOC-based systems. Ultimately, the research supports the future deployment of solid oxide technologies within renewable energy infrastructures, contributing to global decarbonization and sustainable energy storage.

Author	Francesco Marino, Department of Engineering, University of Naples Parthenope, Centro Direzionale - Isola C4 (80133), Napoli, Italy Email: francesco.marino005@studenti.uniparthenope.it
Supervisors	Prof Elio Jannelli, Department of Engineering, University of Naples Parthenope Dr Francesca Santoni, Laboratory for Hydrogen and New Energy Vectors (H2V), Division of Technologies and Vectors for Decarbonization (DEC), Department of Energy Technologies and Renewable Sources (TERIN), ENEA Italian National Agency for Energy, New Technologies and Sustainable Economic Development Dr Ville Saarinen, VTT Technical Research Centre of Finland
Reviewers	Prof. Vincenzo Palma, Università di Salerno Prof. Francesco Todaro, Politecnico di Bari Prof. Ilaria Baffo, Università degli Studi della Tuscia Prof.ssa Laura Tribioli, Università Niccolò Cusano Prof. Andrea Frattolillo, Università degli Studi di Cagliari Prof. Laura Oca Perez, Mondragon Unibertsitatea Prof. Vanja Subotic

	TU Graz

PREFACE

This PhD thesis is entitled *“Multi-Scale Experimental and System-level Analysis of Solid Oxide Cells: Studies and Applications for Energy Storage Purposes”*, and has been carried out in the facilities of ENEA Casaccia Research Centre in Rome and in VTT – Technical Research Centre of Finland in Espoo. The research was conducted under the supervision of Professor Elio Jannelli and Dr. Francesca Santoni, and was developed within the framework of Italian national and European initiatives focused on hydrogen and advanced energy systems. The doctoral project ran from November 2022 to October 2025 and was hosted at the ENEA Casaccia Research Center, in the Laboratory for Hydrogen and New Energy Vectors (H2V), Division of Technologies and Vectors for Decarbonization (DEC). A collaboration with VTT has also been done from Nov 2024 to Jun 2025.

The first chapter of the thesis (*Introduction*) presents a comprehensive overview of the energy transition context, the role of hydrogen as a strategic energy carrier, the potential of fuel cells/electrolyzers – specifically Solid Oxide Cell (SOC) technology – and its operating principles. These sections introduce the research questions of the study.

The second chapter (*Materials and Methods*) is focused on the description of the experimental activities and setups used in this work, while the third chapter (*Results and Discussion*), which comprises the research carried out throughout the PhD, represents the core of the study.

The final chapter (*Conclusion*) presents the conclusions, the answers to the research questions proposed earlier and outlines future research directions.

CONTENTS

LIST OF FIGURES

LIST OF TABLES

Multi-Scale Experimental and System-level Analysis of Solid Oxide Cells: Studies and Applications for Energy Storage Purposes

1. Introduction

The issue of energy supply represents one of the most critical topics for the entire scientific community, encompassing multiple dimensions: technical, engineering, social, economic, and environmental. This chapter presents an examination of the challenges and open questions that researchers and scientists are called upon to address, while also assessing how hydrogen has gained momentum and is increasingly regarded as a promising solution within the framework of sustainable and efficient energy carriers.

Particular attention will be devoted to solid oxide technology – the specific focus of this work – notable for its operational reversibility and high efficiency. The discussion will highlight the key issues identified through the preliminary analysis, as well as the opportunities that this study aims to explore.

Finally, the motivations and research questions that have guided the development of this work will be presented in detail, as they constitute the starting point for the design of the methodology and for the interpretation of the results.

1.1 Transition From Fossil Fuel-Based To Low-Carbon Technologies

The steep growth in global demand for primary electricity represents both a major subject of debate and an area of increasing concern at the international level. The rapid rise in the world's population – which reached 8 billion in 2022 – together with the growing energy requirements of both industrialized nations and developing countries, has led in recent years to a significant increase in energy demand and, consequently, in energy production.

The results of recent studies on global energy production, broken down by source and updated to 2024, are reported in Figure 1a and Table I. It can be observed that non-renewable sources still account for the large majority, with the combined production of coal, oil, and natural gas making up 81.3% of the total. Renewable sources' contribution is 14% (including solar, hydro, wind, and geothermal), a share that increases to 18.7% when nuclear and biofuels are also considered [1]. Although the trend is growing, the contribution from clean energy sources remains insufficient to ensure a safe level of pollutant and CO_2 emissions. Atmospheric concentrations of CO_2 continue to rise year after year, from approximately 290 ppm of the pre-industrial era to 432 ppm in 2025 [2], as shown in Figure 1b. This phenomenon is a direct consequence of the combustion of carbon-containing fuels, through which the chemical energy stored in the fuel is converted into other forms of energy.

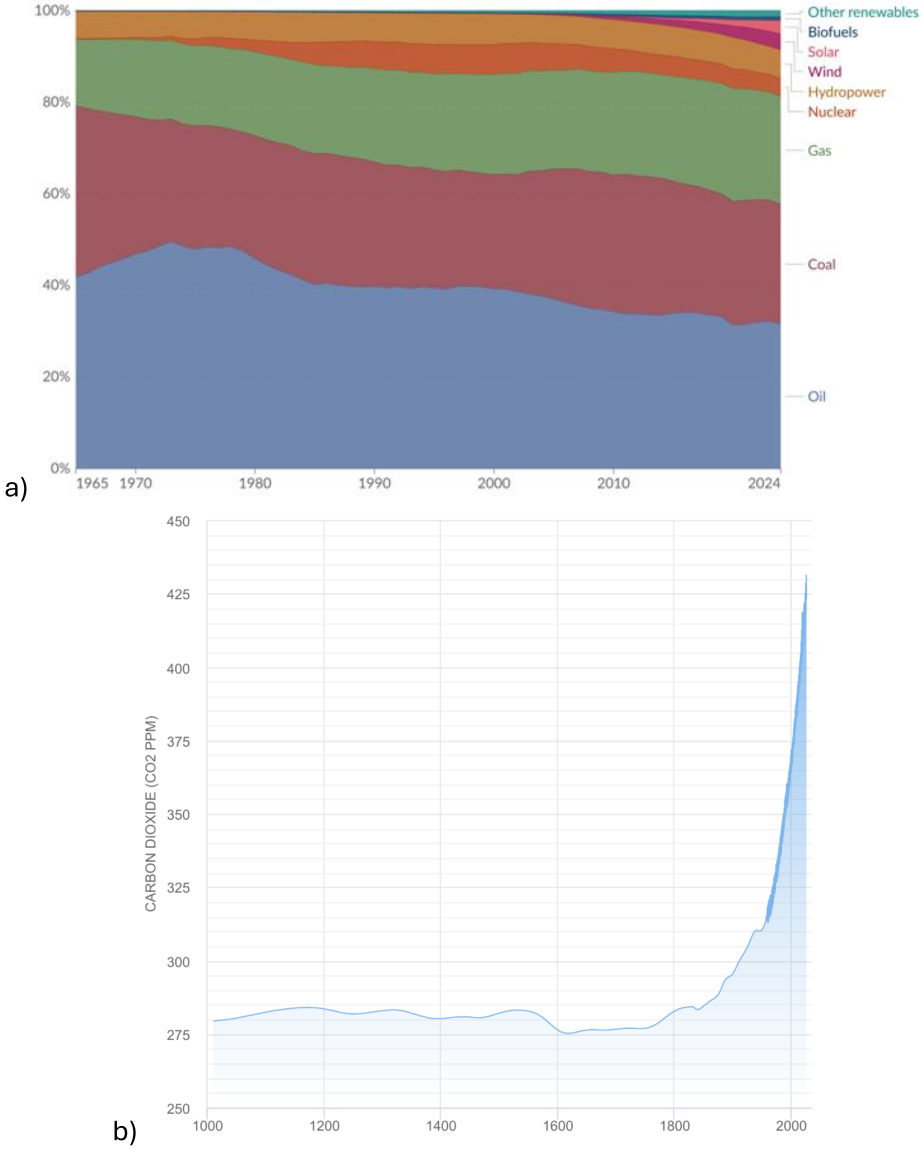

***Figure 1**: a) global energy production from 1965 to 2024, broken down by source and expressed in percentage of overall production* [1]*; b) concentration level of CO_2 in the atmosphere over the course of the years* [2].

***Table I**: global energy production in 2024, broken down by source [1]*

Source	**Production [TWh]**
Natural gas	41,278.3
Coal	45,850.5
Oil	55,292.1
Nuclear	6,871.8
Hydro	10,860.8
Wind	6,124.5
Solar	5,150.6
Biofuels	1,366.9
Other renewables	2,476.4

In the current context, characterized by increasing pressure on global energy demand and the need to meet stringent climate change mitigation targets, the transition from fossil fuels to low- or zero-carbon technologies emerges as a key process. The current energy paradigm can be described as a complex system, in which the progressive penetration of renewable sources introduces variability and non-dispatchability, thereby requiring complementary solutions to ensure security and stability of supply. [3], [4]. In this scenario, it becomes essential to maximize the potential of each energy source in the sectors where it can achieve the highest levels of efficiency and effectiveness.

Hydrogen is assuming a strategic role as a flexible and cross-sectoral energy carrier. Its intrinsic properties – storability, transportability, absence of greenhouse gas or pollutant emissions, and applicability across a wide range of contexts – make it particularly well suited to act as a bridge between sectors that are difficult to electrify (such as hard-to-abate sectors or heavy transport) and the increasing share of variable renewable sources. Although it cannot be regarded as the only solution to decarbonization, hydrogen represents a key element in the construction of an energy system capable of integrating multiple technologies while consistently addressing long-term sustainability goals.

1.2 Role Of Green Hydrogen In The Transition Towards Low Carbon Technologies

Hydrogen is a highly versatile element, currently employed across a wide range of sectors. One of the most common application areas is the chemical industry, where it serves as a key feedstock for the synthesis of ammonia, methanol, and various other products [5], [6]. Although the electrification of the transport, residential, and industrial sectors is expected to increase, in certain areas such as heavy-duty transport, aviation, and maritime shipping, given the current state of technology, batteries are unlikely to represent an effective solution due to their low volumetric energy density [7]. This gap left by batteries could be addressed by fuel cell systems, which are capable of converting hydrogen, methanol, or ammonia into electrical energy and thereby into propulsion [8].

Secondly, steel production – classified as a hard-to-abate sector – also presents significant potential for decarbonization through the use of hydrogen, particularly if coal is replaced as the reducing agent in iron reduction processes [9]. The steel industry is among the most energy- and carbon-intensive sectors, with recent studies reporting that it accounts for approximately 11% of global CO_2 emissions, thereby making its decarbonization pivotal to achieving global climate targets [10].

Ultimately, hydrogen demonstrates particular potential in the field of seasonal energy storage. One of the major challenges associated with high shares of renewable energy, particularly wind and solar, is the seasonal mismatch between renewable generation and end-user demand, as electricity output from these sources often peaks during specific periods while demand may be highest in other seasons. Hydrogen therefore emerges as a mitigating option for this phenomenon, acting as an energy carrier that can store surplus generation and subsequently compensate for the lack of renewable production during periods of deficit [11].

The production cost of hydrogen is one of the most significant barriers to its large-scale deployment as an energy carrier. The most recent data for Europe, as of September 2025, refer to 2023 and are provided by the European Hydrogen Observatory: the levelized production cost of hydrogen via Steam Methane Reforming (grey hydrogen) averages around 3.76 €/kg, rising to 4.41 €/kg when a carbon capture installation is included. The most environmentally advantageous solution is clearly green hydrogen, produced via water electrolysis directly connected to a renewable energy plant, with production costs ranging between 4.13 and 9.3 €/kg. [12]. Similar estimates are reported for the U.S. market, with production costs ranging between 4.5 and 7.5 $/kg [13]. For reference, as of September 2025, the price of natural gas is approximately 32 €/MWh, or 0.46 €/kg [14]. The main factors contributing to the high cost of green hydrogen, compared to a fuel with a similar role and usage such as natural gas, are the cost of renewable electricity, the cost of electrolyzers, and the relatively low overall efficiency of the entire process [13].

Research focused on developing systems for the production and utilization of green hydrogen that are both efficient and economically sustainable – capable of competing with conventional energy sources – is therefore of paramount importance. Fuel cells and electrolyzers currently represent the most effective technologies for this purpose. Given hydrogen's strategic importance, it is crucial to explore the technologies that enable its efficient production and conversion.

1.3 Fuel Cell / Electrolyzer Systems: Technology Overview

Fuel cells and electrolyzers represent key technologies for the efficient production and use of hydrogen as a sustainable energy carrier. Electrolyzers are electrochemical devices that generate hydrogen and oxygen through the electrolysis of water, powered by an electrical current. Fuel cells, on the other hand, convert the chemical energy stored in hydrogen directly into electricity, water, and heat. The main advantages of these devices include: (i) high conversion efficiency, due to the direct conversion of energy between electrical and chemical forms; (ii) zero emissions of polluting gases; (iii) very low noise levels. Depending on the specific type, additional benefits may be realized, such as fuel flexibility, reversibility, and cogeneration capability [15]. In all types, separate reactions take place at the two electrodes that form the cell (fuel electrode and air electrode), while ions are transported through the electrolyte from one electrode to the other, and electrons are directed through an external circuit. Fuel cells and electrolyzers are generally classified according to the material used for the electrolyte, as illustrated in Table II and Table III, where their main characteristics are also described [16], [17], [18], [19].

***Table II**: comparison of main fuel cell technologies [17], [18], [19]*

Fuel cell type	Polymer Electrolyte Membrane (PEM)	Alkaline (AFC)	Phosphoric Acid (PAFC)	Molten Carbonate (MCFC)	Solid Oxide (SOFC)
Electrolyte	Perfluorosulfonic acid	Aqueous solution of KOH, soaked in a matrix	Phosphoric acid soaked in matrix	Molten lithium, sodium, and/or potassium carbonates, soaked in a matrix	Yttria stabilized zirconia
Operating temperature [°C]	< 120	< 100	150 – 200	600 - 700	500 - 1000
Typical stack size [kW]	< 1 – 100	1 – 100	5 – 400	300 – 3000	1 – 2000
Efficiency [%]	60	60	40	50	60 (electric); > 80 (CHP)

***Table III**: comparison of main electrolyzers technologies [20], [21], [22], [23], [24], [25], [26], [27], [28]*

Electrolyzer type	Polymer Electrolyte Membrane (PEM)	Alkaline (AWE)	Anion Exchange Membrane (AEM)	Solid Oxide (SOEC)
Electrolyte	Nafion	Aqueous solution of KOH, soaked in a matrix	Polymer membrane	Yttria stabilized zirconia
Operating temperature [°C]	50 – 80	60 – 90	40 – 60	600 – 850
Efficiency [%]	65 – 80	60 – 70	55 – 70	> 80

Among the broad range of fuel cell types, solid oxide cells (SOCs) represent a particularly promising technology due to several intrinsic strengths, including: (i) higher conversion efficiencies compared to other fuel cell types in both operating modes (fuel cell and electrolysis), (ii) fuel flexibility at the inlet, and (iii) reversibility [29], [30].

1.4 SOC Operating Principles And Electrochemical Performance

In Figure 2, a schematic representation of the main mechanisms and phenomena occurring in a solid oxide cell (SOC) is provided. In SOFC mode, for the sake of simplicity, the schematic assumes pure H_2

as the fuel supplied to the anode (fuel electrode), while air is supplied to the cathode (air electrode). The fuel (H_2) diffuses through the porous structure of the anode and reaches the interface with the electrolyte. In this region, known as the triple phase boundary (TPB), hydrogen is oxidized by oxygen ions (O^{2-}) coming from the cathode, which have crossed the electrolyte, thereby forming H_2O and releasing two electrons (e^-). These electrons flow through an external electrical load connected between the anode and cathode, before reaching the cathode, where they reduce oxygen from the air. The newly formed O^{2-} ions then migrate across the thickness of the cathode until they reach the electrolyte interface. Since the electrolyte is an ionic conductor, it allows these ions to move towards the opposite interface, at the anode, where they participate in the oxidation of additional incoming fuel.

The description above can be conveniently summarized by the electrochemical half-reactions occurring at the two electrodes. In particular, Eq. 1 refers to the fuel electrode, Eq. 2 to the air electrode, and Eq. 3 represents the overall reaction [31], [32]:

$$H_2 + O^{2-} \rightleftharpoons H_2O + 2e^- \qquad (1)$$

$$\frac{1}{2}O_2 + 2e^- \rightleftharpoons O^{2-} \qquad (2)$$

$$H_2 + \frac{1}{2}O_2 \rightleftharpoons H_2O \qquad (3)$$

In SOEC mode, the operation is based on the splitting of steam into hydrogen and oxygen, which is the reverse of the SOFC process. At the fuel electrode (cathode), steam is reduced, generating hydrogen and oxygen ions (Eq. 4). The latter migrate through the electrolyte towards the air electrode (anode), where they are oxidized, releasing molecular oxygen (Eq. 5). The electrons produced at the air electrode are transferred back to the fuel electrode through an external circuit. The overall reaction is represented in Eq. 6 [33]. Here too, for the sake of simplicity, only steam is considered as the gas supplied to the fuel electrode.

$$H_2O + 2e^- \rightleftharpoons H_2 + O^{2-} \qquad (4)$$

$$O^{2-} \rightleftharpoons \frac{1}{2}O_2 + 2e^- \qquad (5)$$

$$H_2O \rightleftharpoons H_2 + \frac{1}{2}O_2 \qquad (6)$$

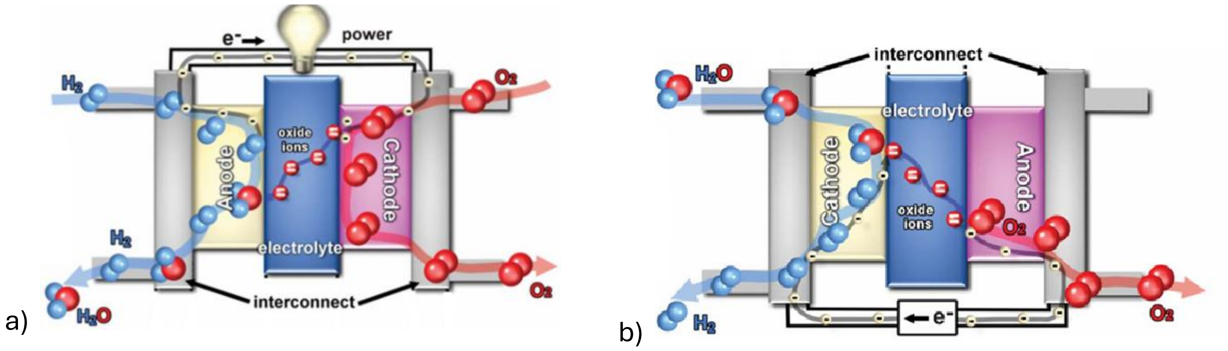

***Figure 2**: a) Schematic representation of a solid oxide cell operating mechanism in fuel cell mode [34]; b) Schematic representation of a solid oxide cell operating mechanism in electrolysis mode [34].*

The maximum electrical work obtainable from a fuel cell operating at constant temperature and pressure is given by the change in Gibbs free energy between reactants and products, as defined in Eq. 7 [32]:

$$W_{el} = \Delta G = G_{f,products} - G_{f,reactants} = -n \cdot F \cdot V \tag{7}$$

Where W_{el} [J] is the electrical work, ΔG [J/mol] is the Gibbs free energy variation, $G_{f,\ products}$ and $G_{f,\ reactants}$ [J/mol] are the free energy of the products and of the reactants respectively, n [-] is the number of electrons taking part in the reaction, F [C / g mol e$^-$] is the Faraday constant and V [V] is the cell voltage. From Eq. 7, it therefore follows that:

$$V = -\frac{\Delta G}{2F} \tag{8}$$

Let us consider the generic chemical reaction:

$$aA + bB \rightleftarrows cC + dD \tag{9}$$

Where *a, b, c, d* are the stoichiometric coefficients of the respective species *A, B, C, D*.

The Gibbs free energy can be expressed as a function of the activities and concentrations of the reactants and products. The following relation assumes ideal gas behavior, and is therefore slightly simplified compared to its more general form [32]:

$$\Delta G = \Delta G^0 + RT \ln\left(\frac{[C]^d[D]^d}{[A]^a[B]^b}\right) \tag{10}$$

Where ΔG^0 [J/mol] is the Gibbs free energy in standard conditions, *[A], [B], [C]* and *[D]* [-] are the concentrations of the species *A, B, C* and *D*, *R* [J/mol K] is the universal gas constant, *T* [K] is the operative temperature

The concentration of a species *i* can, in turn, be expressed as the ratio between the partial pressure of the species p_i [Pa] and the standard pressure p_0 [Pa] (100 000 Pa):

$$[i] = \frac{p_i}{p_0} \tag{11}$$

The ideal gas assumption is justified in the present study due to the high temperatures and low pressures involved [31].

From Eq. 8, Eq. 10, and Eq. 11, the Nernst equation (Eq. 12) can be derived, which allows the calculation of the maximum potential difference generated by a cell under open-circuit conditions and perfect reversibility. Below is the expression of the equation specialized for a fuel cell supplied solely with hydrogen (in power generation mode) or solely with water (in electrolysis mode):

$$V_{Nernst} = -\frac{\Delta G^0}{2F} - \frac{RT}{2F} \ln\left(\frac{[p_{H_2O}]}{[p_{O_2}]^{0.5} \cdot [p_{H_2}]}\right) \tag{12}$$

Eq. 12 can be rewritten in a more mathematically elegant form:

$$V_{Nernst} = E^0 + \frac{RT}{2F} \ln\left(\frac{[p_{O_2}]^{0.5} \cdot [p_{H_2}]}{[p_{H_2O}]}\right) \tag{13}$$

When the cell is operating and delivering current, various polarizations arising from irreversible processes cause the theoretical Nernst potential to decrease (in fuel cell mode) or increase (in electrolysis mode) to a voltage that depends on the operating point [31], as expressed in Eq. 14. It should be noted that the positive sign preceding the polarization terms corresponds to electrolysis mode, whereas the negative sign applies to fuel cell mode.

$$V_{cell} = V_{Nernst} \pm \left(\eta_{act,fuel} + \eta_{act,air}\right) \pm \eta_{ohm} \pm \left(\eta_{conc,fuel} + \eta_{conc,air}\right) \tag{14}$$

Activation polarization

Activation energy is required to overcome the energy barrier that prevents a reaction from occurring spontaneously. Accordingly, activation polarization is associated with the energy barrier that must be surpassed for the reaction to proceed. Several factors influence activation losses, including the type of reaction, the chemical properties of the catalyst, the activity of the reactants, and the structure of the electrodes. The relationship between the current density and the overpotential generated at an electrode is described by the Butler – Volmer equation [31], shown in Eq. 15:

$$j = j_0 \cdot \left[exp\left(\frac{\alpha \cdot F \cdot \eta_{act}}{R \cdot T}\right) - exp\left(\frac{(1-\alpha) \cdot F \cdot \eta_{act}}{R \cdot T}\right)\right] \tag{15}$$

Where j [A/m^2] is the current density, j_0 [A/m^2] is the exchange current density, and α [-] is the charge transfer coefficient at the electrode. The exchange current densities for both the anode and cathode can be expressed using an Arrhenius-type relationship:

$$j_{0,an} = j_{0,an}^{pre} \cdot \left(\frac{p_{H2}}{p_{H2,ref}}\right)^{\gamma_{H2}} \cdot \left(\frac{p_{H2O}}{p_{H2O,ref}}\right)^{\gamma_{H2O}} \cdot exp\left(-\frac{E_{act,an}}{R \cdot T}\right) \tag{16}$$

$$j_{0,cat} = j_{0,cat}^{pre} \cdot \left(\frac{p_{O2}}{p_{O2,ref}}\right)^{\gamma_{O2}} \cdot exp\left(-\frac{E_{act,cat}}{R \cdot T}\right) \tag{17}$$

Where $j_{0,an}^{pre}$ and $j_{0,cat}^{pre}$ [A/m^2] are respectively the anode and cathode exchange transfer current density pre-exponential factors, $E_{act,an}$ and $E_{act,cat}$ [J/mol] are the activation energies for anode and cathode, $p_{x,ref}$ [Pa] is the reference partial pressures – assumed to be equal to the ambient pressure – and γ [-] is the reaction order of species *x*.

Ohmic polarization

Ohmic polarization arises from the transport of charge through the ionic and electronic conductors within the cell. In a SOC, both the electrolyte and the electrode layers follow Ohm's law [31], [35]:

$$\eta_{ohm} = i \cdot R_{ohm} \tag{18}$$

Where *i* [A] is the current and R_{ohm} [Ω] contains the contributions of the ionic conduction, electronic conduction, and contact resistance:

$$R_{ohm} = R_{ion} + R_{el} + R_{cont} \tag{19}$$

However, in typical SOCs only ionic resistance of the electrolyte is considered, other resistances are assumed to be orders of magnitude lower, thus negligible.

Concentration polarization

Concentration losses are associated with the rate of reactant conversion at the fuel electrode and the rate of gas diffusion through the porosity of the electrode. When the diffusion rate of the gas is lower than its consumption rate, a local undersupply of fuel causes a drop in cell voltage in fuel cell mode, and an increase in cell voltage in electrolysis mode. The rate of mass transport through a porous electrode can be described by Fick's first law of diffusion [31], [32]:

$$j = \frac{n \cdot F \cdot D_x \cdot (C_x^B - C_x^S)}{l} \tag{20}$$

Where D_x [mol / m^2 s] is the diffusion coefficient of the species *x*, C_x^B and C_x^S [-] are the concentrations of the species *x* in the bulk of the electrode and at the surface respectively, and l [m] is the thickness of the diffusing layer.

The maximum current, or the limit current, that can theoretically be obtained is when $C_x^S = 0$:

$$j_L = \frac{n \cdot F \cdot D_x \cdot C_x^B}{l} \tag{21}$$

Combining Eq. 20 and Eq. 21, it results:

$$\frac{C_x^S}{C_x^B} = 1 - \frac{j}{j_L} \tag{22}$$

By applying the Nernst equation (Eq. 12), the concentration polarization can be determined:

$$\eta_{conc} = \frac{RT}{2F} \ln\left(\frac{C_x^S}{C_x^B}\right) = \frac{RT}{2F} \ln\left(1 - \frac{j}{j_L}\right) \tag{23}$$

Figure 3 shows two typical current–voltage curves for a cell operating in fuel cell and electrolysis modes, where all polarizations are evident.

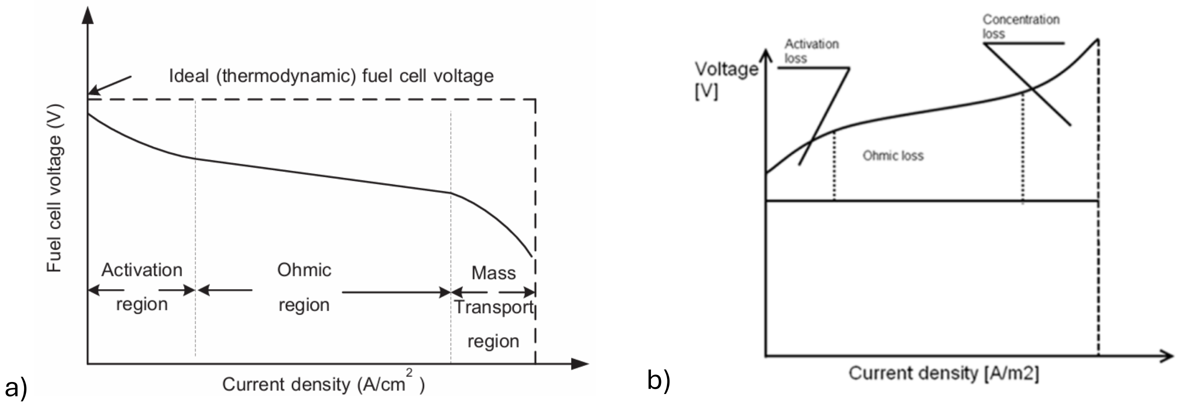

***Figure 3**: a) Typical shape of I-V curve in fuel cell mode [36]; b) typical shape of I-V curve in electrolysis mode [35].*

1.5 SOC materials and design

Following the analysis of SOC operating principles and electrochemical behavior, this section focuses on the materials and structural design that enable and influence their performance.

A single solid-oxide cell is composed of three elements: the electrolyte, the fuel electrode and air electrode, whose roles have been described in chapter 1.4 and whose working principles are shown in Figure 4. In a solid-oxide stack, individual cells are electrically connected in series or parallel by means of an interconnect, which completes the system by directing these electrons through the external circuit, thereby enabling useful electrical work [32].

In this chapter, more details on the materials employed and their characteristics are presented.

1.5.1 Fuel Electrode

The most widely used fuel electrode material in SOCs is the Ni-YSZ cermet, in which the YSZ ensures mechanical stability and porosity, while finely dispersed metallic nickel particles act as the catalytic sites for hydrogen oxidation (or steam reduction). Nickel alone tends to agglomerate at high temperatures, posing challenges to its application [37].

The most common configuration of a solid oxide cell (SOC) features an anode with a bilayer structure composed of: (i) a porous substrate with a thickness typically on the order of several hundred micrometers. This is the thickest and most mechanically robust portion of the fuel electrode and serves as the mechanical support for the entire cell. Its high porosity is designed to minimize mass transport losses; (ii) a functional layer, a thinner region with a typical thickness of 10–20 μm, deposited on top of the substrate and located near the electrolyte interface. This layer contains nickel particles that act as active sites for the oxidation and reduction of the gaseous species.

This anodic architecture is currently regarded as providing the best trade-off between low transport losses, structural stability, high electrochemical performance and cost-effectiveness [38].

Despite their extensive use, Ni-based electrodes suffer from several critical limitations, including particle agglomeration at elevated temperatures, carbon deposition, sulfur poisoning, and poor redox stability when operated with hydrocarbon- or sulfur-containing fuels [37], [39], [40].

To address these challenges, research efforts have focused on exploring alternative materials, such as cerium oxide (CeO_2), which has been investigated for its potential to mitigate carbon deposition and the poisoning of nickel by contaminants such as sulfur compounds and volatile organic compounds (VOCs). However, these approaches have so far achieved limited success, primarily due to stability issues that have emerged during operation [41], [42]. The use of a Cu-YSZ fuel electrode has been considered, given the superior resistance of copper to carbon accumulation and sulfur poisoning compared to nickel. However, copper suffers from low electrical conductivity, which limits its practical application in SOC systems [43].

Lin et al incorporated Cu-Ni composites into YSZ electrodes, reporting moderate catalytic activity for methane oxidation and significantly lower carbon cracking rates compared to pure Ni-based systems, thereby highlighting the effectiveness of Cu-Ni systems in enhancing hydrocarbon utilization while mitigating carbon deposition [44].

Perovskite oxides have emerged as promising fuel electrode materials owing to their excellent redox stability and intrinsic catalytic activity. However, their performance in hydrocarbon oxidation reactions remains limited, which poses a significant barrier to their widespread implementation in SOC systems [45], [46].

Finally, among the most extensively studied fuel electrode materials is ScSZ-Ni, which exhibits high electrical conductivity and good resistance to sulfur poisoning. However, the high cost of scandia-stabilized zirconia (ScSZ) remains a major drawback limiting its practical application [47].

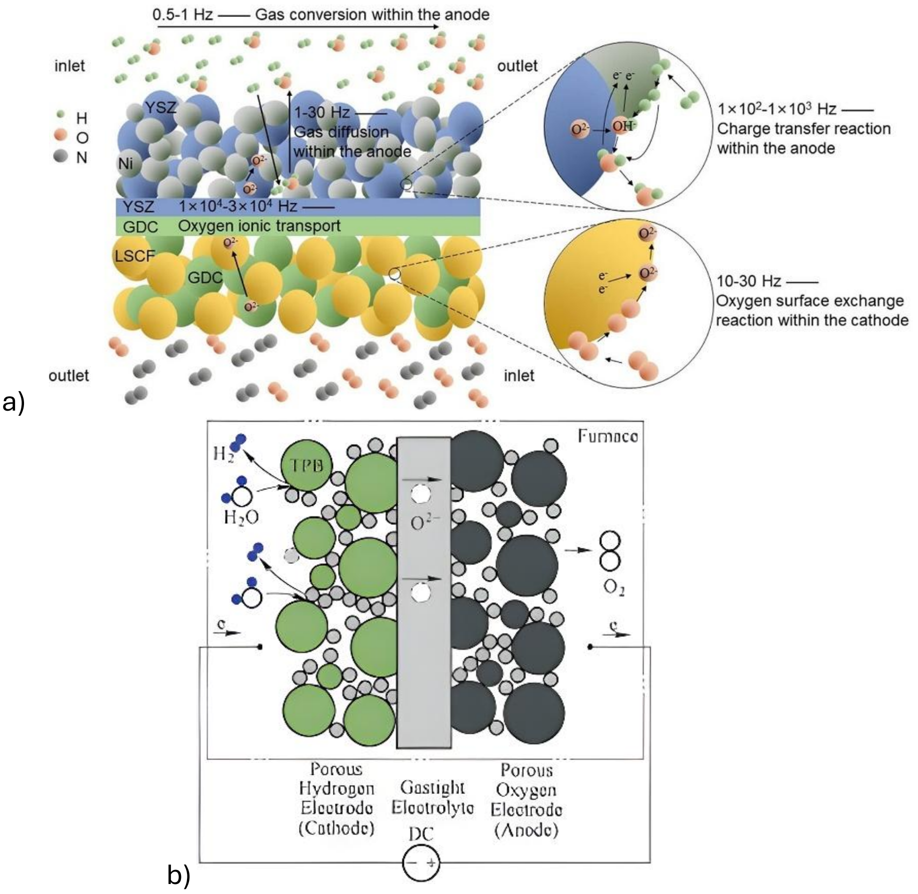

***Figure 4**: Diagram illustrating the paths of electrons and O^{2-} ions in the SOC structure; a) SOFC mode [48]; b) SOEC mode [49].*

1.5.2 Electrolyte

Key requirements for reversible solid oxide cell (rSOC) electrolytes include: (i) excellent sealing properties to prevent gas leakage and ensure system safety; (ii) high ionic conductivity, typically exceeding 0.01 $S \cdot cm^{-1}$ [50]; (iii) low electronic conductivity; (iv) high structural and chemical stability [51], [52]; (v) thermal expansion compatibility with other cell materials to avoid mechanical failure caused by mismatch-induced stresses.

The most widely used electrolyte is yttria-stabilized zirconia (YSZ), which is valued for its mechanical robustness and high oxygen-ion conductivity. However, pure ZrO_2 undergoes phase transitions around 1373 K, resulting in substantial volume changes that can compromise structural stability [53]. Doping with yttria or other stabilizers mitigates these issues by stabilizing the desired phases, increasing oxygen vacancy concentration, and enhancing ionic conductivity [54].

Beyond ZrO_2 - based systems, alternative electrolytes such as CeO_2 - and $LaGaO_3$ - based materials are being investigated for specific applications due to their favorable conductivity and stability characteristics [55]. Nevertheless, these materials may exhibit partial electronic conduction, often attributed to the reduction of Ce^{4+} to Ce^{3+} under low oxygen partial pressures [56].

1.5.3 Air Electrode

Oxygen electrodes in rSOCs are required to possess a porous structure to facilitate oxygen diffusion, high mixed ionic and electronic conductivity for efficient charge transport, chemical compatibility with adjacent cell components, and thermal expansion matching to minimize mechanical stress [37].
Most oxygen electrodes are based on perovskite oxides with the general formula ABO_3 . A-site doping with elements such as La, Sr, or Ba, and B-site incorporation of transition metals such as Mn, Co, or Fe, play a critical role in oxygen vacancy formation and redox behavior [57], [58]. $La_{0.8}Sr_{0.2}MnO_3$ (LSM) is widely employed due to its excellent thermal stability and compatibility with YSZ electrolytes [59]. To further improve performance, composite designs such as LSM-CuO-SDC and PdO/ZrO_2 -LSM-YSZ have been developed to expand the electrochemically active reaction zone and reduce polarization resistance [59] [60].
Cobalt-based perovskites, such as $La_{0.6}Sr_{0.4}CoO_3$ (LSC), offer substantially higher electrical conductivity - up to three to ten times that of LSM - and broader reaction zones, enhancing performance in both SOFC and SOEC operation [61], [62]. However, interface degradation can occur over time [63]. Strategies such as surface coatings with $Gd_{0.1}Ce_{0.9}O_2$ [64] and infiltration with CGO [65] have been demonstrated to improve long-term stability and electrochemical performance.

1.5.4 Interconnects

In rSOC stack assemblies, interconnects perform a dual function: they provide electronic conduction between adjacent cells while simultaneously acting as gas-tight barriers that separate the fuel and oxidant compartments. A schematic representation of a SOC cell including interconnects is given in Figure 5. The performance of interconnects has a direct impact on the electrical efficiency, mechanical integrity, and long-term durability of the entire system. Therefore, the careful selection and engineering of interconnect materials are crucial for the successful deployment of rSOC technology, particularly under dual-mode operation where the cell alternates between fuel cell and electrolysis modes.
To operate reliably under rSOC conditions, interconnects must satisfy several key requirements, including: (i) High electrical conductivity, typically above 10^4 $S \cdot m^{-1}$ at operating temperatures (700 - 850 °C) [66]; (ii) Gas tightness to prevent cross-leakage of H_2 and O_2, maintaining strict separation between the anode and cathode gas streams [31]; (iii) Chemical and thermal stability and compatibility with the electrodes and gases [67]; (iv) Mechanical robustness, (v) resistance to corrosion [68].

The most commonly used interconnect materials in rSOCs are ferritic stainless steels, including Crofer 22 APU, SS430, and SS441. These alloys provide good mechanical strength and acceptable electrical conductivity. However, their high chromium content can lead to Cr volatilization, which may migrate to the cathode and poison oxygen electrode catalysts, such as LSCF, resulting in performance degradation. To address this issue, protective coatings based on spinel-type oxides have been developed to inhibit chromium migration. Alternatively, ceramic interconnects, typically composed of perovskite-based materials, offer excellent chemical stability, though they are limited by lower electrical conductivity and higher fabrication costs [69].

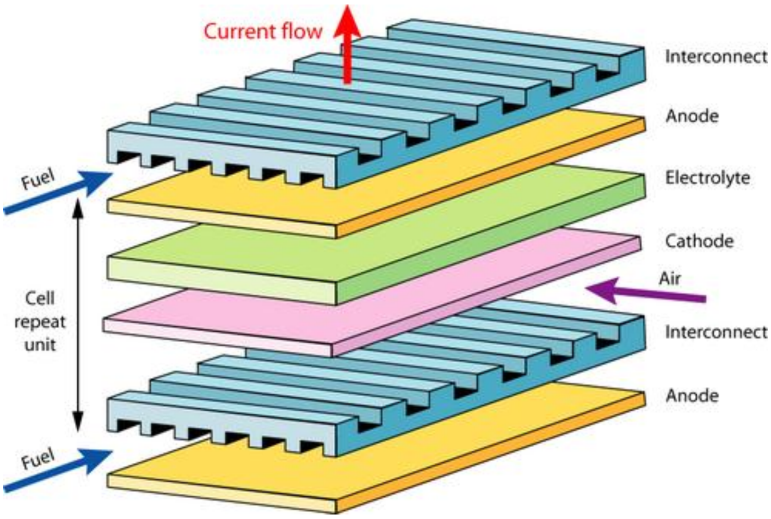

***Figure 5**: Basic SOC cell structure with interconnects [70].*

1.6 SOC Cells Degradation Mechanisms

An important requirement for commercial solid oxide cells is their stability and ability to preserve their performance over time. Degradation mechanisms in SOCs are numerous and they can be found in all of their components. The durability of SOC stacks must meet stringent lifetime requirements, especially for stationary applications, where this value is typically about 90,000 hours [71].

The cell performance degradation is usually observed as a gradual voltage decay in fuel cell operation and as a voltage increase in electrolysis. The degradation rate, generally expressed in mV/1000 h, is the consequence of chemical, thermal, and mechanical phenomena. Understanding these mechanisms at both the materials and system levels is therefore essential to enhance cell durability and ensure the long-term reliability of SOC systems.

The Ni-YSZ present in the fuel-electrode plays a central role in cell degradation since, although it ensures excellent electronic conductivity and catalytic activity, its microstructure is thermodynamically more unstable under high-temperature operating conditions. Prolonged exposure to steam, for example, leads to microstructural coarsening, phase changes, and chemical interactions that progressively increase polarization and ohmic resistance. The main degradation mechanisms at the fuel-electrode can be grouped into three categories: (i) material transport mechanisms, (ii) deactivation and poisoning effects and (iii) thermomechanical degradation.

Material transport mechanisms mainly involve nickel migration and coarsening. Over time, Ni particles tend to agglomerate to minimize surface free energy. This change, accelerated by high temperature and high steam partial pressure, causes a reduction in the length of the triple-phase boundary and, consequently, in the number of electrochemically active sites. The loss of active area increases the polarization resistance and lowers the overall cell performance. The phenomenon where larger Ni particles grow at the expense of smaller ones is particularly critical under electrolysis conditions [72], [73], [74], [75].

Nickel depletion and migration are additional degradation mechanisms often observed under SOEC operation. The high steam and oxygen partial pressures promote the volatilization of nickel as hydroxide species ($Ni(OH)_x$). This results in local Ni depletion and the formation of resistive zones that hinder charge transfer. Conversely, in SOFC operation, nickel migration toward the electrolyte may occur due to electrochemical gradients, occasionally causing local Ni accumulation and delamination. Both phenomena are strongly influenced by the ratio of H_2O to H_2 in the feed gas and by temperature [72], [73].

Redox cycling, caused by repeated oxidation and reduction of the Ni-YSZ electrode, is another major source of degradation. The process induces mechanical stress and possible fracture or delamination of the porous structure. Frequent cycling or high humidity during shutdown accelerates this degradation pathway and can lead to irreversible structural damage [71].

Other chemical effects, such as carbon deposition and sulfur poisoning, further compromise fuel-electrode performance. When carbon-containing gases are used, carbon may deposit blocking pores and catalytic sites. In addition, even impurities such as sulfur can adsorb on the Ni surface deactivating active sites and causing substantial increases in polarization resistance [76].

The air-electrode also experiences degradation due to several mechanisms, the most relevant being the chromium poisoning, which originates from volatile species deposits on the air-electrode surface. These compounds block oxygen reaction sites and are among the most detrimental phenomena affecting air-electrode durability [73].

The degradation of the electrolyte and interconnects also contributes to the overall performance loss. Yttria-stabilized zirconia (YSZ) may suffer from grain growth, yttrium segregation, and oxygen vacancy redistribution under long-term operation. These changes increase the ionic resistance and may induce microcracking during thermal cycling. Metallic interconnects undergo oxidation and chromium evaporation, which elevate contact resistance and lead to the formation of volatile Cr species. Protective coatings have been developed to limit chromium diffusion [71], [73], [77].

Thermomechanical stresses further accelerate cell degradation by causing cracks, delamination and mechanical instability. These stresses arise from mismatched thermal expansion coefficients between different layers, nonuniform temperature distributions, and transient operational loads. The severity of this effect grows with higher current densities [73].

Overall, the degradation behavior of SOCs results from a complex mixture of microstructural changes, chemical instability and thermomechanical stress. Electrochemical impedance spectroscopy and focused-ion-beam SEM are among the characterization methods that can directly correlate microstructural changes with performance degradation [71], [77].

1.7 Solid Oxide Cells Scale-Up From Single-Cell To Stack-Level

Scaling up solid oxide cells (SOCs) from single-cell units to multi-cell stacks represents a critical step in realizing the potential of this technology for industrial applications. This process, however, introduces a number of complexities and challenges that must be addressed to ensure reliable, efficient, and long-lasting operation.

Industrial prototypes with capacities of several kilowatts have already been demonstrated. For instance, the rSOC plant in Salzgitter, Germany, has a capacity of 40 Nm^3 H_2/h and consists of six modules, each comprising 48 stacks with 30 cells per stack. In SOEC mode, the AC power input is 143 kW, while in SOFC mode the AC power output is 30 kW [78], [79]. Similarly, demonstration, verification, and validation of a SOEC system integrated with a nuclear reactor have been carried out through a joint effort by FuelCell Inc. (responsible for engineering design) and Idaho National Laboratory (system testing). This project demonstrated a scalable 250 kW high-temperature SOEC capable of producing hydrogen using electricity and steam from the nuclear power plant, aiming to maximize efficiency. The primary goal was to generate physical test data that would inform the business case for hydrogen production and support mid-term commercialization efforts [80].
Further scaling to multi-megawatt capacities is underway. A high-temperature SOEC system operating at TRL8 is being demonstrated at a biorefinery in the Netherlands, with a nominal capacity of 670 Nm^3/h (over 60 kg/h of H_2), covering approximately 1% of the site's current hydrogen demand [81]. This project targets a stack electrical efficiency of up to 85% (LHV), a hydrogen production loss rate below 1.2% per 1000 h, and an energy consumption of approximately 39 kWh/kg H_2. Although the estimated hydrogen cost is about 2,550 $ per kg H_2/day, the design allows flexibility for further upscaling to 100 MW, potentially reducing the cost to about 2 $/kg in large centralized units or about 7.5 $/kg in smaller decentralized installations.

One of the key challenges distinguishing large-scale operation from single-cell testing is temperature control. At the single-cell level, the operating temperature is relatively uniform, whereas larger systems are prone to asymmetries. Non-uniform temperature distributions can lead to thermal stresses, which increase the risk of delamination and cracking, and can also cause uneven current density, resulting in localized accelerated degradation. For example, modeling studies by Zhang et al [82] on a 20-cell fuel cell stack revealed temperature gradients of up to approximately 100 °C, varying according to the gas flow configuration (see Figure 6). A common observation is that the temperature is highest in the central region of the stack and decreases progressively toward the periphery. Among various stack designs, counter-flow configurations have been shown to outperform others in terms of temperature uniformity in SOEC mode [83]. Effective thermal management, therefore, is essential for preserving stack performance and longevity.

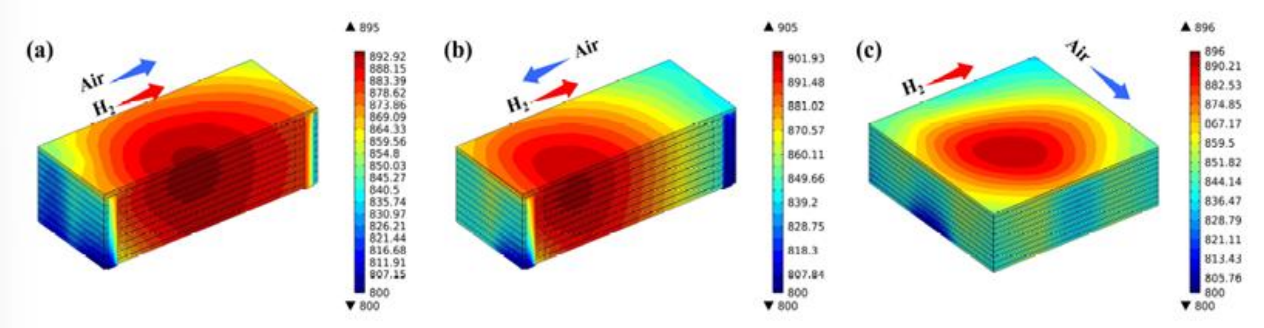

***Figure 6**: Temperature distribution prediction for (a) co-, (b) counter-, and (c) cross-flow 20-cell SOFC stack [82].*

Gas distribution across the stack is another critical issue. If the gas flow is not uniform between cells or within individual cells, concentration gradients can develop, leading to local efficiency losses and even gas starvation in some areas. While such issues may also occur at the single-cell level, they become increasingly pronounced as the system scales up. Moreover, non-uniform gas distribution directly affects temperature distribution, further complicating thermal management. To address this, optimized flow channel designs have been developed. Stack configurations are generally categorized into two types: (i) U-type, where all manifolds are located at one end of the stack, and (ii) Z-type, where inlet and outlet manifolds are placed at opposite ends. A graphical representation is shown in Figure 7.

Overall, Z-type configurations have demonstrated superior performance due to improved uniformity in temperature, electrochemical variables, and species concentration. For example, Choi et al [84] showed that in SOFC operation, Z-type stacks achieved better control of both the maximum temperature (705 °C versus 740 °C in U-type) and the maximum current density (0.43 A/cm^2 versus 0.6 A/cm^2), as illustrated in Figures 8 and 9. These results highlight the importance of manifold design for achieving stable and efficient stack operation.

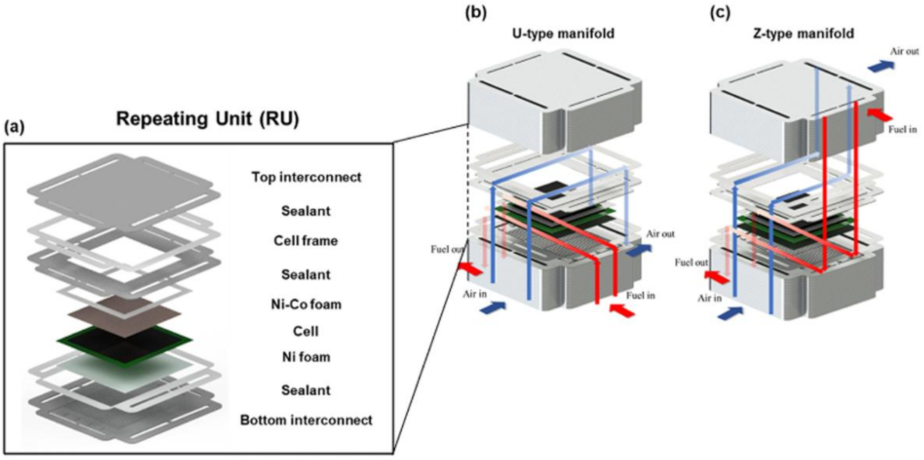

***Figure 7**: Schematic of: (a) single cell repeating unit, (b) U-type manifold stack, (c) Z-type manifold stack [84].*

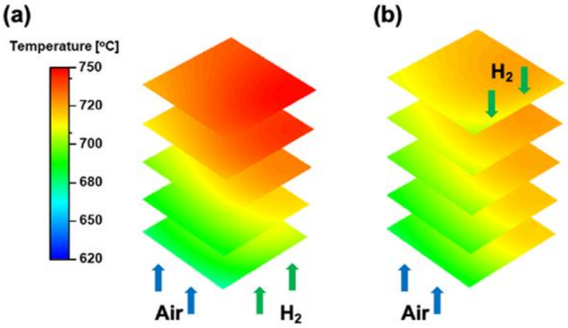

***Figure 8**: Temperature distribution under SOFC operation of: (a) U-type manifold stack, (b) Z-type manifold stack [84].*

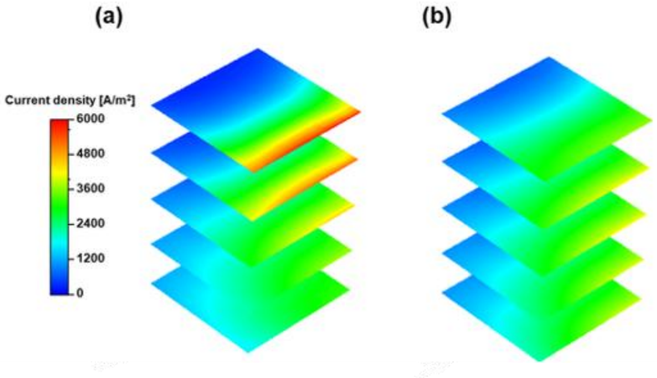

***Figure 9**: Current density distribution under SOFC operation of: (a) U-type manifold stack, (b) Z-type manifold stack [84].*

At stack level, interconnects also present significant challenges. Operating temperatures between 700 °C and 850 °C can cause oxidation and volatilization of chromium-containing steels, leading to cathode poisoning and long-term performance degradation. Protective coatings based on perovskite-type oxides have been widely adopted to improve chemical stability in both SOFC and SOEC operation [85]. Importantly, these coating processes must be compatible with large-scale manufacturing, adding additional constraints for industrial production. Recent research has also focused on improving stack manufacturability and cost-effectiveness. For instance, Pirou et al [86] proposed a monolithic SOC architecture produced via co-sintering, integrating all functional layers into a single ceramic block to achieve high power density and simplified assembly.

In conclusion, while stack-level operation introduces additional complexities – such as temperature gradients, non-uniform gas distribution, and interconnect limitations – the fundamental electrochemical phenomena can still be meaningfully investigated at the single-cell level. Many degradation mechanisms observed in single cells, including nickel migration, chromium poisoning, and interfacial instability, are consistently observed across scales [87], [88], [89]. Alenazey et al [90] further highlighted high operating temperature as a primary driver of performance decay, a factor equally relevant in both single-cell and stack environments. Therefore, single-cell studies continue to provide valuable insights into the behaviour of large-scale systems, while scale-up efforts must carefully address the additional engineering challenges that arise in multi-cell stacks.

1.8 Work motivation and Research questions

Solid Oxide Cell (SOC) technology is among the most promising candidates for high-efficiency energy conversion and long-duration storage, particularly in the context of renewable energy integration and decarbonization of hard-to-abate sectors. However, despite significant progress in materials development and stack design, several critical challenges remain unresolved when SOCs are operated under realistic conditions.

In particular, the performance and durability of SOCs are often compromised by localized degradation phenomena, such as thermal stress, uneven current distribution, and material aging. These effects are exacerbated under dynamic operating regimes, especially in electrolysis mode, where high steam concentrations and current densities can lead to strong gradients in temperature and gas composition. Moreover, the lack of harmonized metrics for evaluating system efficiency across different fuel blends, and the limited understanding of how SOCs behave when integrated with renewable energy systems and at real-scale level, hinder their scalability and practical deployment.

This research was motivated by the need to address these gaps through a multi-scale experimental and analytical approach. The work combines localized diagnostics, fuel composition studies, and system-level modeling to investigate SOC behavior under diverse operating scenarios. Custom-built test benches, in-operando measurement techniques, and real-world integration models were developed to generate high-resolution data and actionable insights.

This thesis addresses four distinct but complementary research gaps through the development and validation of novel experimental setups, modeling approaches, and system-level analyses.

The research questions addressed by the present doctoral thesis are reported below. They constitute the guiding framework around which the entire research activity has been developed, and are aimed at identifying clear answers and providing a meaningful scientific contribution to the issues concerning solid oxide cells raised in the preceding sections.

RQ1: *How can localized experimental characterization of SOCs be improved beyond conventional techniques to optimize electrochemical performance?*

While many studies have focused on SOEC performance and durability at stack-level [88], [91], [92], [93], [94], [95], single cell-level investigations remain essential to understand localized phenomena and degradation mechanisms.

Several works have explored long-term operation and accelerated stress testing, highlighting the influence of operating conditions on performance and stability: Tietz et al [96] successfully completed a test campaign on an electrode-supported solid oxide cell operated for 9000 h in SOEC mode with 80% humidification and with a current density of -1 A/cm^2, and a cell voltage degradation rate of 3.8%/kh was observed. Königshofer et al [97] instead opted for the development of accelerated stress test protocols in SOEC mode, with a water concentration and current density varying from 15% to 90% and from 0.250 A/cm^2 to 0.900 A/cm^2 respectively. The cell was kept in operation for about 200-300 h in continuously variable conditions, each presenting different kinds and degrees of impact on performance and microstructure of the cell. Nguyen et al [98] performed long term ageing tests of a two-cell planar electrode supported stack in steam electrolysis (3450 h), co-electrolysis (640 h) and fuel cell operation (4000 h). Nearly no degradation after 2000 h of steam electrolysis (800 °C, H_2/H_2O = 1/1, FU = 15%) at current density of -0.3 A/cm^2 was observed.

Cell degradation is a phenomenon influenced by multiple factors, some of which can be attributed to the cell fabrication process [73], [99] or to pinch-up, a factor excluded in this work due to the absence of geometric obstacles or cross-sectional restrictions in the gas channels. Despite the encouraging progress demonstrated in literature, cell degradation, proved to be adversely influenced by gas concentration and temperature gradients [100], is still considered one of the major concerns in SOEC technology [73], [95], [101]: as Wolf et al [102] proved, their 1000 h-test at -1A/cm^2 and 800 °C showed a 370 mV/kh voltage increase, as well as the delamination of the LSC electrode and a partial Ni depletion in the active layer. To address these issues, Tong et al [103] developed and tested a nanoengineered SOC featuring a gadolinium-doped ceria (CGO) nanogranular coating on the fuel electrode and a CGO scaffold on the air electrode, in order to improve both performance and degradation behavior. They achieved high performance and durability (voltage decrease of only 0.024 V/kh after 900 h at 1 A/cm^2), demonstrating that the CGO coating suppresses Ni migration while preserving the structure of active sites. Regarding cell degradation, the long-term 23 kh test by Schefold et al [104] highlights a key factor, namely the partially different response of electrolyte-supported cells under prolonged stress: impedance spectroscopy reveals a predominantly ohmic degradation, attributable to the loss of ionic conductivity in the electrolyte, while the fuel electrode shows no significant signs of deactivation.

One of the approaches that allows to improve the performance and minimize the degradation is the optimization of the thermal and gas composition gradients distribution. On one hand, computational models are an effective method to predict the behavior of every portion of the cell as a function of its operating conditions. 1D and 2D models are mainly used to describe the I-V characteristic of a SOEC, whereas 3D models can provide detailed concentration of gas species and temperature distribution [105]. A few 3D model-related articles are retrievable in literature, developed to study impacts of operating conditions on SOECs, such as nominal working temperature, inlet gases compositions and gas flow field patterns [106], [107], [108], [109], [110].
On the other hand, experimental studies on localized cell behavior and performance allow the validation of the numerical models and confirm the presence of the phenomena predicted by the models.

The analysis of segmented SOCs has been reported in several studies, including that of Schiller et al [111], who employed a planar, fuel-electrode-supported SOFC divided into 16 galvanically isolated segments for local experimental measurements, complemented by a 2D electrochemical model for comparison. This study revealed pronounced gradients of gas concentration and current density along the fuel electrode side of the cell, whereas the air electrode side exhibited much smaller gradients. Additional investigations on fuel cell operation have been conducted, including those by Wu et al [112], Kim et al [113], and Lang et al [114].
With regard to SOEC operation, Moussaoui et al [115] employed a segmented experimental setup to analyze the local electrochemical and thermal behavior of a commercial solid oxide cell. Their configuration partitioned the oxygen electrode into 20 segments, each individually controlled by an electronic load under both galvanostatic and potentiostatic modes, enabling the measurement of voltage and current density for each segment. Königshofer et al [116] tested cells with a segmented air electrode under steam electrolysis and co-electrolysis conditions, with the aim of experimentally investigating local impedance and degradation characteristics.

Through this PhD work, the localized temperature and gas concentration distribution within an SOEC using a custom experimental setup comprised of 11 sampling points is assessed. By analyzing these data and applying thermodynamic principles, valuable insights into the electrochemical performance of the cell are obtained. The objective of the study is not to develop complex fluid dynamic models for the precise determination of all possible variables but rather to derive results that provide a qualitative understanding of the underlying phenomena at play and their directional trends. Thus, the aim is to demonstrate that, with a simple yet innovative experimental setup, it is possible to extract extensive information regarding the cell's operation across its entire surface, thereby providing insights into the effects of these phenomena on degradation and durability.

In this context, previous studies have already demonstrated the effectiveness of a similar multisampling setup in fuel cell mode, focusing on the fuel-electrode surface under various operating conditions. In particular, Santoni et al [117] and Pumiglia et al [118] employed this configuration to investigate the local gas-phase composition and temperature distribution in SOFCs fed by reformate natural gas. Conti et al [119] also used this setup for combined experimental-modeling studies. These works laid the foundation for the present study, which extends the application of the multisampling approach to SOEC operation, enabling a detailed spatial analysis of electrochemical and thermal behavior under electrolysis conditions. The main differences with respect to previous studies conducted on a similar setup lie firstly in the operation of the test bench under electrolysis mode (thus involving much higher water content, particularly at the inlet), which requires more accurate thermal management of the gas mixture in the sections upstream of the cell. Secondly, the extension includes cell fictitious segmentation as well as the development of simplified electrochemical and thermal predictive models, aimed at determining the local distribution of current density, voltage, and temperature.

In conclusion, this research question is addressed through the development of a custom-built multisampling test bench enabling simultaneous in-operando measurements of temperature and gas composition across eleven points on the fuel electrode surface. This setup allows for the detection of spatial gradients that are not observable through conventional inlet-outlet analysis, and supports the development of a simplified electrochemical-thermal model for predicting local current density and voltage distributions.

RQ2: *How does fuel composition affect the performance and efficiency of SOC stacks in stationary CHP configurations, and which metrics are most appropriate for comparative evaluation? Is SOC technology suitable for current and future gas grid scenarios?*

Discussions on an efficient use of hydrogen must be preceded by an intelligent and sustainable production of this energy vector. Fuel cells are modular and scalable systems, enabling small-scale decentralized power generation and allowing a more effective exploitation of widespread gas and power networks, while producing energy closer to the end users. This represents a distinctive advantage compared to traditional thermo-electric systems, which are mainly conceived for centralized and large-scale power generation.

One of the most promising characteristics of Solid Oxide Fuel Cells (SOFCs) is their capability to process a wide range of fuels with high electrical efficiencies, when compared to other types of fuel cells [120], [121], [122]. In modern commercially available SOFC μ-CHP systems, natural gas is the primary fuel utilized. However, in order to promote an increased production and use of clean energy while simultaneously exploiting the existing natural gas distribution infrastructure, it is essential to enable the utilization of blends of natural gas with gases obtained from renewable sources, such as green hydrogen and biogas.

For the successful development of hydrogen-related technologies, a safe and reliable infrastructure is required. The cheapest and quickest solution would consist in using, and where necessary retrofitting, the existing gas grid to transport hydrogen even across different countries [123]. Given the different physical and chemical characteristics of hydrogen compared to natural gas, this condition is not automatically guaranteed with the current gas grid. The high permeability of the hydrogen molecule makes it prone to diffuse into the metallic lattice [124], causing embrittlement and pipeline corrosion [125]. Embrittlement refers to the permeation of hydrogen molecules through the steel structure, whose consequences include a loss of material ductility and strength as well as material failure; the fracture toughness of the metal can be reduced to one tenth of its original value [126]. Corrosion is an electrochemical material deterioration phenomenon [127], which is exacerbated by the presence of impurities such as sulphur, chloride and CO_2 in the gas mixture [125].

This issue can be tackled by employing protective coatings (organic, inorganic or metallic layers [128]) that act as barriers to prevent excessive exposure of metallic materials to hydrogen and impurities [125]. The compatibility of the current gas grid pipelines with H_2–NG mixtures therefore represents a major concern, and numerous studies and research projects conducted in recent years have investigated different case studies [125]. It has been shown that, when operating at low gas pressure, hydrogen leakage is comparable to natural gas leakage, whereas at higher operating pressures hydrogen leaks more easily [123]. Moreover, improper injection and mixing of hydrogen with natural gas may lead to separation of the two gas streams, resulting in increased leakage rates and enhanced pipeline material degradation [125].

ENTSOG has shown that, in the case of very low hydrogen content in the gas mixture (blending percentages up to 2 vol.% in natural gas), no specific adaptations of the infrastructure nor additional measures are required, regardless of the operating pressure; for higher hydrogen concentrations this condition may no longer be valid [123], [129]. In [123], the most common pipeline materials were tested while transporting a 20 vol.% H_2 blend in natural gas at 80 bar: the experimental campaign lasted 3000 h and no significant embrittlement effects were observed. At present, a unanimous conclusion on this issue has not yet been reached; therefore, further research is required to more accurately assess the effects of hydrogen introduction into the gas grid and to identify viable solutions for the modification of the current infrastructure.

Considering the prospective transition of the natural gas grid toward hydrogen in order to decarbonize the gas sector [130], SOFCs could play a crucial role as flexible, efficient and clean stationary Combined Heat and Power (CHP) systems. In particular, SOFC CHP systems could operate interchangeably with different feedstocks supplied by the gas network, such as natural gas, hydrogen and various blends of these two gases.

The fuel-flexibility characteristics of SOFCs arise from two main reasons: i) the high operating temperatures (650–850 °C) favour the thermochemical decomposition reactions of carbonaceous fuels, such as methane reforming and the water–gas shift reaction [131]; and ii) the presence of metallic Ni as electro-catalyst material in the fuel electrode, which also acts as a thermochemical catalyst for the aforementioned decomposition reactions [132]. In this way, carbonaceous feedstocks are decomposed in different configurations (external and internal reforming), converting natural gas and CO and enriching the fuel stream in hydrogen, which subsequently reacts electrochemically at the active layer of the fuel electrode [32].

SOFC systems are not solely composed of the fuel cell stack module, but rather consist of complex assemblies encompassing several components that cooperate to increase the overall performance and efficiency of the integrated system through the recycling of unused streams, the re-utilization of internal energy flows and the enhancement of the Fuel Utilization factor (FU) [31]. In particular, the most common system-level architecture includes an external fuel pre-processor reactor (external reformer), which partially converts the fresh fuel feedstock at high temperature in the presence of steam sourced from the recycled fuel off-gas exiting the stack module [133]. The partially pre-reformed inlet stream continues its chemical conversion within the stack module itself (internal reforming in the electrode bulk substrate) before the actual electrochemical reaction takes place. Since the single-pass FU cannot be excessively high in order to avoid localized fuel starvation, possible Ni re-oxidation and operation in concentration overpotential regimes – all of which lead to premature degradation of the cell and stack performance [134], [135] – a substantial amount of unused fuel mixed with product gases exits the stack as off-gas and can be recirculated back into the system, for instance toward the external pre-reformer by means of high-temperature blowers or ejectors, according to the selected system concept. This strategy allows maximization of the global FU as well as of performance and efficiency, with a significant impact on system design, component sizing and operating costs [134].
The design of the balance-of-plant components and the operating strategy (e.g. recirculation rate, degree of external and internal reforming) is therefore of paramount importance to enhance the performance of the integrated system. Nevertheless, the core component of the SOFC integrated system remains the SOFC stack itself, and the determination of stack-level performance is crucial to assess the overall system-level behaviour. Experimental data are essential to obtain detailed information that can be used to calibrate and improve system-level models and to optimize the outputs of the integrated SOFC system.

One of the goals of the present work is therefore to evaluate the performance and the potential of the current SOFC technology in three different gas-grid scenarios: present conditions (100% natural gas), mid-term transition scenarios (hydrogen blended with natural gas) and long-term perspectives (100% hydrogen). Given the absence of standardized efficiency definitions in the fuel cell field, several approaches to define and quantify this crucial parameter have been proposed, both at stack and system level. Within this framework, part of this doctoral research is specifically devoted to the harmonization and critical assessment of efficiency definitions, in order to enable consistent comparisons across operating conditions and technological scenarios and to facilitate a meaningful comparison between SOFC systems and more traditional power generation technologies.

The present research question is therefore explored via an experimental campaign on a fuel-electrode-supported SOC short stack operating with different fuel blends, simulating progressive gas grid decarbonization scenarios. The study compares stack-level performance and efficiency across these feedstocks, and proposes harmonized definitions of efficiency to support cross-scenario analysis.

RQ3: *What is the potential of rSOC systems for integration with renewable energy sources and for energy storage applications in residential and industrial scenarios?*

In their 2021 report, the International Energy Agency (IEA) stated that in order to be on the pathway to world net-zero emissions by 2050, by 2035 emissions need to decrease by 80% in advanced economies and by 60% in emerging markets and developing economies, compared to the respective 2022 levels, hence highlighting the urgency to promote the penetration of clean energy sources [136]. Achieving these targets represents one of the main objectives of world leaders, policy makers and academia [137]. The ever-increasing share of electrical energy supply from renewables is, on the one hand, pushing towards the carbon neutrality targets set out by the IEA, but on the other hand the fluctuating, intermittent and non-programmable nature of these sources (photovoltaic and wind above all) makes the availability of efficient and flexible energy conversion and storage systems an absolute priority [138]. Balancing the constant mismatch between supply and demand while maintaining power grid stability and ensuring the optimal exploitation of Renewable Energy Sources (RES) therefore represents a major challenge, and several solutions and strategies have been proposed.

Energy storage can be achieved through various technologies, and Energy Storage Systems (ESSs) have been classified into several distinct categories based on their underlying operative principles [139]: (i) Thermal Energy Storage Systems (TESS), (ii) Electrical Energy Storage Systems (EESS), (iii) Chemical Energy Storage Systems (CESS), (iv) Mechanical Energy Storage Systems (MESS), and (v) Electrochemical Energy Storage Systems (ECESS).
Each technology presents its own strengths and weaknesses. EESS (e.g. supercapacitors), for instance, exhibit very high power density, excellent discharge efficiency (>95%), fast response and long lifetime. ECESS (e.g. Li-ion batteries, Na–S batteries, flow batteries), considered major competitors in energy storage applications, combine limited maintenance requirements with high efficiencies (70–80%) and, in some cases, relatively simple construction [140]. However, both EESS and ECESS are characterized by limited energy capacity and short discharge times (approximately 1 min and 2 h, respectively), which make them less suitable for the storage of large amounts of energy over long time horizons [139], [141], [142], [143].

Pumped hydro represents the most widely employed MESS and the leading global energy storage technology, accounting for 67% of the worldwide installed capacity with 181 GW [144]. Its advantages include long operational lifetime, rapid dynamic response, high round-trip efficiency, large energy capacity and low self-discharge. Conversely, its deployment is constrained by high capital investments, long payback times, significant water demand and relevant environmental concerns [139], [145].

With respect to Chemical Energy Storage Systems, hydrogen storage can be regarded as a particularly promising solution, as it contributes to advancing the global agenda towards carbon neutrality [137]. This technology, commonly referred to as “power-to-gas” (PtG), establishes a connection between the electrical grid and the gas grid by converting surplus electricity into a grid-compatible gas, either through hydrogen production via water electrolysis and subsequent methanation with an external carbon source, or through direct hydrogen storage and reconversion by means of fuel cells [146], [147], [148].
When selecting the most suitable energy storage technology, several factors must be considered, among which the possibility of seasonal storage plays a crucial role. In this context, hydrogen offers unique advantages compared to other technologies, since the storage capacity is essentially limited only by the size of the reservoir, and can be further enhanced through compression or liquefaction.

Within this framework, some intrinsic characteristics of solid oxide technology, such as high electrical and combined heat and power efficiencies as well as reversible operation, make it particularly attractive for specific applications in which its drawbacks (e.g. slow start-up time and high operating temperature) are less critical [149]. Reversible solid oxide cells (rSOCs) have therefore been proposed as promising candidates for large-scale and long-term energy storage, as they can operate alternately in electrolysis mode to produce hydrogen and in fuel cell mode to reconvert it into electricity. They offer among the highest overall energy conversion efficiencies currently achievable, with round-trip efficiencies exceeding 70%. Moreover, unlike conventional batteries, the energy capacity of rSOC-based systems can be readily scaled by increasing the hydrogen storage volume, thus decoupling energy capacity from power output [138], [150], [151], [152].

Despite these advantages, several limitations still penalize rSOCs with respect to competing technologies, among which cost and durability represent two major aspects. As reported in [153], in 2017 the capital cost of rSOC systems exceeded 2000 €/kW and the technology maturity was still at demonstration level, while alkaline electrolyzers exhibited lower costs (1000–1200 €/kW) and higher technological readiness. Nevertheless, significant cost reductions are foreseen, with recent studies estimating total system costs in the range 760–917 €/kW [154], [155], and long-term projections by industrial stakeholders predicting values as low as 230 $/kW by 2030 [156].

In addition to cost, long operational lifetime is a fundamental requirement for seasonal energy storage systems, making degradation one of the key aspects to be assessed. The main degradation mechanisms in rSOCs are generally consistent with those observed in conventional SOFC and SOEC operation, including interfacial degradation, chromium poisoning and nickel migration [150], [157], [158], [159], [160], [161]. As evidenced by the extensive body of literature available, this topic has been and continues to be widely investigated.

Most experimental studies on solid oxide cells and stacks reported in the literature are conducted under steady galvanostatic or potentiostatic conditions. Long-term tests on single cells and short stacks have provided valuable insight into intrinsic degradation mechanisms [63], [87], [104], [162], [163], [164], [165], [166], [167], [168]. However, the reported results often exhibit significant dispersion, and conflicting trends between fuel cell and electrolysis operation have been observed. Moreover, the majority of available studies focus on steady-state conditions, with limited attention devoted to realistic dynamic operation.

A research gap concerning the experimental investigation of rSOC systems under more realistic application scenarios can be found, particularly involving variable loads and coupling with renewable energy sources. While constant-load degradation studies have provided fundamental information on material stability, they do not capture the complex stress and degradation pathways arising under fluctuating operating conditions. For this reason, part of this doctoral research is devoted to the experimental investigation of rSOC operation under shifting load scenarios representative of residential applications coupled with photovoltaic generation and hydrogen storage, with the aim of assessing dynamic response, degradation behaviour and control strategies under close-to-real operating conditions.

The research question object of discussion is investigated through dynamic experiments and simulations of an rSOC system coupled with a photovoltaic (PV) plant and a residential load, simulating real-world energy profiles with hourly resolution. The study evaluates the dynamic response, stability, and degradation behavior of the rSOC under variable operating conditions, with particular emphasis on seasonal hydrogen storage and grid independence. This work contributes to the broader discourse on renewable energy integration and flexible storage solutions.

RQ4: *What design strategies can be implemented to maximize the efficiency of rSOC stacks, and how do systems scaled for real-world applications respond in terms of performance and operational reliability?*

The ultimate goal of research on solid oxide cell (SOC) technology is to support its development toward the realization of reliable systems capable of being flexibly deployed across a wide range of application scenarios. The advancement of this technology requires not only an in-depth understanding of the individual components – namely, single cells – but also a comprehensive comprehension of how these elements can be integrated and operated to fulfil specific functions, such as delivering electrical power to end users or producing a defined hydrogen flow rate for industrial applications.

To achieve this objective, it is essential to pursue a progressive scale-up across different system sizes, in order to collect critical information on both the behaviour of the individual components and the operating strategies required for the correct functioning of a real plant. This approach also enables the identification of the interactions among the various subsystems and of the conditions under which they can operate synergistically to optimize the overall system performance and efficiency.

A real-scale system based on solid oxide technology comprises several integrated components designed to ensure stable and efficient operation. The core of the system is the stack module, while auxiliary devices such as superheaters are employed to guarantee that the process gases reach the required temperatures at the stack inlet. In addition, heat exchangers are implemented to recover thermal energy from the hot exhaust streams and preheat the incoming cold gases. This heat recovery strategy reduces the thermal load on the heaters, lowers the overall energy consumption of the system, and consequently enhances its global thermal efficiency.

Within this framework, the present chapter reports preliminary results and considerations on the performance of a reversible solid oxide cell (rSOC) system with a rated power exceeding 10 kW, operated in electrolysis mode (SOEC). The analysis focuses on the evaluation of enthalpy flows and overall system efficiency, and is conducted within the framework of the European research project BeBOP.

The experimental activities were carried out at the VTT Technical Research Centre of Finland, in the context of a research collaboration between the author of this thesis and VTT. Since the project is still ongoing and a dedicated scientific publication is currently in preparation, the level of detail and the amount of quantitative data that can be disclosed in this thesis are necessarily limited. For this reason, the discussion presented herein is intentionally focused on general trends and on a preliminary assessment of the most relevant performance indicators.

Within the broader context of the present doctoral research, this chapter represents a natural extension of the investigations conducted at the single-cell level, providing a transition from laboratory-scale characterization to the operation of a system with quasi-real, pre-commercial power capacity. The results and considerations reported here are intended to highlight the main challenges and opportunities associated with the scale-up of solid oxide technologies, with particular emphasis on system integration, thermal management, and energy efficiency under realistic operating conditions.

2. Materials And Methods

This chapter presents the technical details and methodological approach adopted for the experimental and modeling investigations carried out in this research. The first part of the chapter provides a description of the test benches and the experimental setups used for cell and system-level characterization – with particular attention to the configuration and instrumentation – as well as a discussion on the theoretical and modeling approaches to the use of the experimental data. The experimental setups and the testing campaigns were designed to replicate realistic operating scenarios and enable high-resolution monitoring of electrochemical and thermochemical parameters.

The second part focuses on the analytical techniques employed to evaluate cell performance and system behavior. These include polarization curve measurements (I-V curves), gas chromatography (GC) for gas composition analysis and Electrochemical Impedance Spectroscopy (EIS) for assessing internal resistances and identifying dominant loss mechanisms. Each method was selected to provide complementary insights on the operation, degradation, and efficiency of the Solid Oxide Cell technologies investigated in this thesis.

2.1 SOC single cell test station #1 – multisampling design

The experimental test bench developed at ENEA Casaccia Research Centre, hereafter referred to as *multisampling*, represents an innovative setup designed for the detailed characterization of single solid oxide cells (SOCs). It is designed to enable localized gas sampling along the fuel electrode surface, in order to spatially map gas composition and temperature at multiple points of the cell. This approach provides a significant advancement over traditional analyses, which are typically limited to the measurement of inlet and outlet conditions. By enabling localized diagnostics, this setup allows the investigation of the spatial evolution of chemical and electrochemical reactions along the electrode surface, providing deeper insight into cell behavior and performance. Such information is particularly relevant under electrolysis operation, where the high steam concentration and elevated average current density imposed on the cell lead to strong gradients in gas composition, temperature, current density, and local voltage – factors known to accelerate degradation and reduce performance.

2.1.1 Single cell and test rig design

The test bench was developed at ENEA Casaccia facilities, and a schematic rendering of the system is shown in Figure 10. The ***cell housing*** is made of AISI 310 stainless steel and consists of two parts (fuel-side and air-side), capable of accommodating cells up to 10 x 10 cm^2. Gas inlet and outlet tubes are made of Inconel, a material that forms a stable passivating oxide layer on its surface, effectively preventing chromium evaporation and subsequent contamination of the cell.

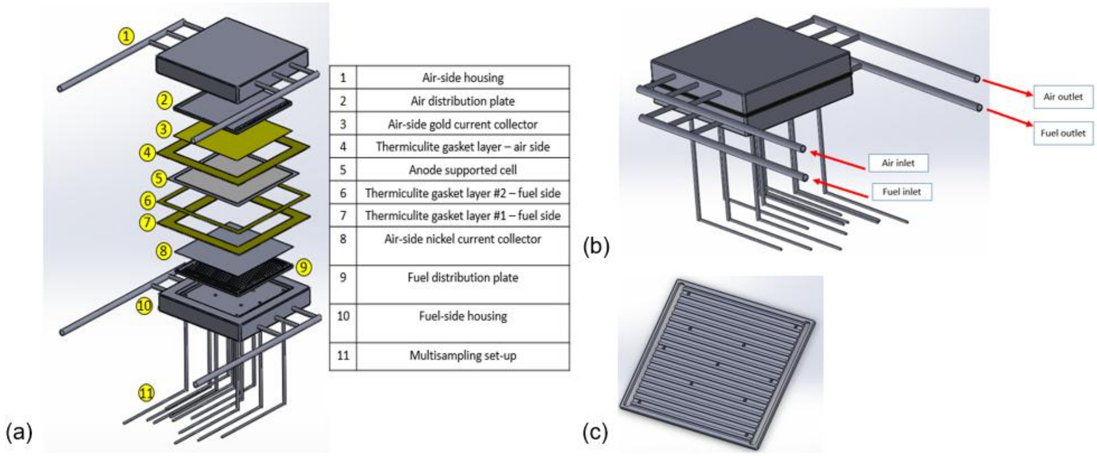

1	Air-side housing
2	Air distribution plate
3	Air-side gold current collector
4	Thermiculite gasket layer – air side
5	Anode supported cell
6	Thermiculite gasket layer #2 – fuel side
7	Thermiculite gasket layer #1 – fuel side
8	Air-side nickel current collector
9	Fuel distribution plate
10	Fuel-side housing
11	Multisampling set-up

***Figure 10**. Exploded view of the multisampling test setup (a); Exploded view of the test setup – focus on the gas flows (b); fuel-side gas distribution plate (c).*

Each side of the housing contains a ***gas distribution plate*** with 11 flow channels designed to distribute the reactant gas uniformly across the cell surface from inlet to outlet. To prevent electrical contact with current collectors and to minimize chromium release, a thin insulating Al_2O_3 coating was deposited on the entire surface of the distribution plates.

On the fuel side, both the housing and the gas distribution plate are equipped with ***11 evenly spaced holes*** enabling multisampling functionality. Through capillary tubes (1/16'') made of AISI 310, small gas samples can be extracted for gas chromatographic analysis, while thermocouples can be inserted to perform localized temperature mapping across the active area. Each capillary line is equipped with an individual valve to prevent gas mixing between sampling points and to minimize pressure drop.
Type K ***thermocouples*** are inserted within the capillaries, located close to the sampling holes, estimated to have a nominal uncertainty of ±1 °C.
The gas analysis is carried out by the Clarus 680 ***GC*** (Perkin Elmer) equipped with a Haysep Q and molecular Sieve 5A column set and a thermal conductivity detector (TCD). The stainless-steel sampling capillaries are trace-heated, as well as all gas inlet lines, and are maintained above 100 °C along their entire length to prevent condensation of water vapor. The sampling flow rate is maintained between 5-10 mL/min per channel, corresponding to less than 2% of the local fuel flow, ensuring negligible perturbation of the electrochemical operation. The chromatograph was calibrated using certified gas mixtures, and the repeatability of the measurements was verified at multiple sampling points. Based on the manufacturer's specifications, the typical accuracy for binary gas mixtures is within ±2–3 vol%, with ±3 vol% adopted as the reference value for error propagation in steam conversion calculations.

Current collectors are placed between the gas distribution plates and the SOC electrodes. They are carefully manufactured to ensure perfectly flat contact surfaces for optimal electrical connection. The fuel-electrode current collector consists of a nickel mesh, while the air-electrode current collector is made of gold. To prevent gas leakage caused by potential surface irregularities, the current collectors are intentionally slightly longer than the housing.

Gas tightness and electrical insulation between components are ensured by three Thermiculite ***gaskets*** (types 866LS, designed by Flexitallic), hand-cut into square frames to match the housing dimensions. Two gaskets are placed between the current collectors and the housing, ensuring both sealing and electrical insulation, while an additional gasket is placed at the cell level to avoid short-circuiting between electrodes and to provide sealing at the active area.

The single-cell housing is inserted into a temperature-programmed ***furnace***, allowing precise control of the operating temperature throughout the test. The eleven capillary sampling tubes emerge from the bottom of the furnace and converge into a multi-stage Valco valve, which sequentially directs the gas from each sampling point to a Perkin Elmer Clarus 680 gas chromatograph.

The test rig is equipped with a complete electrochemical characterization system: a Kikusui PLZ664WA ***electronic load*** connected in series with a Delta Elektronika SM-30-100D ***power supply*** enables the acquisition of polarization curves.

The cell voltage is monitored with a TTi 1604 digital multimeter, while electrochemical impedance spectroscopy (EIS) is performed using a BioLogic BP-300 ***Electrochemical Impedance Analyzer***.

Gas flow is controlled via calibrated mass flow controllers, and on the fuel-side it can be humidified using a ***controlled evaporator mixer*** (CEM) and a liquid flow meter.
At experimental level, the *multisampling* has been used to perform tests on a commercial fuel-electrode-supported solid oxide cell with Ni-YSZ/YSZ/GDC/GDC-LSCF structure, having overall dimensions of 10 × 10 cm^2 and an active area of 81 cm^2. The cell was operated in electrolysis mode under controlled conditions, with the furnace maintaining a constant temperature throughout the entire test campaign.

The concept of a partitioned single cell is depicted in Figure 11. For detailed localized analyses, the fuel electrode is figuratively divided into 11 segments, hence each of them is assigned to each of the sampling points. Areas are divided in accordance with how the sampling points are distributed across the cell and are named after the sampling spot they surround. Surface areas are 3.857 cm^2 for inlet and outlet points, and 11.571 cm^2 for all the other points, resulting in an overall 81 cm^2 area. Table IV reports the distance of each sampling point from the inlet cross section of the cell. Due to the presence of the premixing chamber, the gas enters the cell homogeneously along the y-axis and is distributed over the cell surface through 15 distribution channels. As a result, the total inlet flow to the cell is automatically and uniformly divided among the fictitious segments 1, 2, and 3, each receiving one third of the total flow. Segments 4–8, instead, extend across the entire cell along the y-axis and are therefore exposed to the full inlet flow. Similarly, the outlet segments (9, 10, 11) each receive one third of the total flow. On this basis, a homogeneous gas flow distribution along the cell y-axis is assumed.

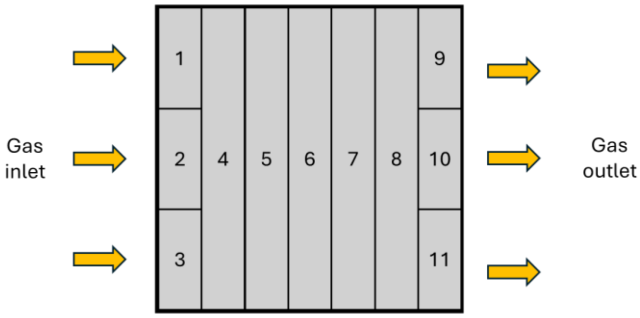

Figure 11. Fictitious partitioning of the fuel electrode into 11 areas, top view.

Table IV: distance of sampling point from the inlet

Sampling point	Distance (mm)
1, 2, 3	9
4	21
5	33
6	45
7	57
8	69
9, 10, 11	81

2.1.2 Single cell preliminary characterization procedures and test campaign definition

Electrical resistance and gas tightness tests are performed on the single cell prior to its standard start-up procedure and reduction, with the leakage resulting to be in the range 2 – 4% of the inlet flow rate (500 mL/min of N_2) – a value considered acceptable to carry on with the tests. Its initial performance is evaluated in fuel cell mode. Silva-Mosqueda et al [169] have already previously conducted an experimental campaign on a Solid Oxide Intermediate Temperature electrode-supported single cell using a similar version of the test bench, effectively validating the current test rig and cell assembly.

Once the benchmark performance is assessed, hence the test bench is validated, the single cell is tested by performing polarization curves, Electrochemical Impedance Spectroscopy (EIS), short-term stability tests (at least 2 hours in stable operation) and gas chromatographic analysis under different operating conditions. In order to map the performance in a wide operating window, tests are run at different:

- Total fuel flow rates (300 – 500 mL/min);
- Fuel compositions (50/50 – 70/30 H_2O/ H_2 %vol)

The electrochemical activity of the electrodes was monitored at a DC bias current of 1 A, with an AC perturbation of 10 mA applied over a frequency range from 10 mHz to 100 kHz.. The I–V curves have been performed taking into account a few constraints: steam utilization below 90% (to avoid induced cell degradation), maximum cell voltage 1300 mV [170], maximum current density 0.5 A/cm^2 (nominal operating point suggested by the manufacturer), scan rate set to 0.1 A/s and a stabilization time of 1 min every time the new current load was reached (e.g. 1 A, 2 A, 3 A, etc.)

In Table V all the experimental conditions tested are summarized, while in Figure 12b the plots of cell voltage in the stabilization process are reported.

***Table V**:* experimental working conditions for the 81 cm^2 electrode-supported single cell

Condition no.	Total fuel flow rate	H_2	H_2O
1	300 mL/min	150 mL/min (50%vol)	150 mL/min (50%vol)
2	500 mL/min	250 mL/min (50%vol)	250 mL/min (50%vol)
3		150 mL/min (30%vol)	350 mL/min (70%vol)

The experimental steps carried out are the following: in OCV conditions one parameter is changed with respect to the previous test (e.g. total flow rate, gas composition, temperature) and sufficient time for the system to stabilize in its new working condition is given; the EIS test is then performed, followed by the IV curve up to a current value at which either the voltage reached 1300 mV (threshold under which the operation in SOEC was considered safe with no forced degradation induced), or Fuel Utilization reached 90%, or a current density of 0.5 A/cm^2 was reached. The cell was then kept at selected load value of 0.235 A/cm^2 (or 19 A) for a minimum of 2h. After the stabilization period under load, the open circuit conditions are restored, and the new parameters of the subsequent tests are set.

The EIS spectra, primarily intended for the preliminary monitoring of cell performance, are shown in Figure 12a. A decrease in polarization resistance is observed with increasing inlet steam content, whereas the ohmic resistance, being unaffected by the feed composition, remains nearly constant in all three cases at a value between 0.20 and 0.25 Ω cm^2.

This value is consistent with other studies conducted on SOECs, such as Wolf et al. [102], whose work reports internal resistance values around 0.2 Ω cm^2. Studies with segmented cells, on the other hand, exhibit ohmic contributions ranging between 0.3 and 0.4 Ω cm^2 per segment, higher than those observed for the full cell due to the complex architecture of the setup, which prevents perfectly flat contact between the segments and the interconnect [115], [116].

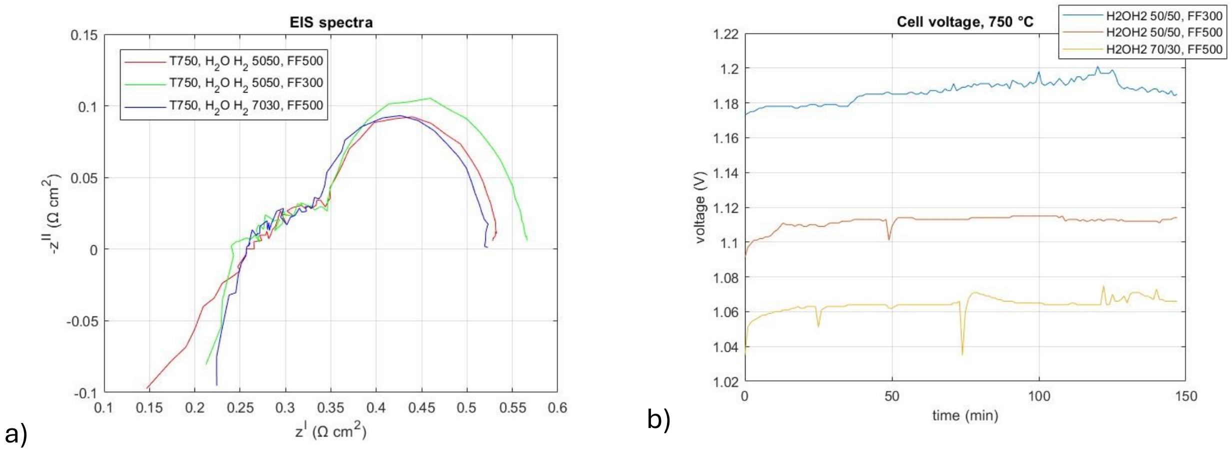

***Figure 12**:* a) EIS spectra for all testing conditions; b) cell voltage versus time in the stabilization process (> 2 h) in all testing conditions.

2.1.3 Cell voltage prediction model (V)

The electrochemical reactions occurring in steam electrolysis (SOE) mode at the electrodes-electrolyte interfaces are presented in Table VI. At the cathode (fuel electrode) steam is reduced to form hydrogen and oxygen ions by gaining electrons coming from the anode. At the anode (air electrode) oxygen ions coming from the cathode migrate through the electrolyte and are oxidized to form molecular oxygen, releasing electrons.

***Table VI**:* electrochemical reactions in steam SOE mode

Where	Reaction
Cathode (fuel electrode)	$H_2O + 2e^- \rightarrow H_2 + O^{2-}$
Anode (air electrode)	$O^{2-} \rightarrow \frac{1}{2}O_2 + 2e^-$
Global reaction	$H_2O \rightarrow H_2 + \frac{1}{2}O_2$

Cell potential, as a function of the current load, can be expressed as [109], [171], [172], [173]:

$$V = V_{Nernst} + \eta_{act} + \eta_{ohm} + \eta_{conc} \tag{24}$$

where V_{Nernst} [V] is the Nernst (reversible) cell potential, η_{act} [V] is the activation polarization, η_{ohm} [V] is the ohmic polarization and η_{conc} [V] is the concentration polarization.
The reversible cell potential is given by the Nernst equation [171], [174]:

$$V_{Nernst} = E_0 - \frac{R \cdot T}{2 \cdot F} \cdot ln\left(\frac{p_{H_2O}}{p_{H_2} \cdot {p_{O_2}}^{0.5}}\right) \tag{25}$$

$$E_0 = 1.253 - 2.416 \cdot 10^{-4} \cdot T \tag{26}$$

where E_0 [V] is the reversible cell potential at standard pressure and temperature, T [K] is the cell temperature, R [J mol^{-1} K^{-1}] is the universal gas constant, F is the Faraday's constant [96487 C/mol] and p_x is the x species partial pressure.

The activation overpotential is split into fuel-electrode and air-electrode overpotential [171]:

$$\eta_{act,fuel} = \frac{2 \cdot R \cdot T}{2\,F} \cdot \sinh^{-1}\left|\frac{i}{2 \cdot \gamma_{fuel} \cdot \left(y_{H_{2,IN}}\right)^A \cdot \left(y_{H_2O_{,IN}}\right)^B \cdot e^{-\frac{E_{act,fuel}}{R \cdot T}}}\right| \tag{27}$$

$$\eta_{act,air} = \frac{2 \cdot R \cdot T}{2\,F} \cdot \sinh^{-1}\left|\frac{i}{2 \cdot \gamma_{air} \cdot \left(y_{O_{2,IN}}\right)^C \cdot e^{-\frac{E_{act,air}}{R \cdot T}}}\right| \tag{28}$$

$$\eta_{act,tot} = \eta_{act,fuel} + \eta_{act,air} \tag{29}$$

where γ_{fuel} and γ_{air} [A / cm^2] are pre-exponential coefficients in exchange current densities, $y_{x,IN}$ [%] are the molar inlet fractions of the species x, A, B and C [-] are the reactant kinetic orders, $E_{act,fuel}$ and $E_{act,air}$ [J / mol] are the activation energies at the fuel- and the air-electrode, i is the current density [A / cm^2].

The ohmic overpotential is defined as in Eq. 30 [171]:

$$\eta_{ohm} = P_1 \cdot T \cdot e^{\frac{P_2}{T}} \cdot i \tag{30}$$

where P_1 [Ω cm^2 K^{-1}] and P_2 [K] are empirical parameters specific for each case study.

The concentration (or diffusion) overpotential may be expressed with Eq. 33 [174]:

$$\eta_{conc,fuel} = -\frac{R \cdot T}{2 \cdot F} \cdot ln\left(1 - \frac{i}{i_{lim}}\right) \tag{31}$$

$$\eta_{conc,air} = -\frac{R \cdot T}{2 \cdot F} \cdot ln\left(1 - \frac{i}{i_{lim}}\right) \tag{32}$$

$$\eta_{conc,tot} = \eta_{conc,fuel} + \eta_{conc,air} \tag{33}$$

where $i_{\lim}$ (A / cm^2) is the limiting current density. In practice, given a certain inlet flow rate and composition, it corresponds to the current density at which 100% of steam conversion is reached.

For the model, the values of the input parameters are summarized in Table VII:

Table VII: values of input parameters in the present study – calculation of cell voltage

Parameter	Value	Reference	Unity
Temperature (T)	1023	-	K
Pre-exponential coefficient – fuel side (γ_{fuel})	5×10^5	[171]	A/cm^2
Pre-exponential coefficient – air side (γ_{air})	5×10^6	[171]	A/cm^2
Molar inlet fraction of H_2 ($y_{H2,IN}$)	30 - 50		%
Molar inlet fraction of H_2O ($y_{H2O,IN}$)	50 - 70		%
Reactant kinetic order (A)	0.5	[171]	-
Reactant kinetic order (B)	0.5	[171]	-
Reactant kinetic order (C)	0.25	[171]	-
Activation energy at the fuel electrode ($E_{act,fuel}$)	10^5	[171]	J / mol
Activation energy at the air electrode ($E_{act,air}$)	1.2×10^5	[171]	J / mol
Empirical parameter (P_1)	1.6×10^{-7}	adapted from [171]	$\Omega\ cm^2\ K^{-1}$
Empirical parameter (P_2)	7500	adapted from [171]	K
Limiting current density (i_{lim})	0.568 – 4.34		A/cm^2

Figure 13 presents the voltage vs current density data obtained from both modeling simulations and experimental measurements, in all of the three working conditions studied. I-V curves exhibit consistent trends across the five different conditions, as both the predicted and measured maximum current input increase as the H_2O mass flow rate on the fuel side rises. The comparison reveals an accurate prediction of the cell voltage by the model, except at very high current densities where the prediction is overestimated (at steam conversion over 80%). This does not undermine the validity of the model because, for the scope of this study, only current densities below or equal to the nominal value (0.25 A/cm^2) will be explored: in this operating range, the maximum relative error is 8 mV (or 6.1%) given by condition no.1 at 0.25 A/cm^2. Moreover, it can be observed that the voltage calculated using the model is systematically higher than the voltage measured experimentally (up to 3 mV).

Since the ideal gas assumption employed in this study (which uses partial pressures instead of fugacities in the calculation of the Nernst potential) is known to be highly accurate at atmospheric pressure [175], this discrepancy may instead be attributed to the method used for calculating the equilibrium constant in the determination of the reversible cell potential. This phenomenon has been reported in the literature for solid oxide cells [176], with discrepancies between the two values reaching up to 5 mV [175]. Another contributing factor may be the actual operating temperature: although the furnace is set to 750 °C, the inlet gases from the tank do not immediately reach the surrounding temperature (T < 750 °C), which, as shown in Eq. 25, leads to an increase in the Nernst potential.

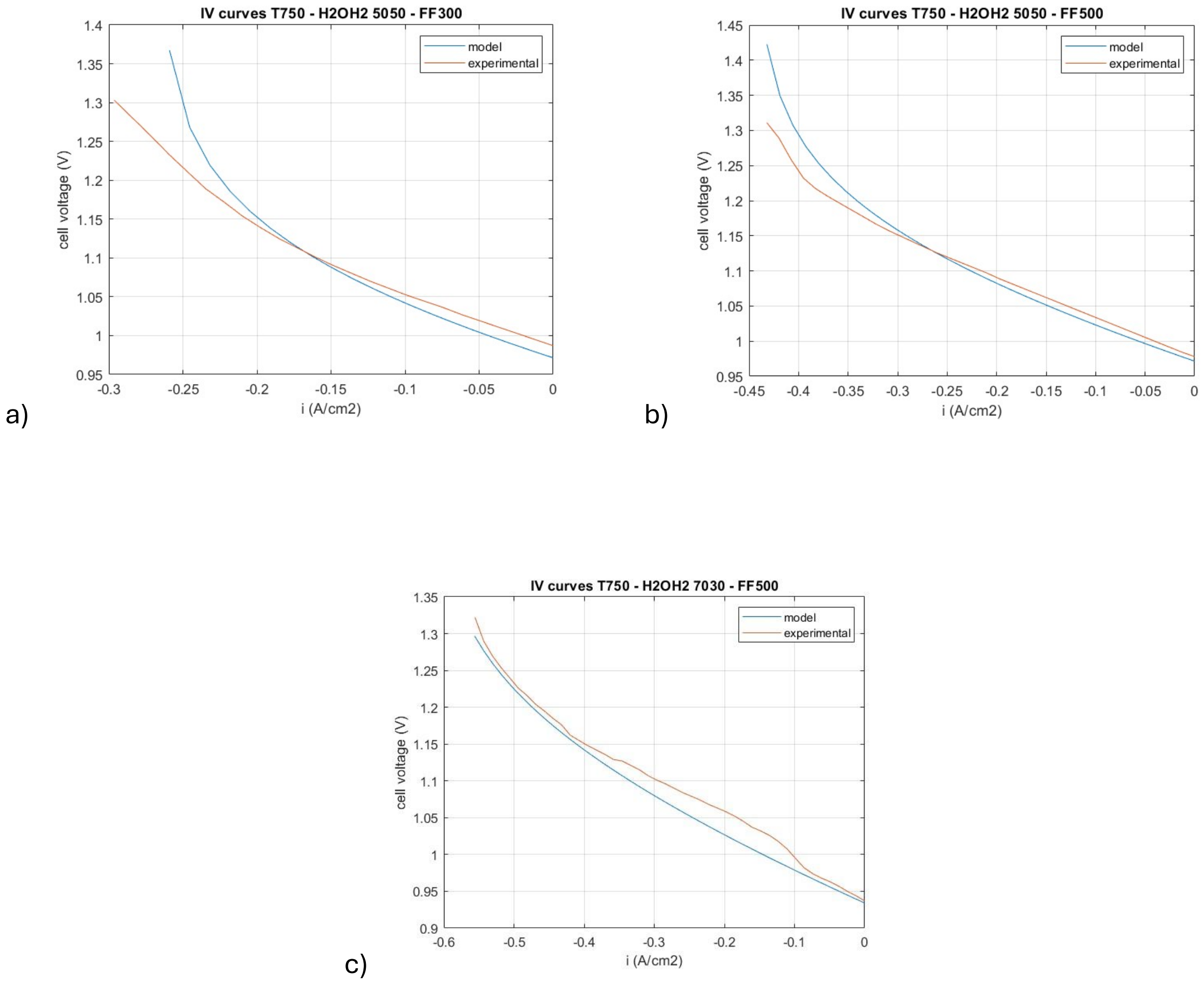

a)

b)

c)

***Figure 13**:* Comparison of experimental and modelled polarization curve; as in Table V: a) condition no.1; b) condition no.2; c) condition no.3.

While the predictive model presented here relies on classical electrochemical kinetics and transport formulations , it is important to note that several additional phenomena may affect the effective electrochemical response of the electrodes. These include local variations in the number and quality of contact points, electrode aspect ratio and morphology, as well as charge and ion accumulation in the vicinity of the electrode–electrolyte interfaces. Moreover, recent works have highlighted the role of surface configurations and reconstructions in Ni-based electrodes, which can induce a p-type semiconducting character and significantly modify the activation and transport processes at the electrode surface [177], [178]. Although these effects are not explicitly included in the present simplified formulation, they represent crucial factors in interpreting deviations between experimental data and theoretical predictions, especially at high current densities or under strongly non-uniform operating conditions.

2.1.4 Determination of local cell current density

The following equation is defined:

$$I(x) = 2 \cdot F \cdot \dot{n}_{H_2O,cons}(x) \tag{34}$$

Where *I* (A) denotes the electric current, *x* (cm) represents the position along the gas flow path, $\dot{n}_{H_2O,cons}$ (mol/s) is the molar flow rate of water vapor consumed at position x. By applying the differentiation method, the following expression is obtained:

$$i(x) = 2 \cdot \frac{F}{W} \cdot \frac{d\dot{n}_{H_2O,cons}(x)}{dx} \tag{35}$$

Where *i* (A/cm^2) is the current density at position x, *W* is the width of the cell's active area. It can be observed that the current density at each point is a function of the cell size and the water conversion rate, which in turn is derived from experimental gas chromatographic data. The finite number of experimental measurements does not allow for a continuous spatial distribution of current density; therefore, a fitting of the experimental points (indicating the water percentage) was performed in order to obtain a continuous curve. From this curve, it is possible to determine the water flow rate converted at each point.

It is also important to note that the equations presented are applicable at the macroscopic scale, and do not account for local phenomena or microstructural states.

2.1.5 Determination of local cell voltage

The validation of the model described in section 2.1.3 serves as a foundation for determining one of the primary objectives of this study: the distribution of cell voltage across its surface. As outlined in section 2.1.1, the cell is divided into 11 smaller segments. These segments can be considered as scaled-down versions of the complete cell, possessing identical characteristics while differing only in size. Consequently, under identical operating conditions, in this simplified approach these segments are considered to retain the same chemical and performance properties as the full cell from which they originate.

This assumption is deemed valid provided that the structural properties of the cell are uniform across its entire surface. Given that the tested cell has not undergone prior experimentation, it is reasonable to assume that its properties remain consistent across all segments. This ensures that the 11 segments described in section 2.1.1 function as true repeating units of the original full cell.

The model from section 2.1.3 is thus modified and the following input parameters, which vary depending on the case study, are provided to it, while the other structural parameters observed in the full cell remain unchanged:

- area of the cell segment
- local current density
- gas flow rate entering the cell segment
- gas composition entering the cell segment
- limiting current density

2.1.6 Determination of local cell temperature

The governing equations to describe the flow field are the Navier-Stokes equations [105], [176], [179]:

$$\frac{\partial \rho}{\partial t} + \nabla(\rho \cdot \vec{v}) = 0 \tag{36}$$

$$\rho \left[\frac{\partial \vec{v}}{\partial t} + (\vec{v} \cdot \nabla) \cdot \vec{v}\right] = -\nabla p + \mu \cdot \nabla^2 \vec{v} + \rho \cdot g \tag{37}$$

$$\rho \cdot c_p \cdot \left[\frac{\partial T}{\partial t} + \vec{v} \cdot \nabla T\right] = k \cdot \nabla^2 T + \dot{q} \tag{38}$$

Eq.13, 14 and 15 are the mass, momentum and energy conservation equations respectively. Some simplifying assumptions are made:

- steady-state condition;
- c_p and h constant within each of the segments into which the full cell is divided;
- heat absorbed/generated constant within each of the segments into which the full cell is divided
- 1D temperature variation (along the x-axis)
- ideal gases
- negligible radiative heat transfer
- constant cell surface temperature

Based on these considerations, the Navier-Stokes equations are significantly simplified, leading to an analytical formulation of the temperature:

$$T_{g,j}(x) = T_s + \left(T_{g0,j} - T_s\right) \cdot e^{\left(\frac{-h \cdot P \cdot x}{\dot{m}_j \cdot c_{p,j}}\right)} - \frac{\dot{Q}_{cell,j} \cdot l}{h \cdot P} \cdot \left(1 - e^{\left(\frac{-h \cdot P \cdot x}{\dot{m}_j \cdot c_{p,j}}\right)}\right) \tag{39}$$

$$\dot{Q}_{cell} = \Delta H \cdot \dot{m}_{H_2O\ conv} - V_{cell} \cdot i \tag{40}$$

Where j is the cell segment object of study, $T_{g,j}(x)$ (K) is the gas temperature across the surface of segment j, T_s (K) is the cell surface temperature, $T_{g0,j}$ (K) is the gas temperature at the inlet of the segment j, h (W/m^2 K) is the convective heat transfer coefficient between cell surface and gas, P (m) is the perimeter of the cross section, x (m) is the distance from the inlet cross section of segment j, $\dot{m}_j$ (kg/s) is the total gas flow rate entering segment j, $c_{p,j}$ (J/kg K) is the specific heat capacity of the gas mixture in segment i, l (m) is the width of the cross section.

Eq. 39 hence indicates the gas temperature, as a function of the distance from the inlet section, in each of the 11 sub-cells.

As reported by Min et al [180], the net amount of heat generation or consumption of a solid oxide cell can be defined with the formulation in Eq. 40, where Q_{cell} (W/cm^2) is the heat generation/consumption, V_{therm} (V) is the thermoneutral voltage, V_{cell} (V) is the cell voltage, ΔH (J/mol) is the enthalpy change during electrochemical reaction at the operating temperature, and $\dot{m}_{H2O\ conv}$ (mol/s) is the molar flow rate of water conversion in the electrochemical reaction. Based on the cell operating voltage, Q_{cell} can be positive or negative, indicating the operating characteristics of the SOEC:

$$\dot{Q}_{cell} \begin{cases} > 0 & \text{endothermic operation} \\ = 0 & \text{thermoneutral operation} \\ < 0 & \text{exothermic operation} \end{cases} \tag{41}$$

An entire subsection must be dedicated to the determination of *h*. The reason why only convective heat exchange has been considered is that, according to literature studies, in the case of planar solid oxide cells, heat transfer between the gas and the cell is predominantly convective, whereas radiative heat exchange becomes non-negligible only in tubular cells [181].

To the best of the authors' knowledge, studies on the magnitude of the convective heat transfer coefficient in planar solid oxide cells are absent in the literature. For this reason, the calculation is performed using formulas and correlations from thermodynamics, as reported below.

The convective heat transfer coefficient is calculated using Eq. 42 [182], [183]:

$$h = \frac{Nu \cdot k}{L} \tag{42}$$

where:

- k (W/m·K) is the thermal conductivity of the gas mixture,
- L (m) is the specific length of the duct,
- Nu is the Nusselt number.

The latter depends on the flow type and the geometry of the gas duct. For rectangular cross-sections, as in the present case study, with a width-to-height ratio of around 3, the corresponding Nu value is 3.96 [182]. Based on these considerations, the value of h is determined: h = 10.74 W / m^2 K.

Table VIII: values of parameters– thermal analysis

Parameter	value	unity
Nusselt number (*Nu*)	3.96	-
Thermal conductivity of gas mixture (*k*)	0.244	W/m K
Width of channels (w)	0.0047	m
Height of channels (H)	0.0016	m
Specific length of channels (*L*)	0.09	m
Width to height ratio *(w/H)*	2.95	-
Hydraulic diameter of channels *(D_h)*	0.0024	m
Gas velocity *(v)*	0.06 (case 1) – 0.1 (case 2-3)	m/s
Dynamic viscosity *(μ)*	$3.624 \cdot 10^{-5}$	Pa · s
Gas density *(ρ)*	0.0426	kg/m^3
Number of channels *(n)*	11	-
Reynolds number *(Re)*	0.17 (case 1) – 0.28 (case 2-3)	-

Table VIII reports the values of the parameters used for the thermal analysis. It is important to note that the value of *h* varies with the composition of the gas mixture, which becomes increasingly rich in H_2 and less rich in H_2O as the gas progresses. However, since the impact of this variation on the final result would not be significant and to avoid complicating the calculations, given the purpose of the work, *h* has been determined considering the inlet gas mixture.

The average gas velocity was estimated from the definition of volumetric flow rate, a known parameter:

$$Q = v \cdot w \cdot H \cdot n \tag{43}$$

Where *Q (m^3/s)* is the volumetric flow rate.

Reynolds number is reported in Table VIII as well, and is determined as follows:

$$Re = \frac{\rho \cdot v \cdot D_h}{\mu} \tag{44}$$

Since the Reynolds number is, for all case studies, well below the threshold for the flow to be considered turbulent [184], it can be concluded that the flow is assumed to be laminar.

2.2 SOC short stack test station

Part of the experimental campaigns object of study of the present thesis was conducted using the short-stack test bench at the ENEA Casaccia Research Centre, which was specifically designed to allow detailed electrochemical, gas and thermal analysis of intermediate-temperature SOC short-stacks, in the framework of the European project SO-FREE. The setup enables the evaluation of overall stack performance under precisely controlled stationary operating conditions. As a laboratory replica of the actual SOFC stack module (5 kW class, 180-cell, 121 cm^2/cell) manufactured by Elcogen which will be integrated in the prototype CHP system in the SO-FREE project, the stack employed for the experiments is a 15-fuel electrode-supported-cell model (manufacturer: Elcogen, model: E350) with an active area of 121 cm^2 per cell. The stack features a closed air/fuel architecture, in which manifold structures provide individual gas access to each cell. Insulation between adjacent cells is ensured by pre-mounted glass-based sealings, and stack compression is applied through an external spring-based system, with initial pre-compression performed via a dedicated transfer unit prior to installation in the furnace. A picture of the stack integrated in the test station is reported in Figure 14a, while Figure 14b shows the stack configuration and flow field scheme.

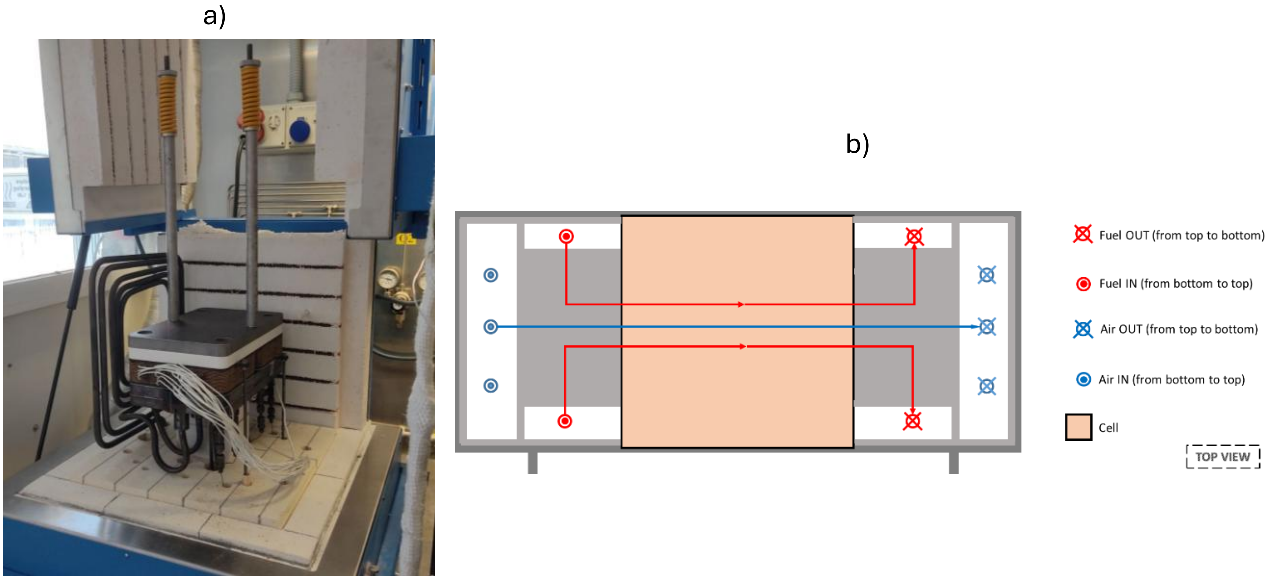

Figure 14: *a) Stack Elcogen E350 integrated in the short-stack test station at ENEA facilities; b) Elcogen E350 stack configuration and flows directions, top view*

Figure 15 reports the P&ID of the test station: the fuel gases are supplied from high-pressure cylinders located outside the laboratory and depressurized in two stages using pressure-reducing valves, first to approximately 10 bar and then to 2 bar. Each gas line is connected to a dedicated mass flow controller (MFC) that delivers the gas to the stack at near-atmospheric pressures. The air supply is drawn from the centralized facility network, with a relative humidity of approximately 13%, and is compressed, filtered, and pressure-regulated through a primary and backup compressor system to ensure reliable operation.

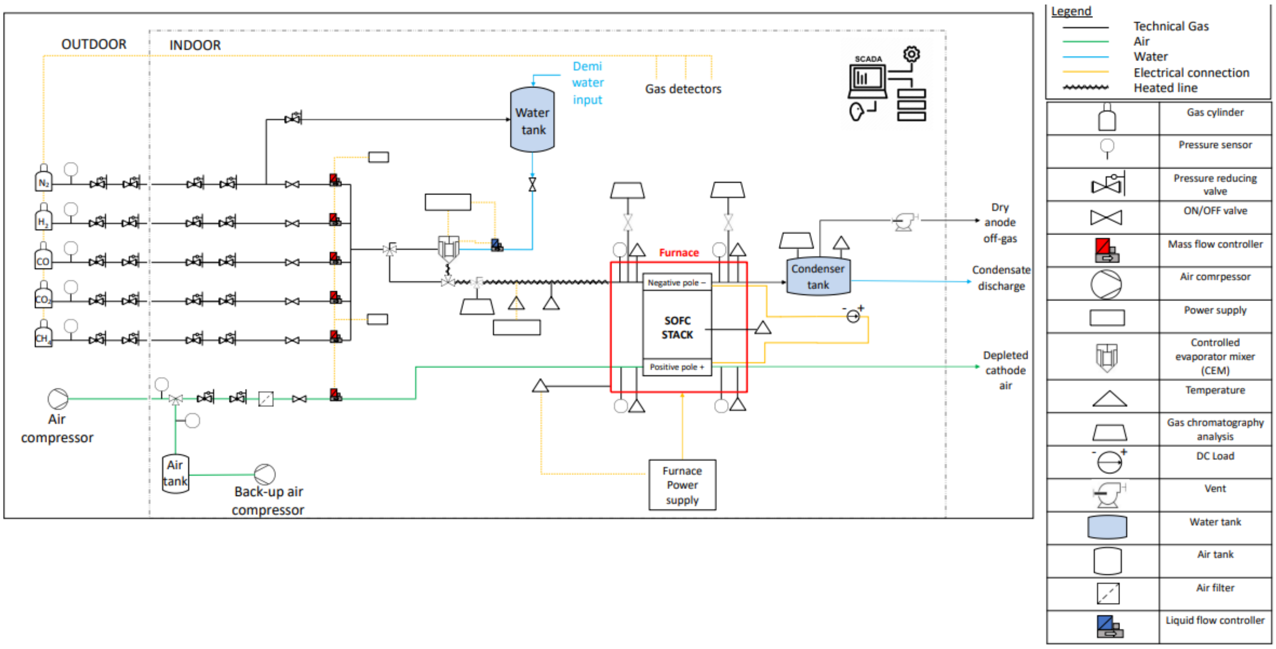

Figure 15. *P&ID of the short-stack test station at ENEA facilities*

Distilled water is stored in a 10 L pressurized tank connected to the nitrogen line at 2 bar, which ensures proper flow to the Liquid Flow Controller (LFC), responsible for measuring water flow toward the CEM. The CEM (Bronkhorst W300B) enables precise mixing of fuel gases and steam, with water vapor flow rates ranging from 17 g/h to 1000 g/h. Within the CEM, water is pre-heated to approximately 120 °C to guarantee complete vaporization before entering the externally heated lines that deliver the mixture to the stack inlet. Trace heating along all gas lines prevents condensation, ensuring a stable gas composition and preventing blockages or disturbances in fuel delivery.

The short-stack is housed in a temperature-programmed ***furnace*** (IEN FCF 64/90/spec) with an internal volume of 400 x 395 x 400 mm and a maximum power of 5.2 kW, capable of reaching temperatures up to 900 °C. The furnace ensures uniform thermal distribution, maintaining the stack at the desired operating temperature throughout testing. The fuel and oxidant gases evolve through the stack in a co-flow configuration.

Thermocouples and ***pressure sensors*** are located in all critical points of the fuel and air inlet and outlet manifolds to monitor gas temperature and pressure in real time. Exhaust gas from the fuel-side passes through a condenser tank to remove water formed by electrochemical oxidation before being vented externally via a suction fan, while air-side exhaust is vented directly outside the laboratory.

Two gas-sampling points are installed at the stack inlet and outlet to allow verification of inlet gas composition and monitoring of reaction products. The outlet samples are analyzed using a Perkin Elmer Clarus 680 ***gas chromatograph*** equipped with a Thermal Conductivity Detector (TCD), Hayesep Q, and Molecular Sieve 5A columns. Multiple samplings are performed for each measurement, and the reported values correspond to the averages. The calculated statistical relative error for each measurement was less than 5%, ensuring reliable monitoring of the chemical reactions within the stack.

Electrochemical measurements are carried out with a Kikusui PLZ664WA ***electronic DC load***, operated in galvanostatic mode, connected in series with a Delta Elektronika SM-30-100D ***power supply***. A shunt resistor allows current measurement via Ohm's law, and a switch enables polarity reversal to operate the stack in either fuel cell (SOFC) or electrolysis (SOEC) mode. Voltages of each single cell within the stack are monitored through Ni-Cr cables, while total stack voltage and auxiliary signals are acquired using a National Instruments ***CompactDAQ system*** (cDAQ-9174), incorporating two NI 9213 modules for thermocouple acquisition and one NI 9205 module for voltage measurements, providing 54 acquisition channels in total.

Electrochemical impedance spectroscopy (EIS) is performed using a BioLogic BP-300 analyzer, allowing detailed characterization of the stack's dynamic and resistive behavior.

The facility integrates precise thermal management, controlled reactant and steam delivery, and extensive in-operando diagnostics, enabling reproducible and high-fidelity testing of intermediate-temperature SOFC short-stacks. Its modular design, combined with real-time monitoring of electrochemical, thermal, and gas-composition parameters, ensures safe and reliable operation while providing detailed insight into stack performance under a wide range of operating conditions.

A SOFC short stack has been analysed experimentally under different fuel gas compositions. As part of the collaboration for the project, The stack inlet gas composition is defined by an in-house simulation tool developed by AVL for system-level simulation considering the three fresh feedstock scenarios (100% NG, 67% H_2 blend in NG and 100% H_2) which resemble possible short-, medium- and long-term gas grid transition scenarios.

The medium-term scenario designed in this experimental campaign foresees the ratio H_2/NG = 2 since the aim is to consider a fuel composition very rich in hydrogen, but at the same keeping it far from the 100% H_2 scenario itself. Moreover, had a lower hydrogen content been used, the post-reforming gas composition would have been way too similar to the 100% NG scenario, making the two set of tests too aligned to each other and giving the study less scientific contribution.

It is worth noting that, according to the system architecture and operation strategy, the gas stream flow rate and composition entering the SOFC stack can be very different from the fresh fuel feedstock due to the recirculation of off-gas and pre-reforming steps.

The simulation is based on preliminary performance data estimations provided by the SOFC stack manufacturer in different FU and temperature in part-/full-load conditions. From an overall system integration point of view, the system level parameters (e.g. RR, single-pass FU) are tailored to maximize the output system level efficiency, while taking into account specific constraints related to both the SOFC stack (i.e. carbon deposition boundaries, maximum stack current and single-pass FU, minimum cell/stack voltages, etc.) and the overall system integration (no additional steam requirement for the external reformer reactor, compatible temperature levels for the balance of plant components, maximum global FU, etc.) [185].

The flow rates and gas composition of fresh fuel, recirculated off-gas and stack inlet fuel are calculated by the model and strictly depend on the system architecture and operating strategy. In particular, the

RR controls the amount of steam recirculated to the external pre-reformer – determining the degree of external fuel pre-processing following the stoichiometry of the reforming and shift reactions other than maintaining the S/C ratio at reasonable levels (indicated by the stack manufacturer) at the inlet of the stack.

The short stack sample is tested prior to cold tests (electrical resistance and gas leakage tests) followed by a standard start-up procedure [186] to reduce and initially load the stack. Once the benchmark performance is compared with the values obtained by the manufacturer in the factory acceptance tests (validating the test bench), the short stack is tested by performing polarization curves and short-term stability tests (>2-10 hours in stable conditions with <0.5 K variation in temperature) under the different operating conditions obtained by the simulation results. Thermal and pressure fuel/air inlet/outlet measurements are monitored continuously throughout the tests. For each gas composition several parametric tests are run at different single-pass FU (50 %/ 60 %/ 70 %) and temperatures (640 °C/660 °C/710 °C), in order to map the short stack performance in a wide range of operating windows. The characterization tests are carried out following standard procedures and protocols [186], following general indications given by IEC 62282-7-2:2021 [187].
The design of the test campaign takes into account different constraints and trade-offs such as project requirements (fresh fuel feedstock, compositions, stationary performance measurements for >2-10 h, etc.), wide variation ranges for each testing parameter/condition (e.g. temperature, FU, current loading), technical limitations of the stack (degree of internal reforming, S/C ratio, O/C ratio, etc.), test/total campaign duration, technical limitations related to the testing facility infrastructures (minimum/maximum mass flow controllers rangeability, minimum/maximum steam supply system rangeability, available instrumentation, etc.), etc.

The short-stack performance has been evaluated in three different scenarios:

- 100% NG
- 67% H_2 + NG
- 100% H_2

At laboratory-level, the stack is fed with the gas whose flow rate and composition are obtained by the simulation in a certain operating condition, and that already takes into account the mixing of the fresh fuel and the recirculated gas.

Let us remind ourselves the three main reactions (electro-oxidation of hydrogen, steam methane reforming and water gas shift respectively) that occur in a SOFC:

$$H_2 + \frac{1}{2}O_2 \leftrightarrow H_2O \tag{45}$$

$$CH_4 + H_2O \leftrightarrow CO + 3H_2 \tag{46}$$

$$CO + H_2O \leftrightarrow CO_2 + H_2 \tag{47}$$

Table IX: System-level and stack-level inlet gas compositions and flow rates.

System-level inlet composition ($\%_{vol}$)	**Temperature (°C)**	**RR (%)**	**Load point**	**Stack-level inlet composition ($\%_{vol}$)**				
				H_2	**H_2O**	**CO**	**CO_2**	**CH_4**
100% H_2	640-660-710	50.0	30 A	59.2	40.8	0	0	0
67%H_2 + NG	640-660-710	45.0	30 A	29.2	42.4	1.0	8.3	19.0
100% NG	640-660-710	72.5	30 A	17.7	42.1	2.0	28.9	9.0

	System-level inlet flow rates (Nl/min)			**Stack-level inlet flow rates (Nl/min)**				
	Fuel Utilization (FU)	**H_2**	**CH_4**	**H_2**	**H_2O**	**CO**	**CO_2**	**CH_4**
100% H_2	50 %	5.3	0	6.28	4.32	0	0	0
	60 %	4.42	0	5.23	3.60	0	0	0
	70 %	3.79	0	4.48	3.09	0	0	0
67%H_2 + NG	50 %	1.77	0.88	1.72	2.50	0.06	0.48	1.12
	60 %	1.48	0.73	1.43	2.08	0.05	0.41	0.93
	70 %	1.27	0.63	1.23	1.78	0.04	0.35	0.80
100% NG	50 %	0	1.18	1.98	4.72	0.22	3.24	1.00
	60 %	0	0.98	1.65	3.93	0.19	2.70	0.84
	70 %	0	0.85	1.42	3.37	0.16	2.31	0.72

Table IX reports the inlet compositions, both at system and stack level. Stack inlet compositions for 100% NG and 67%H_2 + NG cases are generally representative of a reformate gas in which most of the CH_4 has been converted producing H_2 and CO. The resulting CO has also almost fully converted to CO_2 via shift reaction (remaining CO below 5% for both cases and CO_2 content above 28% for the 100% NG case and above 8% for the 67% H_2 + NG case). Although both reforming and shift reactions consume a considerable amount of H_2O, a significant amount of H_2O is still present in the stack inlet composition (around 35-45%). Instead, for the 100% H_2 case the stack inlet composition is only composed of H_2 and H_2O resulting from the recirculation of the anode off-gas for global FU increase purposes.

With the aim of increasing the overall system fuel utilization (and therefore system efficiency), significant amount of steam is present in the stack inlet composition (around 40%) due to anode off-gas recirculation. In all cases a very small amount of N_2 is obtained from the simulation (<0.5 %), which is neglected in the testing phase.

A low H_2 content blend scenario (e.g. 20% H_2 + NG) is excluded from the experimental campaign since, given the high RR and evolution of the gas mixture to thermodynamic equilibrium in the external reformer, the flow rate and composition at the stack inlet are very similar (with differences within 5 %) respect to the 100% NG feedstock case, which did not justify an additional set of experiments.

It can be observed that at nominal conditions (30 A, 660°C) the 100% H_2 and 67% H_2 + NG scenarios show lower RR since there is lower to no steam requirement for fuel pre-processing. On the other hand, the 100% NG scenario requires the highest RR in order to provide enough steam at the external reformer to convert the higher input amount of CH_4 in the fresh fuel. Higher RR entails a higher global system FU since more fuel is being re-used internally to the system.

Some more definitions are necessary, given in the table and equations below:

Table X: Basic definitions

Symbol	Description	Unit of measurement
c_p	Specific heat at constant pressure	kJ/Nm^3
CHP	Combined heat and power	-
FRR	Fuel Reaction Rate	*Nl/min*
FU_{th}	Fuel utilization (theoretical)	-
FU_{exp}	Fuel utilization (experimental)	-
GC	Gas Chromatography	-
IT-SOFC	Intermediate-Temperature SOFC	-
LHV	Lower heating value	kWh/Nm^3
NG	Natural Gas	-
O/C	Oxygen to Carbon ratio	-
OCV	Open Circuit Voltage	*V*
P_{el}	Electrical power produced	*W*
$P_{IN\,stack}$	Chemical power – stack inlet	*W*
$P_{IN\,system}$	Chemical power – system inlet	*W*
$\dot{Q}$	Flow rate	*Nl/min*
RR	Recirculation rate	-
S/C	Steam to Carbon ratio	-
SMR	Steam Methane Reforming	-
SOFC	Solid Oxide Fuel Cell	-
SRU	Single Repeating Unit	-
TCD	Thermal Conductivity Detector	-
WGS	Water Gas Shift	-
α	Steam methane reforming rate	-
β	Water gas shift rate	-

η	Efficiency	-

$$\alpha_{exp} = \frac{\dot{Q}_{CH4\ IN} - \dot{Q}_{CH4\ OUT}}{\dot{Q}_{CH4\ IN}} \cdot 100 \tag{48}$$

$$\beta_{exp} = \frac{\dot{Q}_{CO\ TOT} - \dot{Q}_{CO\ OUT}}{\dot{Q}_{CO\ TOT}} \cdot 100 \tag{49}$$

$$\dot{Q}_{CH4\ reacted} = \dot{Q}_{TOT\ IN} \cdot \frac{\%CH4_{IN} - \%CH4_{OUT}}{1 + 2 \cdot \%CH4_{OUT}} \tag{50}$$

$$\dot{Q}_{CO\ generated} = \dot{Q}_{CH4\ reacted} = SMR_{exp} \cdot \dot{Q}_{CH4\ IN} \tag{51}$$

$$\dot{Q}_{CO\ TOT} = \dot{Q}_{CO\ IN} + \dot{Q}_{CO\ generated} \tag{52}$$

$$\dot{Q}_{CO\ OUT} = \dot{Q}_{TOT\ OUT} \cdot \%CO_{OUT} \tag{53}$$

$$\dot{Q}_{TOT\ OUT} = \dot{Q}_{TOT\ IN} + 2 \cdot \dot{Q}_{CH4\ reacted} \tag{54}$$

$$FU_{stack\ theoretical} = \frac{\dot{Q}_{H2\ FRR}}{\dot{Q}_{H2\ IN\ stack} + \dot{Q}_{CO\ IN\ stack} + 4 \cdot \dot{Q}_{CH4\ IN\ stack}} \cdot 100 \tag{55}$$

$$FU_{stack\ experimental} = \frac{\dot{Q}_{H2\ FRR}}{\dot{Q}_{H2\ IN\ stack} + WGS_{exp} \cdot \dot{Q}_{CO\ IN\ stack} + 4 \cdot SMR_{exp} \cdot \dot{Q}_{CH4\ IN\ stack}} \cdot 100 \tag{56}$$

$$FU_{system\ theoretical} = \frac{\dot{Q}_{H2\ FRR}}{\dot{Q}_{H2\ IN\ system} + \dot{Q}_{CO\ IN\ system} + 4 \cdot \dot{Q}_{CH4\ IN\ system}} \cdot 100 \tag{57}$$

$$FU_{system\ experimental} = \frac{\dot{Q}_{H2\ FRR}}{\dot{Q}_{H2\ IN\ system} + WGS_{exp} \cdot \dot{Q}_{CO\ IN\ system} + 4 \cdot SMR_{exp} \cdot \dot{Q}_{CH4\ IN\ system}} \cdot 100 \tag{58}$$

α and β (Eq. 48 and 49) are the experimental Steam Methane Reforming (SMR) rate and Water Gas Shift (WGS) rate, therefore they indicate the percentage of CH_4 and CO that takes part in the respective reaction. The outlet flow rates are not directly obtainable, so it is necessary to trace their value through the GC outlet composition data. When calculating β, $\dot{Q}_{CO\ TOT}$ is the value that accounts for both the CO fed to the stack and the CO originated by the conversion of methane.
Considering that the SMR reaction (Eq. 46) is the only one that causes an increase of volume (for each mole of CH_4, 2 moles of reactants are consumed and 4 moles of products are generated), the total outlet flow rate can be calculated as reported in Eq. 54.

As described in the equations above, four definitions of fuel utilization (FU) are given: the experimental FU takes into account the amount of hydrogen present in the stack (considering the actual conversion

of CO and CH_4 into H_2 – through water gas shift and methane reforming respectively), whereas the theoretical FU considers the complete occurrence of the same reactions (thus α and β are set to 1).
Regarding the FU, in this work it has been defined based on hydrogen, as the ratio amount of hydrogen electrochemically consumed by the reaction (dependent on the current) with respect to total amount of hydrogen fed to the stack. This last term is obtained considering the complete conversion of CO and CH_4 into H_2.
Thus, based on the fuel gas input/output, current, voltage and power outputs of the SOFC stack, different formulations of the conversion efficiency can be considered at stack and system level [188], [189]. For this specific campaign, only the electrical efficiency is considered since the thermal efficiency is not assessed in the experimental tests.

The definitions of the efficiency given in this work are 18 in total, and are now divided into 3 sections; in each section 6 formulations are reported, 3 of them at stack-level and 3 at system-level. All of them differ exclusively in how the inlet chemical power is defined:

$$\eta_{STACK\,w/o\,FU} = \frac{P_{el}}{P_{IN\,STACK}} = \frac{P_{el}}{\dot{Q}_{H2\,stack} \cdot LHV_{H2} + \dot{Q}_{CO\,stack} \cdot LHV_{CO} + \dot{Q}_{CH4\,stack} \cdot LHV_{CH4}} \tag{59}$$

$$\eta_{STACK\,w/FU_{th}} = \frac{P_{el}}{P_{IN\,STACK} \cdot FU_{th}} = \frac{P_{el}}{\left(\dot{Q}_{H2\,stack} \cdot LHV_{H2} + \dot{Q}_{CO\,stack} \cdot LHV_{CO} + \dot{Q}_{CH4\,stack} \cdot LHV_{CH4}\right) \cdot FU_{stack\,th}} \tag{60}$$

$$\eta_{STACK\,w/FU_{exp}} = \frac{P_{el}}{P_{IN\,STACK} \cdot FU_{stack\,exp}} = \frac{P_{el}}{\left(\dot{Q}_{H2\,stack} \cdot LHV_{H2} + \dot{Q}_{CO\,stack} \cdot LHV_{CO} + \dot{Q}_{CH4\,stack} \cdot LHV_{CH4}\right) \cdot FU_{stack\,exp}} \tag{61}$$

$$\eta_{SYSTEM} = \frac{P_{el}}{P_{IN\,SYSTEM}} = \frac{P_{el}}{\dot{Q}_{H2\,system} \cdot LHV_{H2} + \dot{Q}_{CO\,system} \cdot LHV_{CO} + \dot{Q}_{CH4\,system} \cdot LHV_{CH4}} \tag{62}$$

$$\eta_{SYSTEM\,w/FU_{th}} = \frac{P_{el}}{P_{IN\,SYSTEM} \cdot FU_{system\,th}} = \frac{P_{el}}{\left(\dot{Q}_{H2\,system} \cdot LHV_{H2} + \dot{Q}_{CO\,system} \cdot LHV_{CO} + \dot{Q}_{CH4\,system} \cdot LHV_{CH4}\right) \cdot FU_{system\,th}} \tag{63}$$

$$\eta_{SYSTEM\,w/FU_{exp}} = \frac{P_{el}}{P_{IN\,SYSTEM} \cdot FU_{system\,exp}} = \frac{P_{el}}{\left(\dot{Q}_{H2\,system} \cdot LHV_{H2} + \dot{Q}_{CO\,system} \cdot LHV_{CO} + \dot{Q}_{CH4\,system} \cdot LHV_{CH4}\right) \cdot FU_{system\,exp}} \tag{64}$$

The first set of equations (Eq. 59 – 64) are characterized by a definition of inlet chemical power of each species separately, which means that the fuel gases flow rates (CO, H_2 and CH_4) are multiplied by their respective lower heating values.
In particular, in the stack-level formulations, the stack-level gas composition is considered; in the system-level formulations, the system-level gas composition is considered instead.

Both at stack- and system-level, the first formulation (Eq. 59 and Eq. 62) is calculated based on the total inlet/outlet fuel gas flow rate – thus is strongly limited by the single pass FU since the unreacted fuel at the outlet results in unused chemical energy.
Since in reality the off-gas is recirculated within the system back to the stack, the efficiency can be re-assessed with the second formulation (Eq. 60 and Eq. 63) based on the actual reacting fuel, net of the single-pass FU conditions of the specific test. Here the theoretical FU is used, which considers the complete occurrence of SMR and WGS reactions. In this way the SOFC stack efficiency is evaluated based on the reacting fuel, providing information on the actual process efficiency.

A third formulation of the stack efficiency can be considered (Eq. 61 and Eq. 64), in which the experimental FU is employed: the gas chromatography analysis at the stack outlet allows to know the exact amount of unreacted CO and CH_4, thus evaluate the amount of H_2 actually available within the stack for its electrochemical conversion. The incomplete conversion of CO and CH_4 implies a lower hydrogen content in the reacting gas mixture compared to the complete conversion-scenario, thus FU_{exp} appears to be always higher than FU_{th}.

$$\eta_{STACK\ w/o\ FU\ H2\ equivalent} = \frac{P_{el}}{P_{IN\ STACK}} = \frac{P_{el}}{\left[\dot{Q}_{H2\ stack} + \dot{Q}_{CO\ stack} + 4 \cdot \dot{Q}_{CH4\ stack}\right] \cdot LHV_{H2}} \tag{65}$$

$$\eta_{STACK\ w/FU_{th}\ H2\ equivalent} = \frac{P_{el}}{P_{IN\ STACK} \cdot FU_{th}} = \frac{P_{el}}{\left[\dot{Q}_{H2\ stack} + \dot{Q}_{CO\ stack} + 4 \cdot \dot{Q}_{CH4\ stack}\right] \cdot LHV_{H2} \cdot FU_{stack\ th}} \tag{66}$$

$$\eta_{STACK\ w/FU_{exp}\ H2\ equivalent} = \frac{P_{el}}{P_{IN\ STACK} \cdot FU_{stack\ exp}} = \frac{P_{el}}{\left[\dot{Q}_{H2\ stack} + \dot{Q}_{CO\ stack} + 4 \cdot \dot{Q}_{CH4\ stack}\right] \cdot LHV_{H2} \cdot FU_{stack\ exp}} \tag{67}$$

$$\eta_{SYSTEM\ H2\ equivalent} = \frac{P_{el}}{P_{IN\ SYSTEM}} = \frac{P_{el}}{\left[\dot{Q}_{H2\ system} + \dot{Q}_{CO\ system} + 4 \cdot \dot{Q}_{CH4\ system}\right] \cdot LHV_{H2}} \tag{68}$$

$$\eta_{SYSTEM\ w/FU_{th}\ H2\ equivalent} = \frac{P_{el}}{P_{IN\ SYSTEM} \cdot FU_{system\ th}} = \frac{P_{el}}{\left[\dot{Q}_{H2\ system} + \dot{Q}_{CO\ system} + 4 \cdot \dot{Q}_{CH4\ system}\right] \cdot LHV_{H2} \cdot FU_{system\ th}} \tag{69}$$

$$\eta_{SYSTEM\ w/FU_{exp}\ H2\ equivalent} = \frac{P_{el}}{P_{IN\ SYSTEM} \cdot FU_{system\ exp}} = \frac{P_{el}}{\left[\dot{Q}_{H2\ system} + \dot{Q}_{CO\ system} + 4 \cdot \dot{Q}_{CH4\ system}\right] \cdot LHV_{H2} \cdot FU_{system\ exp}} \tag{70}$$

In the second set of equations (Eq. 65 – 70) the inlet chemical power is calculated in relation on a hydrogen equivalent basis. The hydrogen-equivalent flow rate is considered, instead of the flow rate of each gas: from the SMR and WGS reactions (Eq. 46 – 47) it is possible to notice that, in volume, the H_2

formed in the WGS reaction is the same as the CO reacting. In the SMR reaction the H_2 flow rate generated is 4 times higher than the flow rate of the reacting gas. Complete conversion of CO and CH_4 is assumed.

$$\eta_{STACK\ w/o\ FU\ chem\ conv} = \frac{P_{el}}{P_{IN\ STACK}} = \frac{P_{el}}{\left[\dot{Q}_{H2\ stack} + WGS_{exp} \cdot \dot{Q}_{CO\ stack} + 4 \cdot SMR_{exp} \cdot \dot{Q}_{CH4\ stack}\right] \cdot LHV_{H2}} \tag{71}$$

$$\eta_{STACK\ w/FU_{th}\ chem\ conv} = \frac{P_{el}}{P_{IN\ STACK} \cdot FU_{th}} = \frac{P_{el}}{\left[\dot{Q}_{H2\ stack} + WGS_{exp} \cdot \dot{Q}_{CO\ stack} + 4 \cdot SMR_{exp} \cdot \dot{Q}_{CH4\ stack}\right] \cdot LHV_{H2} \cdot FU_{stack\ th}} \tag{72}$$

$$\eta_{STACK\ w/FU_{exp}\ chem\ conv} = \frac{P_{el}}{P_{IN\ STACK} \cdot FU_{stack\ exp}} = \frac{P_{el}}{\left[\dot{Q}_{H2\ stack} + WGS_{exp} \cdot \dot{Q}_{CO\ stack} + 4 \cdot SMR_{exp} \cdot \dot{Q}_{CH4\ stack}\right] \cdot LHV_{H2} \cdot FU_{stack\ exp}} \tag{73}$$

$$\eta_{SYSTEM\ chem\ conv} = \frac{P_{el}}{P_{IN\ SYSTEM}} = \frac{P_{el}}{\left[\dot{Q}_{H2\ system} + WGS_{exp} \cdot \dot{Q}_{CO\ system} + 4 \cdot SMR_{exp} \cdot \dot{Q}_{CH4\ system}\right] \cdot LHV_{H2}} \tag{74}$$

$$\eta_{SYSTEM\ w/FU_{th}\ chem\ conv} = \frac{P_{el}}{P_{IN\ SYSTEM} \cdot FU_{system\ th}} = \frac{P_{el}}{\left[\dot{Q}_{H2\ system} + WGS_{exp} \cdot \dot{Q}_{CO\ system} + 4 \cdot SMR_{exp} \cdot \dot{Q}_{CH4\ system}\right] \cdot LHV_{H2} \cdot FU_{system\ th}} \tag{75}$$

$$\eta_{SYSTEM\ w/FU_{exp}\ chem\ conv} = \frac{P_{el}}{P_{IN\ SYSTEM} \cdot FU_{system\ exp}} = \frac{P_{el}}{\left[\dot{Q}_{H2\ system} + WGS_{exp} \cdot \dot{Q}_{CO\ system} + 4 \cdot SMR_{exp} \cdot \dot{Q}_{CH4\ system}\right] \cdot LHV_{H2} \cdot FU_{system\ exp}} \tag{76}$$

The definitions given in the third set of equations (Eq. 71 – 76) are more accurate than those in the second set, since the rate of conversion of CO and CH_4 is included in the calculation of the inlet chemical power. That is because such reactions do not necessarily reach thermodynamic equilibrium.

2.3 SOC single cell test station #2 – reversible operation

Another part of the experimental campaign included in this work was conducted using a dedicated test station designed for the characterization of a single solid oxide cell (SOC) with an active area of 16 cm^2.

2.3.1 Test bench design and characteristics

An exploded view of the setup is presented in Figure 16. The cell is positioned centrally within a ceramic housing (90 x 90 x 65 mm) specifically engineered to withstand temperatures up to 900 °C, imposed by a temperature-controlled furnace, and to accommodate a maximum gas flow rate of 2 L/min. A picture of the complete test bench and the housing assembly is shown in Figure 17.

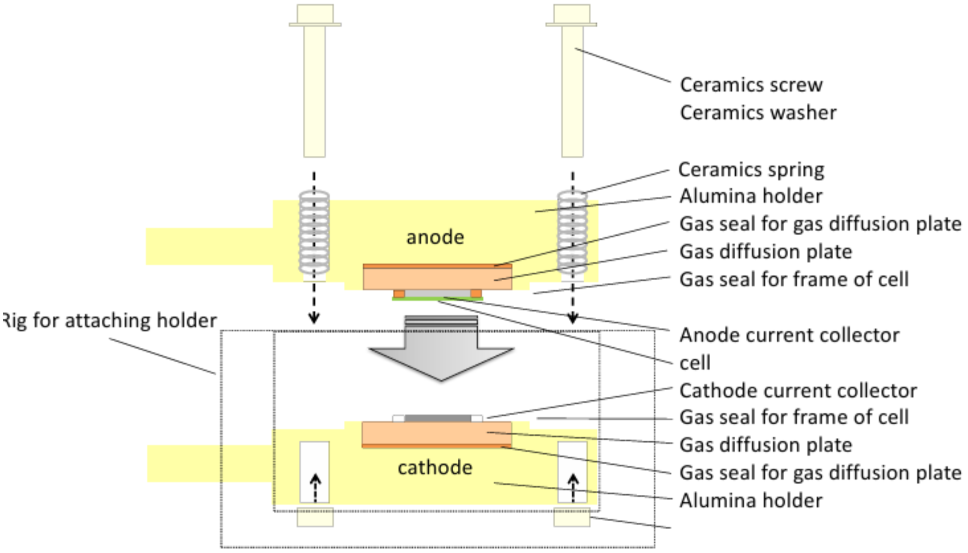

Figure 16. *Exploded view of the 16 cm^2 test setup*

Gas is supplied to and discharged from the cell through 1/4'' - diameter stainless-steel tubes, while the gas distribution plates – also fabricated from high-temperature ceramic – ensure uniform radial distribution of the flow across the cell surface, as illustrated in Figure 17c.

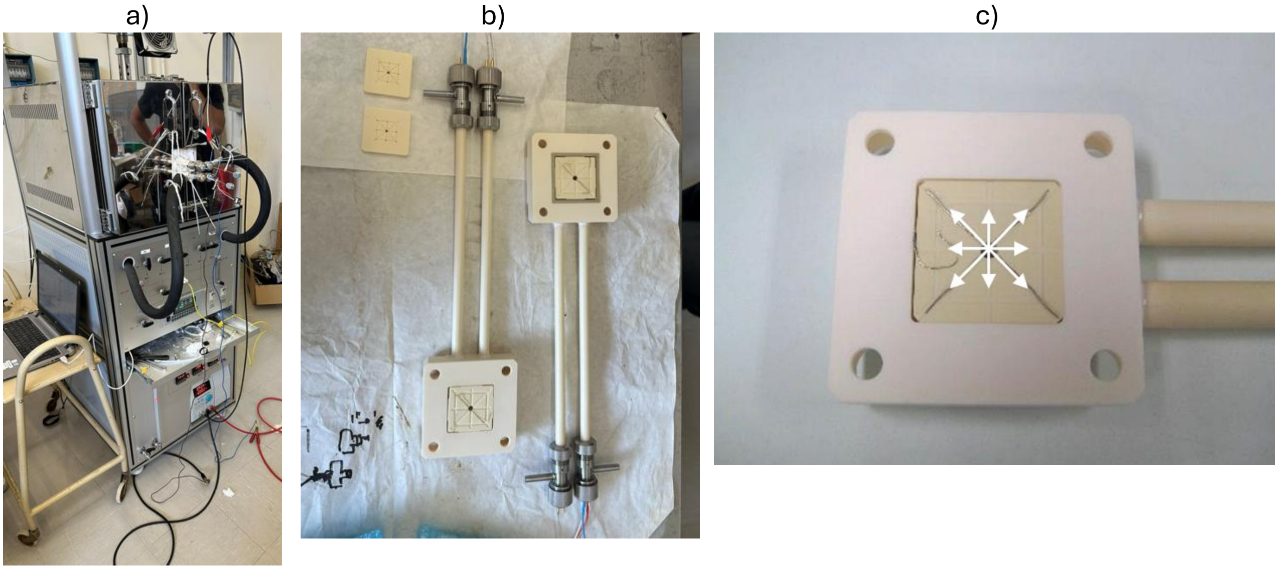

***Figure 17**. a) single cell station for reversible operation; b) cell housing; c) detail on gas flow distribution pattern*

The current collectors are made of nickel on the fuel-electrode side and silver on the air-electrode side, each with dimensions of 50 x 50 mm. Gas sealing is achieved using ceramic gaskets, while mechanical stability and electrical insulation are ensured by a high-temperature, torque-controlled fastening system composed of ceramic screws and spring-based compression elements. This design minimizes thermal stress during operation while maintaining structural integrity and consistent contact pressure.

The setup is further equipped with a BioLogic BP-300 electrochemical analyzer for electrochemical impedance spectroscopy (EIS) and a bi-directional electronic load (ITECH IT-M3903C-150-50PV), which enables operation of the cell either in fuel cell (SOFC) or electrolysis (SOEC) mode. The device allows the imposition or supply of electrical power up to 150 V and ±50 A, ensuring full control of the applied current or voltage during operation.

Overall, the complete system enables real-time assessment of electrochemical performance, gas flow behavior, and degradation mechanisms under well-controlled thermal and electrical conditions, ensuring reproducible and reliable testing of SOC single-cell behavior.

2.3.2 Concept and description of domestic load – rSOC – PV coupling

The present experimental setup has been used for a technology coupling analysis, as the system proposed now consists of the coupling of 5 main elements: household energy load, PV plant, rSOC system, hydrogen storage tank, hydrogen compressor. From now on, conventionally, positive power values will correspond to SOEC operation, and negative values to SOFC operation.

Figure 18 presents a qualitative schematic of the proposed rSOC-based renewable microgrid. The system operates according to the following strategy: the photovoltaic (PV) plant supplies power to the household load and, whenever excess electricity is available, it is used to drive the rSOC stack in electrolysis mode, thereby producing and storing green hydrogen. This operating condition occurs exclusively during daytime, as solar irradiance is required to sustain the process. Conversely, when PV generation is insufficient to satisfy the household demand – during nighttime or periods of low solar radiation – the previously stored hydrogen is utilized to fuel the rSOC stack operating in fuel cell mode, thus providing the required supplementary power.

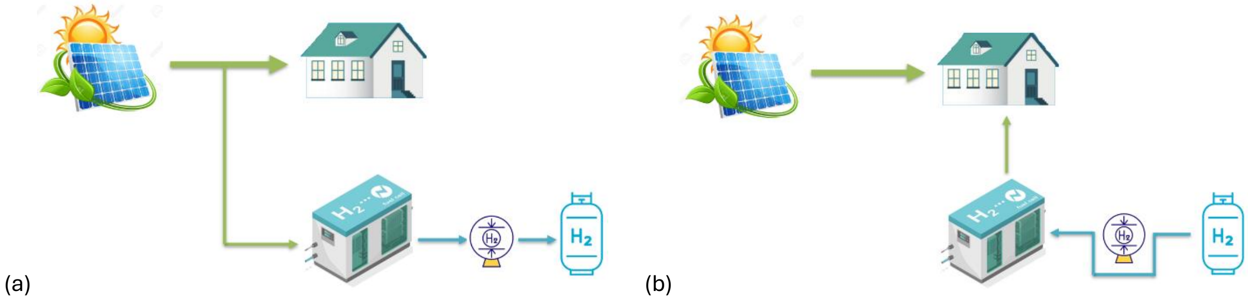

Figure 18. rSOC – energy system schematic diagram; (a) day-time operation; (b) night-time operation

This configuration has been chosen for two main reasons: first off, it represents a viable solution to fully decarbonize even dwellings that cannot be connected to the grid. Moreover, the household electricity demand has been taken as an example in this study, given the possibility to simulate its trend and retrieve data more smoothly, even though it could be potentially replaced by an industrial end user while maintaining the exact same methodology and sizing approach. At industrial level, this is of great interest as it allows to satisfy the energy needs of a large consumer through a 100% renewable – based microgrid without heavily burdening on the national grid. In this sense, to obtain generalizable results, the focus of this work has been kept on a single-family house.

Although the reference case study is based on a household located in Rome, the proposed methodology is thus fully generalizable to other locations and user types. By replacing the local renewable generation and demand profiles, the same modeling and experimental approach can be applied elsewhere. The obtained results on the rSOC responsiveness, stability, and degradation therefore will hold for comparable renewable-based energy systems in different geographical contexts.

2.3.3 Household load

The household's demand was modelled using the software LoadProfileGenerator [190], [191] to simulate the daily use and power consumption of standard domestic loads with an hourly resolution. The database contains information on household appliances commonly used in every dwelling (e.g. lights in every room, fridge and several kitchenware, TVs, computers, washing machine, etc.). It is possible to choose the energy intensity of the appliances among three sets: energy saving, energy intensive and randomly chosen devices. The former have been assumed in this work.

Information from statistical data are employed by the simulation programme to generate load curves representative of a generic household. In the following case study, a 4-people house (family with two children) is considered.

Space heating and cooling are assumed to be provided by an electric heat pump and are therefore considered as part of the electrical load. The thermal demand is estimated based on the geographic location of the dwelling (Rome, Italy) and the corresponding air temperature profile. The temperature data are simulated using the PVGIS software, following the criterion of the Typical Meteorological Year (TMY). The TMY approach relies on historical meteorological datasets spanning the past 20 years, with hourly resolution, to generate a representative annual temperature profile composed of 8760 hourly values. For each month, the year whose temperature trend most closely matches the long-term monthly average is selected, resulting in a synthetic year composed of the most representative months from the two-decade dataset. Figure 19 shows the simulated load power curve throughout the entire year. According to the model, the peak consumption of a 4-people house located in Rome is 5.55 kW and occurs on March 23rd at 5 p.m. and the power of 3 kW is exceeded only in 177 occasions, corresponding to the 2% of the year. Most of the time, the daily peak is reached between 2 p.m. and 6 p.m.

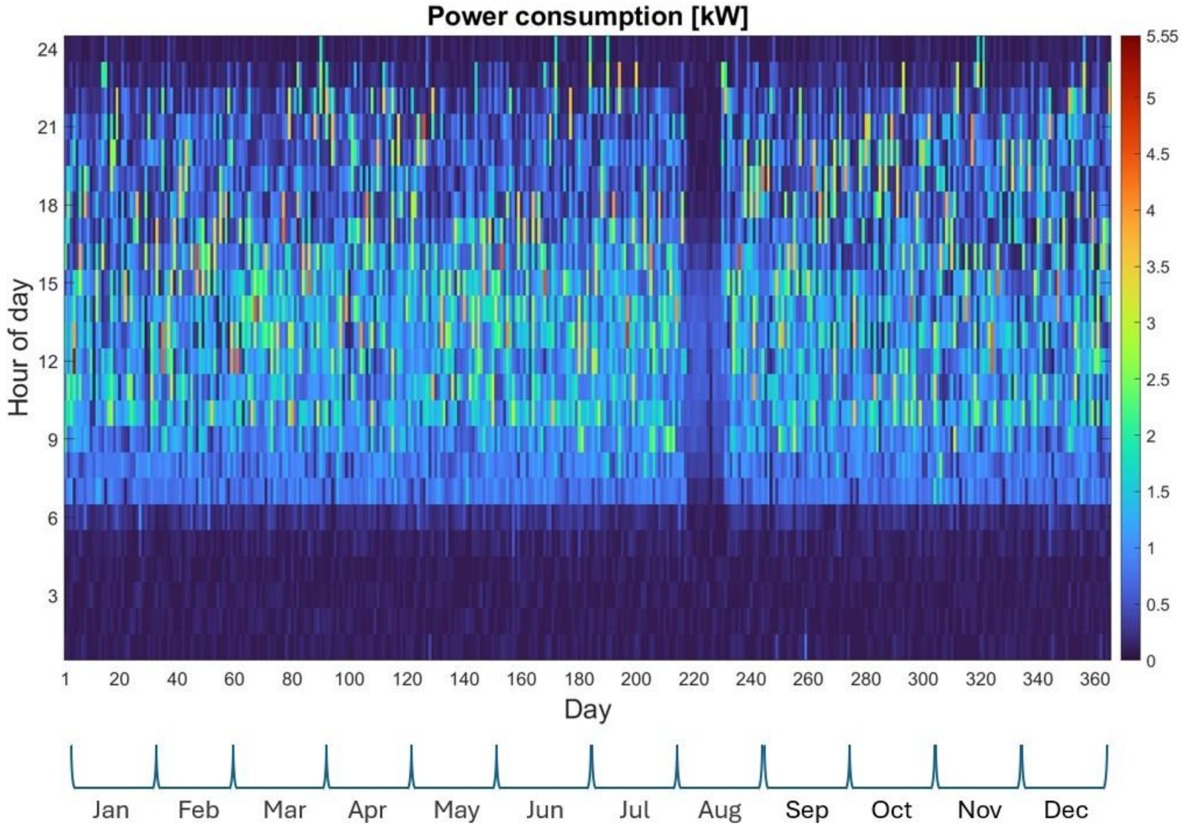

***Figure 19**:* Household's simulated power consumption as a function of hour and day of the year

2.3.4 PV system

The system object of study promotes the introduction of distributed renewable power plants by softening their impact on the grid. Among the RES, for the present case study, in spite of the high intermittency of the solar irradiance, a photovoltaic plant was adopted for two reasons: (i) the focus of the present work is to investigate on the ability of the rSOC technology to cope with highly intermittent input and output power variations; (ii) wind was put aside for the scope of this work. Some estimations made by IRENA report that the global weighted average levelized cost of electricity (LCOE) of onshore wind fell to 0.033 €/kWh in 2023, with respect to 0.044 €/kWh for PV [192]. The latest retrievable data on LCOE in Italy is as of 2020 and it is given by IEA, reporting 52.87 €/MWh for onshore wind and 58.09 €/MWh for PV, making it the cheaper technology on paper [193]. However, a dedicated wind farm does not appear to be suitable for residential applications, hence it was opted to consider a PV plant, still a valid option even in the case of industrial end user.

Combined with the rSOC-based system, the PV plant will serve primarily the residential load, and then, in case, the SOEC operation for hydrogen production.

The productivity of the PV plant depends on the specifications of the panels, their mounting position and the installing location. As mentioned earlier, Rome was chosen as a reference location, and the production from such PV plant has been simulated with the software PVGIS [194]. A reference 1 kWp-sized plant is considered, as at this stage the ideal size of the plant is unknown and will be performed afterwards.

The assumptions were made automatically by the tool, in order to optimize the performance:

- PV technology: crystalline silicon;
- Panels slope = 35°;
- Absent shadowing elements;
- Installed peak PV power = 1 kW.

Figure 20 illustrates the PV plant production curve over the course of the year. It can be seen that the maximum power simulated by the software is 870 W, produced on March 5th at at 12 p.m. The peak production is always observed between 11 a.m. and 1 p.m.

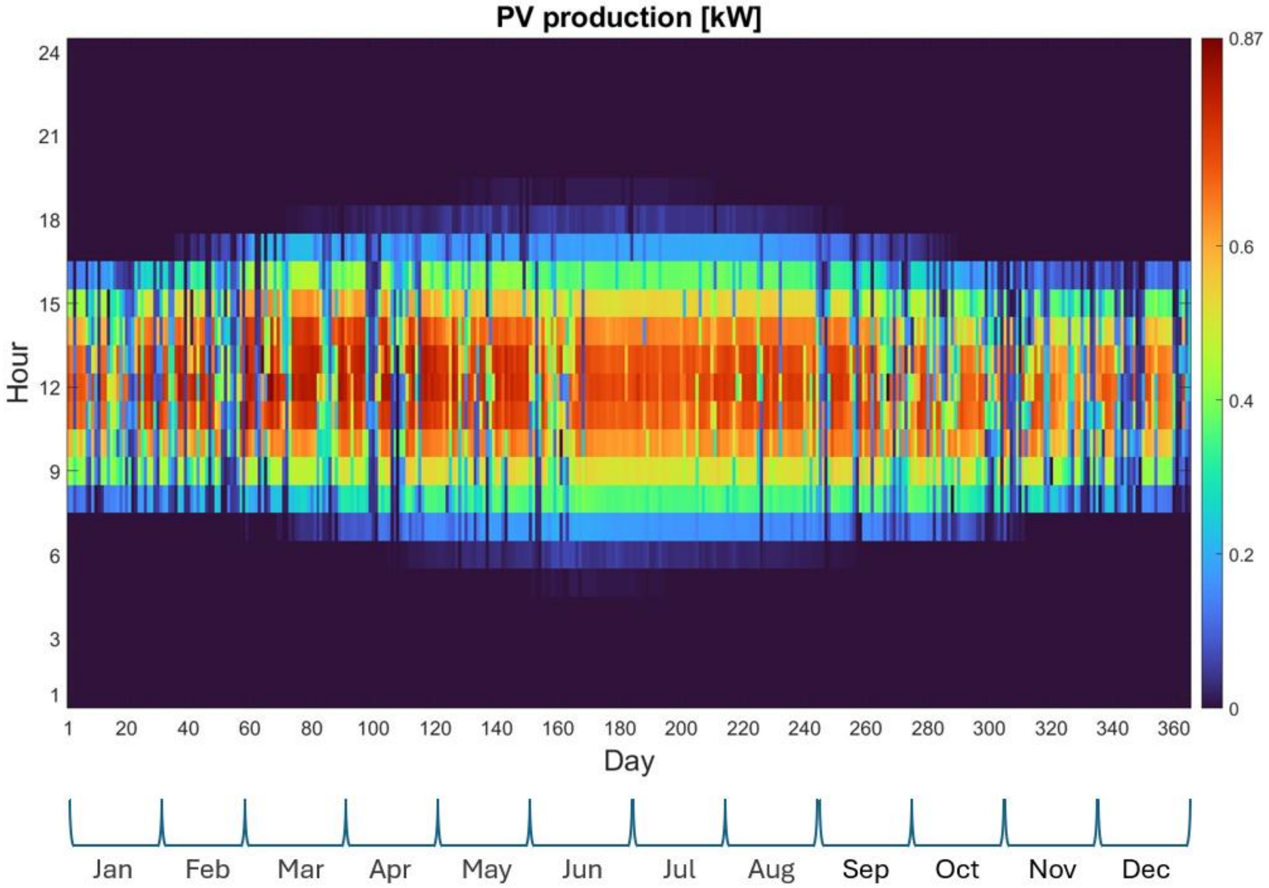

***Figure 20**:* 1 kWp PV plant simulated production as a function of hour and day of the year

2.3.5 Approach for PV and H_2 storage tank sizing

The simplified rSOC Balance of Plant (BOP) considered in this work consists only in a compressor for the storage of hydrogen. For the sizing of the rSOC stack, PV plant and H_2 tank, the literature analysis on the former suggested, as precautionary values, a water conversion efficiency rate (η_{SOEC}) of 70% [107], [195] and a hydrogen conversion efficiency rate (η_{SOFC}) of 50% [196].

The compressor can be considered as a load in case of hydrogen production and an absent element in SOFC mode, with a stored hydrogen pressure of 700 bar [197]. DOE addressed the theoretical range of energy requirements to compress hydrogen up to 700 bar: 1.7 to 6.4 kWh/kg H_2, hence a precautionary value of 5 kWh/kg H_2 has been considered in this work [198].

$$Load_{TOT} = Load_{house} + Load_{compr} \tag{77}$$

$$P_{NET} = P_{PV} - Load_{TOT} \tag{78}$$

$LOAD_{TOT}$ [kW] is the total load given by the sum of the dwelling's load ($LOAD_{HOUSE}$ [kW]) and the power absorbed by the compressor ($LOAD_{COMPR}$ [kW]), as shown in 777, and the net power supplied to the rSOC stack (P_{NET} [kW]) is calculated as the difference between the PV production (P_{PV} [kW]) and total load (Eq. 78). Positive and negative values of P_{NET} are indicative of SOEC working mode (excess of PV power) and SOFC mode respectively.

Hydrogen production and consumption are calculated by means of water and hydrogen efficiency conversions in Eq. 79 and Eq. 80:

$$H_{2_{product}} = \frac{P_{NET} \cdot \eta_{SOEC}}{LHV_{H_2}} \tag{79}$$

$$H_{2_{consumpt}} = \frac{P_{NET}}{\eta_{SOEC} \cdot LHV_{H_2}} \tag{80}$$

Where hydrogen production and consumption are expressed in kg/h and LHV_{H2} *[kWh/kg]* is the lower heating value of molecular hydrogen (33.3 kWh/kg).

The PV plant size at this stage is the only missing input information to simulate the system; it is selected iteratively until the amount of hydrogen stored at the end of the year equals the amount of hydrogen stored at the beginning of the year, in order to setup an independent and energy self-sufficient system.

The process led to an optimal PV size of 7.7 kWp, whose simulated trend of stored hydrogen is shown in Figure 21. In such case, a 37.8 kg-hydrogen storage tank is needed. Figure 21 illustrates the seasonal variation in hydrogen storage requirements, with a marked surplus during summer months and a deficit in winter, emphasizing the need to store excess hydrogen produced in summer to compensate for winter shortages. This contrast highlights the importance of appropriately sizing the hydrogen storage system to ensure year-round energy balance and uninterrupted operation. In particular, the excess hydrogen generated in summer must be adequately stored to compensate for the winter shortfall, guiding the sizing of the storage system not only in terms of capacity but also in terms of operational flexibility and discharge duration.

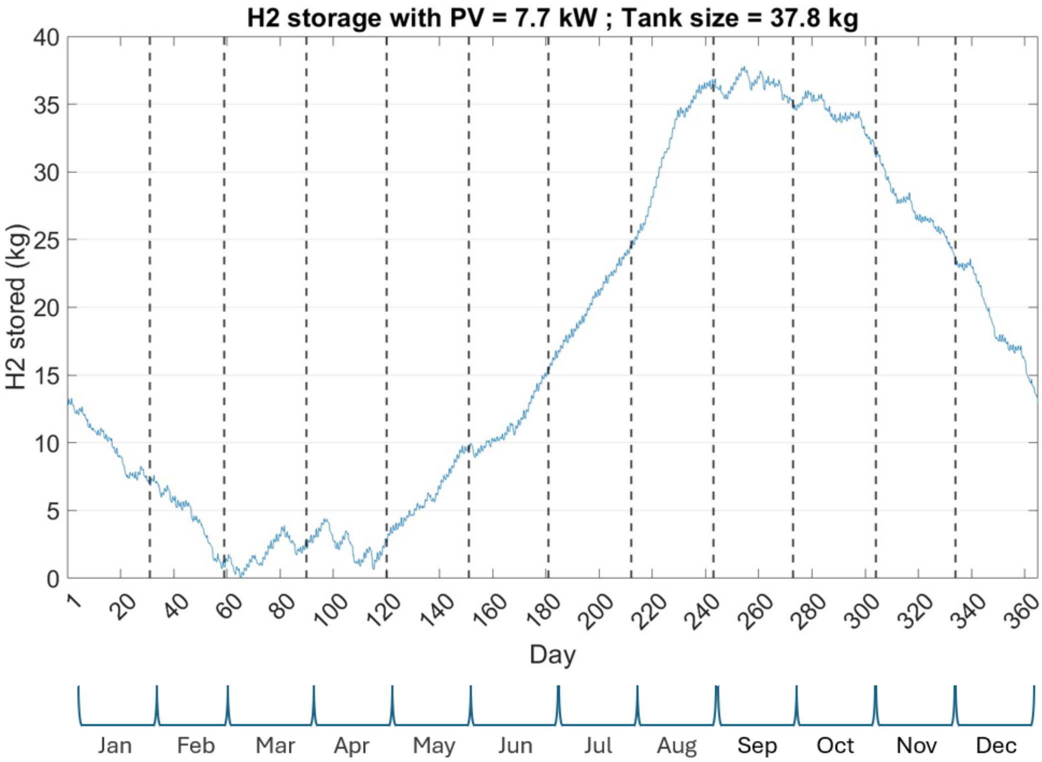

Figure 21. trend of H2 stored throughout the year; P(PV) = 7.7 kW; Tank size = 37.8 kg.

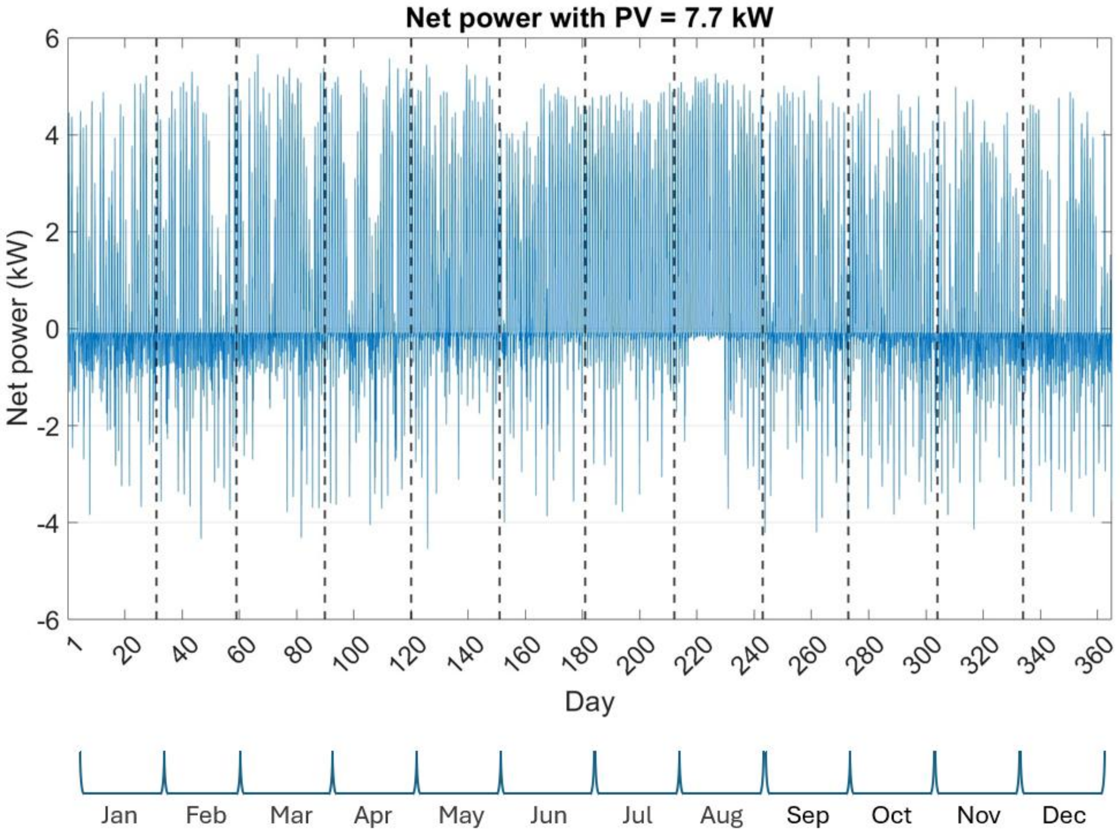

***Figure 22**:* trend of net power throughout the year; P(PV) = 7.7 kW.

The results of the simulation of the net power trend are reported in Figure 22: a maximum excess power of 5.66 kW is observed, occurred on 8th March at 11 a.m. The maximum power to be supplied to the household by means of the rSOC stack working in SOFC mode is -4.54 kW, occurred on 6th May at 8 p.m. The high loads in both SOFC and SOEC are particularly relevant from a degradation perspective, as they impose significant electrochemical stress on the cell stack. The elevated current densities and thermal gradients associated with peak operation can accelerate material fatigue and contribute to long-term performance decay.

Let us define the self-consumption ratio through Eq. 81:

$$SCR = \frac{PV_{load}}{Total\ PV} \tag{81}$$

Where PV_{load} (kWh) represents the energy produced by the photovoltaic system that is directly consumed by the household electrical load, and $Total_{PV}$ (kWh) is the total energy generated by the PV system. *SCR* (-) is therefore the self-consumption ratio, indicating the percentage of total generated energy that is effectively used to supply the load.

The data presented in Figure 22 highlight a key feature of the system under study: over the course of the year, the *SCR* amounts to 29.4%, indicating that approximately one third of the solar energy produced can be directly utilized on-site. The month with the most pronounced mismatch is August, where the *SCR* drops to 21.7%, while the highest self-consumption is observed in November, reaching 32.1%.

This mismatch between generation and consumption underscores the need for an energy storage and conversion system capable of shifting excess renewable electricity to periods of higher demand. In this context, reversible solid oxide cells represent an interesting solution to increase local self-consumption and reduce grid dependency through flexible operation in both fuel cell and electrolysis modes.

2.3.6 Preliminary economic estimation of the rSOC-based storage system

Although the present work primarily focuses on the experimental validation of rSOC system performance under realistic residential operating conditions, a qualitative economic assessment has been included to provide context for future techno-economic evaluations.

According to the Strategic Research and Innovation Agenda (SRIA) of the Clean Hydrogen Joint Undertaking [199], the benchmark capital cost (CAPEX) for reversible solid oxide cell (rSOC) systems is approximately 1250 €/kW. The cost of electricity was not included in the present analysis since it is assumed to be generated on-site by the PV plant. Consequently, the operational expenditure (OPEX) reported by SRIA, equal to 130 €/(kg H_2/day)/year, was adopted.

In the system under study, the average hydrogen production rate is 0.825 kg H_2/day. Considering an rSOC unit rated at 8.5 kW (oversized by a factor of 1.5 with respect to the maximum observed load of 5.66 kW) and approximating to 1 kg H_2/day, the estimated capital investment for the rSOC stack is about 10625 €, with an annual OPEX of approximately 130 €/year.

A similar estimation procedure was applied to the remaining components of the seasonal hydrogen energy storage system. Data for small-scale hydrogen compressors are scarce. Based on a maximum hydrogen production rate of 0.4 kg H_2/h and a specific energy consumption for compression of 5 kWh/kg H_2 (see Section 2.3.5), the corresponding compression power is 2 kW. Applying a safety factor of 1.5 yields a nominal power of 3 kW (about 4 hp). According to the cost correlations reported in [200] for compressors below 13 hp (about 9.7 kW), with an average cost of 4900 $/hp, the resulting compressor cost is approximately 19060 $ (≈ 16800 € as of October 2025).

The hydrogen tank cost was estimated using data from [201] and [202], reporting 300 $/kg H_2 and 633 $/kg H_2 respectively for Type-IV tanks at 700 bar. A mean value of 500 $/kg H_2 (about 430 €/kg H_2 in 2025) was therefore adopted. For a storage capacity of 37.8 kg H_2, rounded to 40 kg, the resulting tank cost is approximately 17200 €.

Overall, the qualitative cost analysis highlights that, for small-scale residential or microgrid applications, the compressor and hydrogen storage vessel represent the dominant contributions to expenditures, while the rSOC system plays a secondary yet non-negligible role. Although the absolute costs remain high at the present scale, future cost reductions driven by technological maturity and economies of scale are expected to significantly enhance the economic viability of integrated rSOC-based systems for seasonal storage. Based on SRIA [199] for example, the forecast at 2030 of cost reduction for key components is a decrease of more than 50%, making the system proposed suitable for future domestic applications.

2.3.7 Experimental approach and method

The objective of this study is to investigate the operation and potential performance degradation of the cell due to its reversible mode of operation. More specifically, the aim is to evaluate these parameters within the context of applying this technology to a real case study. While stack-level operation introduces additional complexities such as temperature gradients, gas flow maldistribution and pressure losses, the fundamental electrochemical phenomena can still be meaningfully investigated at single cell level. Therefore, single cell testing provides valuable insights into the intrinsic behavior and responsiveness of the technology under dynamic operating conditions. For these reasons, a single repeating unit cell of 16 cm^2 was utilized, subjected proportionally to the same load variations that a full-scale stack would experience.

This approach allows for controlled testing of degradation trends and electrochemical responses without the added complexity introduced by stack architecture and balance of plant components. Although single cells and stacks show different absolute performance [87], [88], literature shows that key degradation mechanisms – such as Nickel migration, Chromium poisoning, and interfacial instability – are consistently observed across different scales [89]. Alenazey et al [90] highlighted high operating temperature as a primary driver of performance decay, a factor equally present in both single-cell and stack environments. Thus, the single-cell configuration adopted in this study is intended to highlight general trends and dynamic responses relevant to real world rSOC systems.

To ensure consistency between the simulated and experimental conditions, the net power profiles derived from the household – PV – compressor model were proportionally scaled to match the active area of the single cell (16 cm^2), preserving the same electrical stress per unit area. This approach enables the cell to experience the same relative load variations it would encounter in a full-scale system.

The study therefore proceeded with the definition of an experimental campaign in which the daily profiles of net power (household's load + PV plant + H_2 compression) reported in Figure 22 are scaled down at single cell level, in order to replicate the same working conditions and impose the single cell the same level of stress it would have in a larger sized system. Given the troubles and complexity in replicating 365 days of testing in laboratory's facilities, a few adjustments needed to be made: both for PV and domestic load profiles, one typical day for each month has been selected, and the juxtaposition of these curves, as well as the corresponding contribution given by the compressor unit (scaled down at single cell level), gave the most representative net power profile of the said month. Consequently, each month was represented by a single typical power profile. The same procedure was applied from January through December, resulting in twelve representative power curves in total. Each profile includes both positive (SOEC mode) and negative (SOFC mode) power values. To better analyze and quantify the contribution of each operating mode to overall cell degradation, the two modes were separated: individual power profiles were defined for SOEC and SOFC operation, as described in Eq. 82 and Eq. 83. This approach effectively doubled the number of test days but did not compromise the validity of the results, since the same overall load levels were applied to the cell.

$$P_{SOEC,month\ i} = \begin{cases} P_{NET,month\ i} & if\ P_{NET,month\ i} > 0 \\ 0 & if\ P_{NET,month\ i} < 0 \end{cases} \tag{82}$$

$$P_{SOFC,month\,i} = \begin{cases} 0 & if\ P_{NET,month\,i} > 0 \\ P_{NET,month\,i} & if\ P_{NET,month\,i} < 0 \end{cases} \quad (83)$$

Where P_{SOEC} and P_{SOFC} [kW] indicate respectively the power share in electrolysis mode and fuel cell mode for the *i-th* month.

2.4 SOC stack test station

The present test station enabled the operation and characterization of a > 10 kW-scale reversible solid oxide cell system, another part of the study included in this thesis.

2.4.1 Stack test station design and characteristics

The system is about 1 m^3 in overall volume, and the placement of the main Balance of Plant (BoP) components is illustrated in Figure 23. These include: (A) the evaporator for steam generation; (B) electrical band heaters for the stack module; (C) heat exchangers for the fuel side; (D) heat exchangers for the air side; (E) catalytic afterburner; (F) outlet gas coolers.

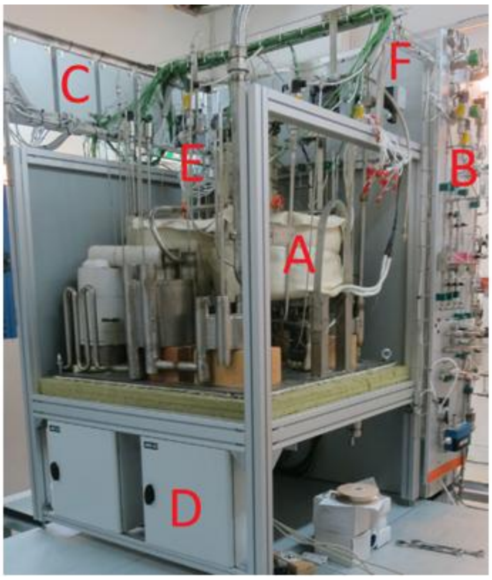

***Figure 23**. Main components of the 10 kW rSOC system [203]*

In order to minimize thermal losses and optimize the placement of the BoP components, instead of isolating each BoP component individually, the entire hot box was filled with a high-performance ceramic granular thermal insulation material [203]. This design approach enables efficient internal heat utilization while simultaneously limiting heat losses from the stack module and other BoP components to the external environment.

A simplified representation of the system P&ID (Process and Instrumentation Diagram) is shown in Figure 24. The evaporator supplies steam to the stack, and the resulting steam–gas mixture is preheated by means of a fuel heat exchanger (FHEX), where thermal exchange occurs with the fuel exiting the stack. The fuel superheater (FSH) then raises the gas temperature to its nominal operating value of approximately 700 °C.

The gas leaving the stack – now enriched in hydrogen when operating in SOEC mode – after passing through the FHEX, is directed to another heat exchanger, the Fuel Cooler Heat Exchanger (FCHEX). In this unit, heat is transferred to a coolant loop consisting of a water–glycol mixture, before the gas stream is finally sent to the compressor for storage.

An identical flow path is implemented on the air side, though through separate piping. Each corresponding component is denoted with the prefix *Air-*, resulting in AHEX, ASH, and ACHEX, respectively. The coolant is circulated by a dedicated pump, which drives the liquid through the FCHEX and ACHEX and subsequently to a radiator, where it exchanges heat with the surrounding environment and is cooled before recirculation.

It is immediately evident that the effectiveness of the cooling system partially depends on the ambient air temperature: the lower the external temperature, the colder the coolant entering the ACHEX and FCHEX, and the greater its capacity to remove heat from the fuel and air streams exiting the system.

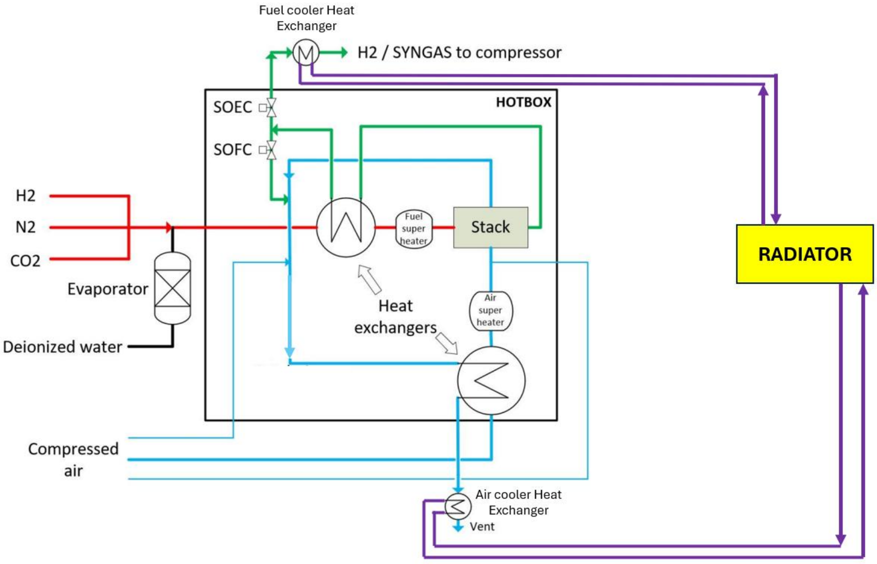

***Figure 24**. Basic P&ID of the 10 kW rSOC system*

The stack module is a commercial fuel-electrode supported type, comprising 120 cells stacked in series each with an active area of 120 cm^2.

The power electronics are installed below the hot box to facilitate compact integration and ease of maintenance. The gas supply control wall is located on the right-hand side of the system, while the programmable logic controller (PLC) and electrical cabinets for power supply and relays are positioned respectively behind and to the left of the hot box. In the event of a power failure, an uninterruptible power supply (UPS) ensures continued operation of the control logic and the most critical gas valves, thereby maintaining operational safety [203].

Additionally, the rSOC system features more than 250 individual measurement and control variables, including mass flow controllers, gas valves, bidirectional electronic load, humidity sensors, pressure sensors, thermocouples and individual cell voltage monitoring points.

System operation and monitoring are managed through a custom-developed automation system based on a PLC architecture, which ensures high precision, safety, and flexibility. The extensive data acquisition network allows for detailed thermodynamic and electrochemical analysis of the system, including real-time computation of enthalpy flows and efficiency for individual BoP components. Digitalization of all control and measurement signals is implemented via the Modbus RTU/TCP protocol, providing reliability, accuracy, and noise resistance compared to conventional analog signal processing [203]. Overall, the fully integrated and instrumented rSOC test platform enables reproducible and high-fidelity experimental investigations of reversible solid oxide systems under realistic thermal, electrical, and fluid-dynamic conditions, thereby offering valuable insight into system-level efficiency, degradation mechanisms, and dynamic response behavior.

2.4.2 SOC 10 kW-stack testing approach

The system described above was tested under various operating modes, employing different inlet gas compositions and current densities. For the purposes of this doctoral work, the discussion is focused exclusively on the SOEC operating mode, conducted at a current density of 0.5 A/cm^2 and a steam conversion rate of 66.7%.
The detailed experimental characterization of the stack is intentionally omitted here, for the reasons outlined in Chapter 1.4. Moreover, such details are not central to the discussion of the results that this section aims to highlight.
The portion of the experimental campaign considered in this study extended over a total duration of 336 hours, during which all relevant parameters – including temperatures and pressures at multiple locations, as well as the electrical consumption of individual components – were continuously monitored and recorded in real time.

The performance analysis of the system is carried out by examining the enthalpy flows of the gases at various points of the plant and by calculating efficiencies, defined in several different ways. The enthalpy flow is defined according to the formulas reported in Eq. 84 and 85:

$$\dot{H}_{i,j} = \dot{m}_{i,j} \cdot cp_{i,j} \cdot \Delta T_{i,j} \tag{84}$$

$$\dot{H}_{j,tot} = \sum_i \dot{H}_{i,j} \tag{85}$$

Where *i* denotes the gas species present in the mixture, *j* refers to a specific location within the plant, $\dot{H}_{i,j}$ (kW) is the enthalpy flow of gas *i*, $\dot{m}_{i,j}$ (kg / s) is the mass flow rate of gas *i* at point *j*, $cp_{\,i,j}$ (kJ / kg K) is the specific heat capacity of gas *i* and ΔT_i (K) is the difference between the mixture temperature at point *j* and the reference temperature, set in this case study at 293 K. The specific heat capacity of each gas was determined, using appropriate correlations, as a function of its temperature. The total enthalpy flow at each point *j* was calculated as the sum of the contributions of each gas in the mixture.

The plant sections under investigation are the following:

- Fuel side: evaporator OUT, FHEX cold IN, FSH IN, FSH OUT, stack IN, stack OUT, FHEX hot IN, FHEX hot OUT, FCHEX OUT;

- Air side: AHEX cold IN, ASH IN, ASH OUT, stack IN, stack OUT, AHEX hot IN, AHEX hot OUT, ACHEX OUT.

This type of analysis is essential to understand how thermal energy is transferred, transformed, or lost within the plant, in order to identify the main losses and to diagnose potential faults.
The following formulations are used to calculate the system efficiencies:

$$\eta_{stack} = \frac{\dot{m}_{H2\,prod} \cdot LHV_{H2}}{P_{stack}} \tag{86}$$

$$\eta_{system} = \frac{\dot{m}_{H2\,prod} \cdot LHV_{H2} + \dot{H}_{fuel,OUT} + \dot{H}_{air,OUT}}{P_{stack} + P_{evap} + P_{FSH} + P_{ASH} + P_{aux}} \tag{87}$$

$$\eta_{system,RAD} = \frac{\dot{m}_{H2\,prod} \cdot LHV_{H2} + P_{rad} + \dot{H}_{fuel,OUT} + \dot{H}_{air,OUT}}{P_{stack} + P_{evap} + P_{FSH} + P_{ASH} + P_{aux}} \tag{88}$$

$$\eta_{system,RAD+EVAP} = \frac{\dot{m}_{H2\,prod} \cdot LHV_{H2} + P_{rad} + \dot{H}_{fuel,OUT} + \dot{H}_{air,OUT}}{P_{stack} + P_{FSH} + P_{ASH} + P_{aux}} \tag{89}$$

Where η_{stack} (-) is the stack efficiency, η_{system} (-) is the system efficiency, $\eta_{system,RAD}$ (-) is the system efficiency taking into account the heat recovery at the radiator and $\eta_{system,RAD+EVAP}$ (-) is the system efficiency taking into account the heat recovery at the radiator and the hypothesis of free steam available.
In the present study, the radiator functions as the component responsible for cooling the coolant stream exiting the ACHEX and FCHEX. Consequently, the heat transferred from the coolant to the surrounding environment is considered a thermal loss. However, in a real-scale system, if the SOC plant were to be integrated into a district heating network, this portion of thermal energy could be effectively recovered and utilized. In that case, it would represent an additional energy gain for the overall system. Therefore, Eq. 88 expresses the system efficiency under the assumption that such recoverable heat is fully exploited.
Eq. 89 instead describes the efficiency in a scenario where also free steam is available, as may occur in certain industrial facilities. Under these conditions, the heat required for steam generation does not constitute an energy expenditure, thereby leading to an improvement in the overall system efficiency.

The terms appearing in the equations are as follows: $\dot{m}_{H2\,prod}$ (kg/h) is the hydrogen production rate, P_{stack} (kW) is the electrical power consumed by the stack, P_{evap} (kW) is the electrical power consumed by the evaporator, LHV_{H2} (kWh/kg) is the lower heating value of hydrogen, P_{FSH} and P_{ASH} (kW) are the electrical consumption of the FSH, ASH, P_{aux} is the electrical consumption of other auxiliary systems (e.g., mass flow controllers, control electronics, computers, etc.), P_{rad} (kW) is the power recovered through the radiator.

2.5 Electrochemical performance characterization and gas analysis

In this section, the main characterization techniques employed for solid oxide cells (SOCs) are presented and described, namely polarization (I-V) curves and electrochemical impedance spectroscopy (EIS). In addition, the section provides a description of gas chromatography, which is utilized to determine the gas composition during in-operando operation of the cell.

2.5.1 Polarization curve

The polarization curve (or i-V curve) is the most widely used diagnostic technique for evaluating the overall performance of a solid oxide cell [31]. A representative polarization curve for solid oxide cells (SOCs), in both fuel cell and electrolysis operation modes, is illustrated in Figure 3.

This curve is obtained by measuring the cell voltage as a function of the applied current density – either extracted from the cell in SOFC mode or supplied to the cell in SOEC mode. It provides a direct visualization of how the different electrochemical, transport, and kinetic phenomena combine to determine the overall performance of the device. As such, polarization analysis represents one of the most fundamental and informative characterization techniques for SOCs, allowing the evaluation of cell behavior under varying operating conditions and over a wide range of current densities.

The Open Circuit Voltage (OCV), corresponding to the voltage measured at zero current density ($i = 0$ A/cm^2), reflects the thermodynamic potential difference between the electrodes. When compared with the theoretical voltage calculated through the Nernst equation (Eq. 12), it offers critical information about potential gas leakage or cross-diffusion phenomena that may reduce the effective separation between the reactant gases. A lower experimental OCV than the theoretical value is typically indicative of such parasitic effects or of partial mixing between the anodic and cathodic gas streams.

At low current densities, the initial voltage deviation is mainly attributed to activation polarization losses, which originate from the energy barrier that must be overcome for the electrochemical reactions to proceed at the electrode interfaces. These losses depend on factors such as the electrode microstructure, catalytic activity and temperature, and therefore provide insight into the reaction kinetics of the cell.

In the intermediate current density region, the voltage typically exhibits a linear trend with respect to current density. This portion of the curve corresponds to ohmic polarization, which arises from resistive losses within the electrolyte, electrodes, and interconnects. Among these contributions, the electrolyte resistance is usually dominant. The slope of this linear region enables the determination of the Area Specific Resistance (ASR), expressed in $\Omega \cdot cm^2$. The ASR is often used to compare the electrical performance of cells fabricated with different materials or architectures. The linearity of this segment also indicates that the internal resistance remains nearly constant within this operating regime, in agreement with Ohm’s law.

At high current densities, the voltage experiences a pronounced deviation due to concentration polarization, also referred to as mass-transport or diffusion losses. This regime arises when the rate of reactant supply (fuel or steam) becomes insufficient to sustain the required current, leading to reactant starvation. Such behavior may result from gas diffusion constraints within the porous electrode structure or from inadequate flow distribution. This condition is related to a shortage of fuel (in SOFC) or steam (in SOEC) at the reactive interface. This region defines the maximum usable current density of the cell, beyond which severe performance degradation and irreversible material damage can occur.

It is important to note that not all polarization curves necessarily exhibit the same characteristic shape as that shown in Figure 3. In general, the activation loss region and the ohmic region are almost always clearly visible, as they represent intrinsic electrochemical and resistive behaviors of the cell. Conversely, the concentration polarization region is often intentionally avoided during testing, since operating the cell under strong mass-transport limitations can accelerate degradation phenomena. In practice, this is achieved either by supplying an adequate amount of fuel or steam to the inlet – thus preventing reactant starvation even at relatively high current densities – or simply by limiting the operational current range so that the threshold of the concentration losses is never reached.

2.5.2 Electrochemical Impedance Spectroscopy (EIS)

Electrochemical impedance spectroscopy (EIS) is another widely adopted diagnostic techniques for investigating the electrochemical behavior in solid oxide cells [204], [205], [206] . It enables non-destructive analysis of the processes occurring within the cell, allowing for the separation of resistive and capacitive contributions that govern the overall performance of the system. The fundamental principle of EIS consists in applying a small alternating voltage or current perturbation across a range of frequencies to a cell maintained under steady-state operating conditions in terms of temperature and gas composition. The resulting current or voltage response is then analyzed in the frequency domain to extract the complex impedance $Z(\omega)$ [Ω cm^2], defined as in Eq. 90:

$$Z(\omega) = \frac{V(\omega)}{I(\omega)} = Z'(\omega) + jZ''(\omega) \tag{90}$$

where $Z'(\omega)$ [Ω cm^2] denotes the real part of the impedance, associated with resistive losses, while $Z''(\omega)$ [Ω cm^2] represents the imaginary part, related to capacitive accumulation phenomena [207]. The measurement results are typically displayed in a Nyquist plot, in which $-Z''(\omega)$ is plotted as a function of Z'. A representative Nyquist diagram obtained from impedance analysis on SOCs is shown in Figure 25.

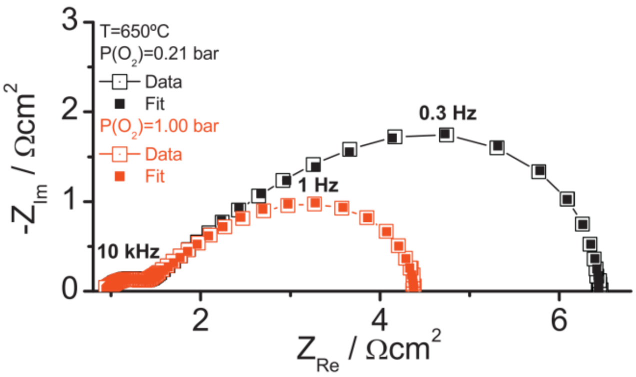

Figure 25. *Typical EIS spectra in SOC cells; in this particular case, two SOFC conditions are studied.*

This representation enables visual distinction of the various processes occurring within the cell. In a typical EIS spectrum of a solid oxide cell (SOC), one or more semicircles are observed, each corresponding to a phenomenon characterized by its own time constant. The high-frequency intercept on the real axis corresponds to the total ohmic resistance R_{ohm} [Ω cm^2], which is primarily determined by the resistance of the electrolyte and the electrical contacts. The semicircles appearing at intermediate and low frequencies reflect contributions associated with charge transfer processes, ionic and electronic diffusion within the electrodes, and surface reactions involving adsorption/desorption of reactants [31]. The polarization resistance (R_{pol} [Ω cm^2]) can be defined as the difference between the low-frequency and high-frequency intercepts, and is indicative of the combined losses due to activation and concentration overpotentials:

$$R_{pol} = R_{tot} - R_{ohm} \tag{91}$$

The total cell resistance R_{tot} , measured at low frequencies, reflects the sum of all losses affecting the cell, including activation, ohmic, and concentration-related contributions. Electrochemical impedance spectroscopy is employed both in the fundamental study of the materials constituting the cell (electrolyte, anode, and cathode) and in the in-operando monitoring of cells and stacks, providing valuable insights into degradation mechanisms. However, EIS does not reveal which electrode predominantly contributes to the polarization resistance. For a more detailed analysis of the individual phenomena occurring at each electrode, it is necessary to employ the Distribution of Relaxation Times (DRT) method.

2.5.3 Gas chromatography

Gas Chromatography (GC) is an analytical technique aimed at determining the composition of gaseous mixtures. The method is based on the different distribution of substances between a stationary phase (solid or liquid supported on a solid) and a mobile phase (carrier gas), according to the specific affinity of each compound for the stationary phase.

A schematic overview of a typical gas chromatograph is shown in Figure 26, which illustrates the essential components of the system and the analytical process.

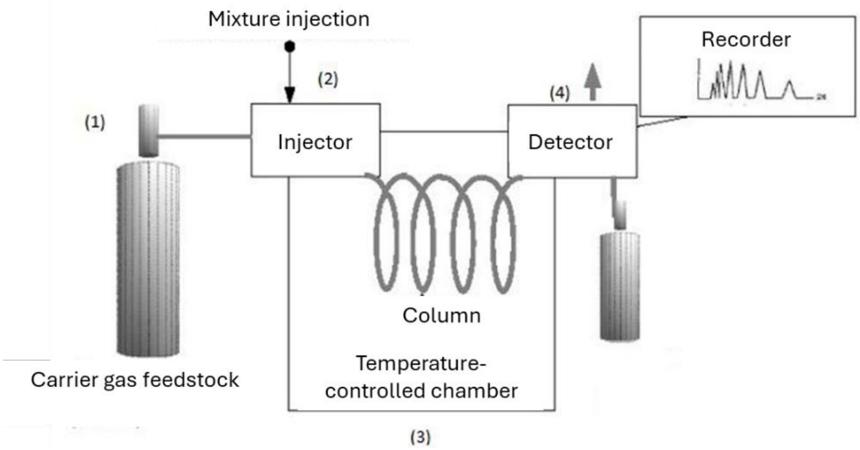

***Figure 26**. Scheme of the essential components of a Gas Chromatograph.*

Carrier gas supply system

The carrier gas – typically an inert gas such as nitrogen, helium, or argon, and in some cases hydrogen – is used to transport the sample gaseous components through the chromatographic column. The choice of carrier gas depends on the detector type and the desired analytical sensitivity.

Injector or injection chamber

The injector's main function is to ensure the instantaneous vaporization of the sample. This step is particularly critical when using capillary columns, for which only a very small amount of sample (in the order of microliters) can be introduced. To achieve optimal sample transfer, various injection techniques have been developed, which allow only a controlled fraction of the injected sample (typically about 1/100) to enter the column. The injection chamber is equipped with a variable-resistance heating system that allows precise temperature control, ensuring complete and reproducible vaporization of the mixture.

Column

The chromatographic column can be either packed or capillary. The packed columns (2 – 4 mm internal diameter, 1 – 4 m length) are used in classical gas chromatography. They consist of steel or glass tubes filled with an inert solid support coated with a thin layer of stationary liquid phase. The sample is carried through the column by the flowing carrier gas. Separation efficiency is limited by the relatively slow elution of molecules along the packed bed. Capillary columns (0.1 – 0.8 mm internal diameter, 10 – 100 m length), now widely used, represent a major advancement due to their faster elution and higher resolution – typically achieving more than four times the number of resolved peaks in half the time compared to packed columns. Their smaller diameter and thinner stationary phase require much smaller sample volumes.

Columns are located in a temperature-controlled furnace, usually with forced hot-air circulation to ensure thermal stability. The furnace temperature can be held constant throughout the analysis (isothermal operation) or varied according to a temperature-programmed profile to improve the separation of compounds with different volatilities.

Detector

Detectors can be classified as universal or selective. Universal detectors are capable of detecting any compound present in the sample, whereas selective detectors respond only to specific classes of compounds. For the analyses conducted in this work, a Thermal Conductivity Detector (TCD) was employed. The TCD consists of four metallic filaments connected in a Wheatstone bridge configuration. Helium is the most commonly used carrier gas due to its high thermal conductivity, which is greater than that of most analytes. The Wheatstone bridge is balanced when the product of resistances across opposite arms is equal. Under these conditions, when only the pure carrier gas passes through the detector, no voltage difference is measured, and the bridge is said to be "balanced."

When an analyte elutes from the column and enters the detector, the thermal conductivity of the carrier gas mixture decreases. Consequently, less heat is removed from the filaments, causing an increase in their temperature and electrical resistance. This change unbalances the bridge, generating a measurable electrical signal proportional to the analyte concentration.

The TCD is a universal and non-destructive detector, suitable for virtually any compound. Its sensitivity typically reaches ≤ 0.01 %, making it an effective and reliable tool for continuous monitoring of gas composition in solid oxide cell experiments.

3. RESULTS AND DISCUSSION

This chapter presents and critically discusses the results obtained from the experimental and modeling activities described in Chapter 2, following the methodologies and operating conditions therein detailed. The experimental outcomes are organized and interpreted with the explicit aim of addressing the research questions and scientific issues introduced in the previous chapters, through a multi-level analysis encompassing different system scales and complementary investigation approaches.

Particular emphasis is placed on the interpretation of the results with focus on the underlying physical and electrochemical phenomena, as well as on their implications for the design, operation and scale-up of solid oxide technology. Through this structured and multi-scale analysis, the chapter seeks to provide coherent and comprehensive answers to the identified research questions, highlighting both the advances achieved and the remaining limitations that motivate further investigation.

3.1 Research Question 1: How can localized experimental characterization of SOCs be improved beyond conventional techniques to optimize electrochemical performance?

The first step towards the development of solid oxide cell (SOC) technology in electrolysis mode lies in a detailed understanding of the phenomena occurring at the local scale, in order to identify strategies for improving and optimizing its operation. To enable an analysis capable of achieving this objective, it is necessary to employ an experimental system that allows for an in-depth investigation of the water vapor conversion mechanisms in a spatially resolved manner across the entire cell active area. The multisampling system described in Section 2.1 was specifically designed to enable this type of investigation.

3.1.1 Experimental gas composition distribution

Following the approach described in Section 2.1, in Figure 27 the experimental H_2 and H_2O concentration plots across the fuel-electrode surface are reported, along with their respective H_2O concentration contour plots, for the three conditions tested. Given the measurement uncertainty of the GC, error bars of ± 3 vol% are shown, as indicated in Section 2.1.

In condition 1 (H_2O/H_2 = 50/50, FF = 300 mL/min), the H_2O concentration drops steeply from 50% at the inlet to about 10% at the outlet. The contour plot reveals a strong gradient concentrated in the first half of the cell, particularly between sampling points 1-2-3 and 4. This indicates that the majority of the electrochemical activity is localized near the inlet, where the steam concentration is highest. The distribution on the axis perpendicular to the direction of the flow also shows some slight asymmetry, suggesting non-uniform gas distribution across the width of the cell.

In condition 2 (H_2O/H_2 = 50/50, FF = 500 mL/min), the H_2O profile is more gradual, ranging from 50% to about 25%, as this condition mitigates the formation of steep gradients.

In condition 3 (H_2O/H_2 = 70/30, FF = 500 mL/min), the inlet steam concentration is higher (70%), and the outlet still retains significant H_2O (about 40%). The conversion is less pronounced, as expected under constant current operation with excess steam.

These results confirm that steam conversion is not uniform across the cell surface, and that the inlet region consistently exhibits the highest electrochemical activity. The extent and distribution of the gradients are strongly influenced by the inlet flow rate and composition: since the same amount of water needs be converted (electrical load remains unaltered), the outlet H_2O concentration varies depending on the inlet water content. In terms of gas composition, lower flow rates and lower steam content lead to sharper gradients, while higher flow rates and excess steam promote more uniform operation.

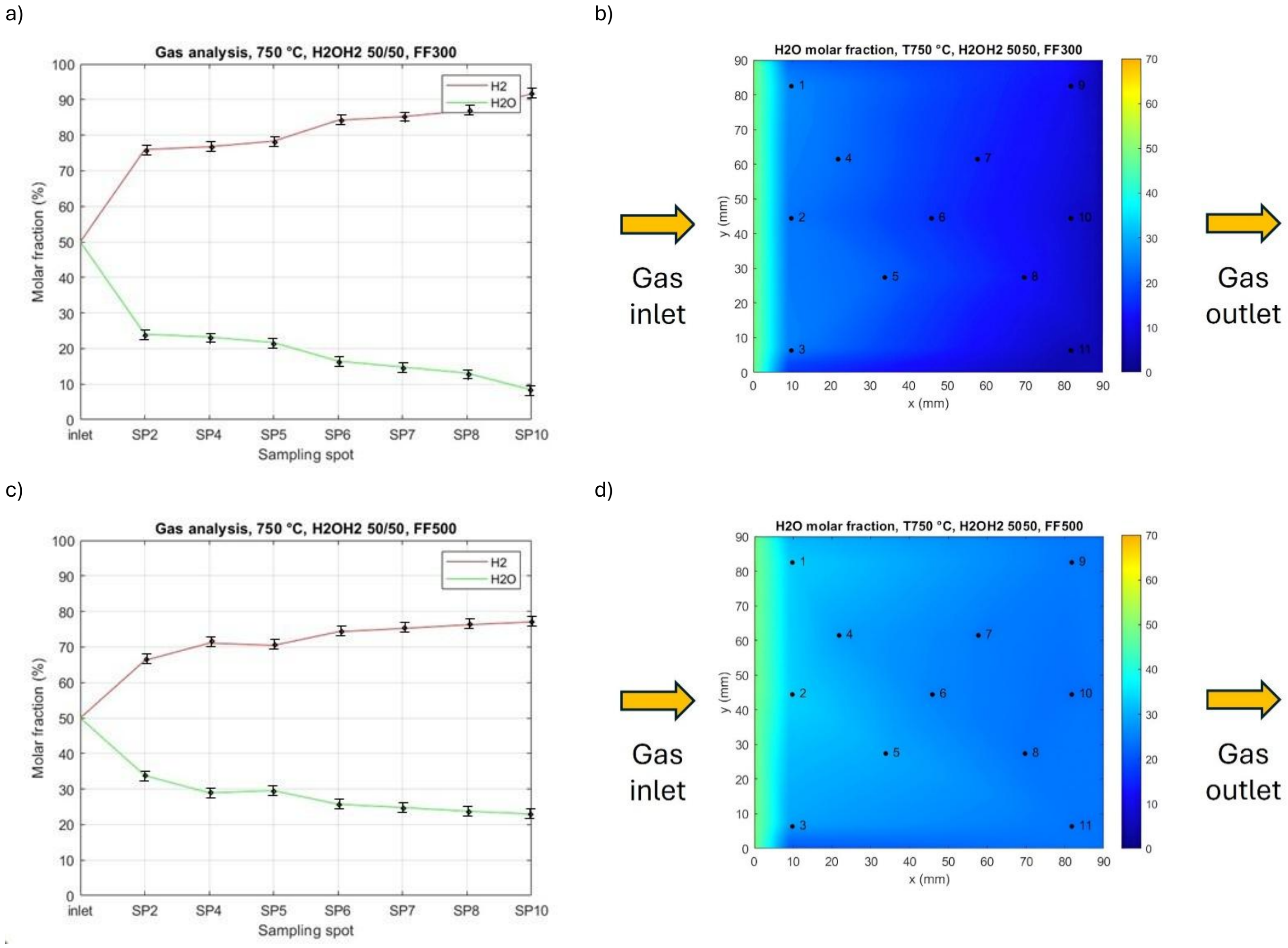

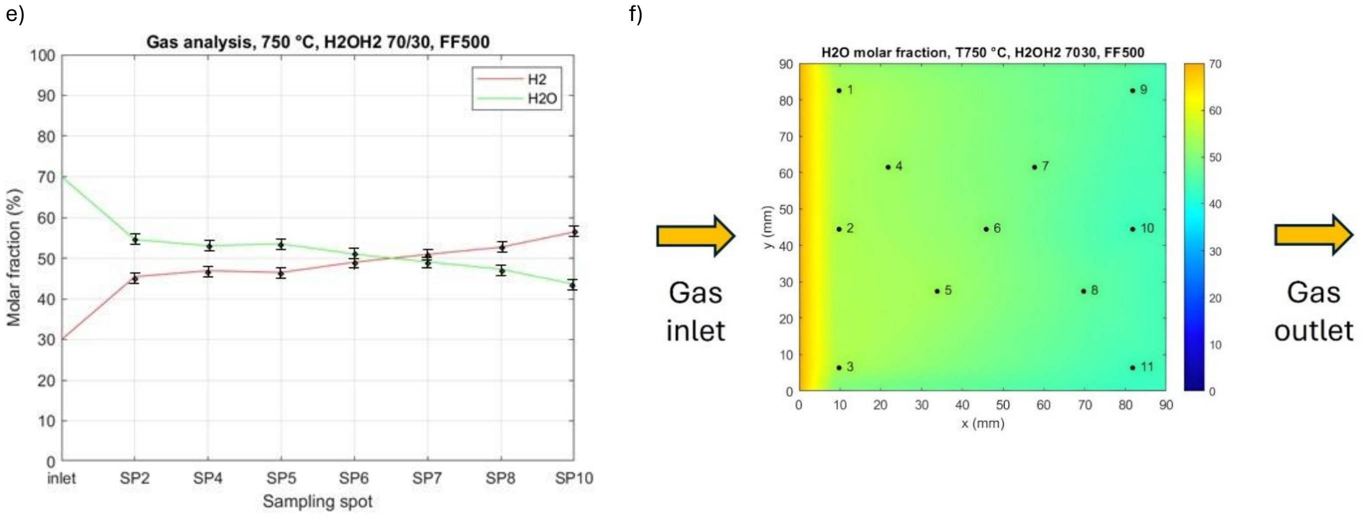

Figure 27: H_2 and H_2O concentration plots; as in Table V: a) condition no.1; c) condition no.2; e) condition no.3;
H_2O contour plots: b) condition no.1; d) condition no.2; f) condition no.2

In order to show the correlation between experimental and theoretical results, a Faradaic balance on the hydrogen produced has been performed (Eq. 92):

$$H_{2\,produced,Faradaic} = \frac{I}{2 \cdot F} \cdot 22.414 \cdot 60 \cdot 1000 \tag{92}$$

Where $H_{2\,produced,Faradaic}$ (ml/min) is the theoretical production of H_2 through the electrochemical conversion of water, *I* (A) is the current, 22.414 (Nl/mol) are the normal liters of any gas contained in a mole, 60 (s/min) and 1000 (ml/min) are conversion factors. Added to the inlet H_2 content, the overall H_2 content at the outlet can be determined. At experimental level, the percentage of H_2 at the outlet allows the calculation of the effective outlet H_2 content ($H_{2\,produced,exp}$), and thus the discrepancy between the two values, as in Eq. 93:

$$e = \frac{H_{2\,produced,Faradaic} - H_{2\,produced,exp}}{H_{2\,produced,Faradaic}} \cdot 100 \tag{93}$$

For the cases 1, 2 and 3 respectively (as in Table V), *e* resulted to be 4.35%, 3.02% and 4.34%, proving the limited discrepancy between theoretical calculations and experimental outcomes.

3.1.2 Local cell voltage and current distribution

The results from the experimental GC analyses shown in section 3.1.1 are now utilized to determine the distribution of current density and voltage, as described in section 2.1.

Table XI: modelling results for local voltage and current density; as in Table V, condition no.1

Sampling point	Voltage (V)	Current density (A/cm^2)	Local steam conversion (%)
1	1.202 ± 0.01	0.411 ± 0.012	22.1
2	1.213 ± 0.01	0.441 ± 0.013	23.7
3	1.206 ± 0.01	0.423 ± 0.013	22.8
4	1.123 ± 0.01	0.137 ± 0.004	9.6
5	1.147 ± 0.01	0.172 ± 0.005	13.2
6	1.193 ± 0.01	0.254 ± 0.008	22.5
7	1.156 ± 0.01	0.116 ± 0.003	13.3
8	1.201 ± 0.01	0.187 ± 0.006	24.8
9	1.227 ± 0.01	0.184 ± 0.006	32.4
10	1.241 ± 0.01	0.208 ± 0.006	36.6
11	1.238 ± 0.01	0.202 ± 0.006	35.5

Table XII: modelling results for local voltage, current density and steam conversion; as in Table V, condition no.2

Sampling point	Voltage (V)	Current density (A/cm^2)	Local steam conversion (%)
1	1.153 ± 0.01	0.451 ± 0.014	14.5
2	1.151 ± 0.01	0.437 ± 0.013	14.1
3	1.159 ± 0.01	0.461 ± 0.014	14.9
4	1.106 ± 0.01	0.259 ± 0.008	9.8
5	1.085 ± 0.01	0.171 ± 0.005	7.1
6	1.103 ± 0.01	0.206 ± 0.006	9.3
7	1.089 ± 0.01	0.144 ± 0.004	7.2
8	1.089 ± 0.01	0.129 ± 0.004	6.9
9	1.099 ± 0.01	0.143 ± 0.004	8.2
10	1.100 ± 0.01	0.146 ± 0.004	8.4
11	1.096 ± 0.01	0.133 ± 0.004	7.7

Table XIII: modelling results for local voltage, current density and steam conversion; as in Table V, condition no.3

Sampling point	Voltage (V)	Current density (A/cm^2)	Local steam conversion (%)
1	1.093 ± 0.01	0.422 ± 0.013	9.7
2	1.098 ± 0.01	0.438 ± 0.013	10.1
3	1.095 ± 0.01	0.429 ± 0.013	9.9
4	1.026 ± 0.01	0.170 ± 0.005	4.4
5	1.009 ± 0.01	0.102 ± 0.003	2.7
6	1.039 ± 0.01	0.186 ± 0.006	5.1
7	1.050 ± 0.01	0.201 ± 0.006	5.8
8	1.053 ± 0.01	0.191 ± 0.008	5.9
9	1.071 ± 0.01	0.214 ± 0.006	7.0
10	1.071 ± 0.01	0.215 ± 0.006	7.0
11	1.065 ± 0.01	0.198 ± 0.006	6.5

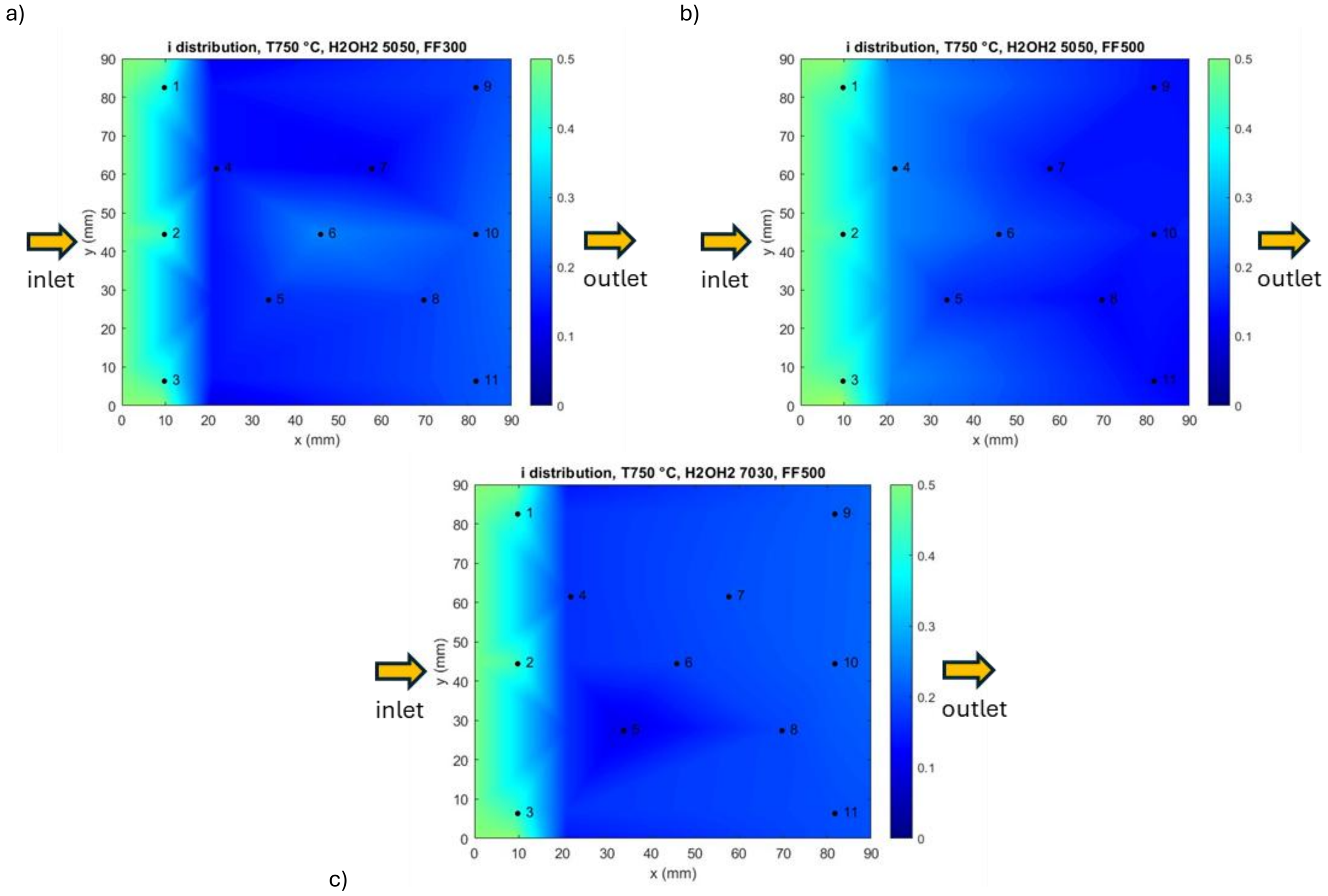

Figure 28: contour plot of modelling results for local current density; as in Table V, a) condition no.1; b) condition no.2; c) condition no.3;

In agreement with the gas analysis discussed in Section 3.1.1, the models for calculating the local current density (Figure 28) and voltage also clearly show higher cell activity in the region near the gas inlet section. The calculations highlight a cell voltage above 1.150 V for the areas corresponding to sampling points 1, 2, and 3 for all conditions studied except for condition no.3 (Table XI, Table XII and Table XIII).

In condition no.2, all subsequent points (4 to 11) exhibit a rather uniform voltage, ranging between 1.085 V and 1.100 V, unlike the case with FF = 300 mL/min, where the highest voltage values are observed in the sections near the outlet. This phenomenon is mainly attributed to the low water content in those same sections – a condition that also occurs in all other cases but to a much lesser extent, such that with FF = 500 mL/min, the phenomenon is not even observed.

The current density is consistent with the voltage profile, highlighting different behaviors between different regions of the cell: values between 0.4 and 0.45 A/cm^2 at points 1, 2, and 3 (about twice as much as the overall cell current density of 0.235 A/cm^2), and below 0.260 A/cm^2 at the remaining points. Since the current density is an indicator of the electrochemical activity of the cell, it can be stated that the area represented by points 1, 2, and 3 – exhibiting values up to 2 times higher than those of the subsequent regions – is the most active and, consequently, also the most prone to degradation. As also shown in the literature concerning the testing of solid oxide cells [88], [92], [93], [95], [96], [97], [98] nominal current density values exceeding 0.5 A/cm^2 are rarely reached, if not for accelerated stress tests, and this operating point is therefore considered a threshold that should not be exceeded in order to avoid highly accelerated cell degradation phenomena.

Similar dynamics to those observed with varying inlet flow rate are found when changing the composition of the inlet gas. At equal sampling points, the comparison with tests conducted at lower inlet water content reveals lower average voltage values, resulting from the higher water concentration at each location. This effect is particularly pronounced in the region near the outlet: the voltages at sampling points 9, 10, and 11 are slightly lower than those at the inlet. In contrast, in the test with H_2/H_2O = 50/50 and FF = 300 mL/min, these outlet voltages are slightly higher – despite the lower electrochemical activity – due to the reduced amount of gas (e.g. water) available for conversion.

Similarly to the Faradaic balance, area-weighted local current densities have been compared to the applied global current density to validate internal consistency. By multiplying each local current density (as in Tables VI, VII and VIII) by the corresponding area to which that value is associated, and summing the resulting products, total current values of 18.2 A, 18.3 A, and 18.2 A are obtained for case studies 1, 2, and 3, respectively. These values deviate by approximately 4% from the 19 A actually applied to the cell. It is worth noting that this deviation is nearly identical to that observed for the hydrogen flow rate at the cell outlet, when comparing theoretical and experimental calculations.

In Tables VI, VII, and VIII, error propagation for current density and voltage was considered, based on the measurement uncertainty of the GC from which these modeled quantities are derived. The current density was found to have an error directly proportional to the electrochemical activity, since it is proportionally linked to the GC measurement: the ± 3 % error on the GC translates into a ±3 % error on the current density. Therefore, the modeled values of current density can be considered only minimally affected by measurement uncertainties.

Similar considerations can be made regarding the estimated error on voltage. Unlike current density, voltage does not have a direct proportional relationship with experimental measurements and is influenced by multiple sources of error, making its evaluation more complex. The contributing factors include the GC measurement error, temperature measurement uncertainty, and potential uncertainties in model input parameters. Given the large number of variables involved, we focused on the contributions from the GC, temperature, and one key model input parameter—activation energy, assumed with a ±10 % uncertainty – to assess model stability.
Consequently, the error was calculated for each component of the voltage shown in Eq. 1, resulting in an overall estimated uncertainty of approximately ± 10 mV for all cases. This uncertainty is largely dominated by the activation energy, which accounts for nearly 50 % of the total error. The estimated voltage uncertainty is considered applicable uniformly across all sampling points.

Since in this study the 0.5 A/cm^2 threshold has not been reached, as suggested by the modeling analysis, it is reasonable not to expect a dramatic degradation of cell performance over the medium to long term. Among the consequences of operating at high current density, numerous studies report the occurrence of Ni migration or Ni re-oxidation – particularly when a high concentration of water vapor is combined with high current density or voltage, leading to fuel-electrode-induced cell degradation in the long term; by contrast, the impact on the air-electrode side is negligible [72], [73], [208], [209].

The nickel re-oxidation reaction is the following [210]:

$$Ni + H_2O \leftrightarrow NiO + H_2 \tag{94}$$

The high water concentration gradient between the inlet area (points 1, 2, and 3) and the immediately subsequent region (point 4), as shown in Figure 27, leads to a strong imbalance in NiO concentration, with NiO being more concentrated near points 1, 2, and 3 in order to re-establish equilibrium in the reaction (Eq. 94). This oxide, migrating towards regions of lower concentration (point 4), will further shift the reaction toward the products, accelerating the consumption of Ni and H_2O in the inlet section, ultimately causing a decrease of active sites for the inlet gas.

This phenomenon, on one hand, highlights the degradation mechanism that develops in regions of higher electrochemical activity, and on the other hand explains the greater water consumption observed at the cell surface near the gas inlet. However, despite this observed inlet bias effect is consistent with possible degradation mechanisms, further microstructural characterization would be needed to confirm this.

Other degradation mechanisms of the cell have been observed and reported in numerous studies. Among these, Ni coarsening is one of the most extensively investigated [72], [74]. This process involves an increase in the size and a decrease in the number of nickel particles, resulting in a loss of interparticle contact and, consequently, an increase in polarization resistance. Hubert et al [211] reported a significant occurrence of Ni coarsening in post-mortem analyses following a series of long-term experiments (ranging from 1000 h to 9000 h), leading to a substantial loss of active sites. The phenomenon was particularly pronounced at higher operating temperatures.

Ni migration has also emerged as a frequent degradation pathway, with several studies [72], [212], [213] confirming its occurrence and detrimental impact on cell performance, especially when associated with a coarser Ni microstructure [214].

The current density gradient across different areas of the cell is a phenomenon also reported in the literature: Yildiz et al [107] developed a model that shows a decrease from the gas inlet region (about 0.55 A/cm^2) to the outlet region (about 0.38 A/cm^2); similarly, Xu et al [108] performed a numerical investigation highlighting the same trend (approximately 0.49 A/cm^2 at the inlet and 0.14 A/cm^2 at the outlet), considering an average applied current density of 0.4 A/cm^2. In both examples, however, unlike in the present study, the decrease in current density along the flow direction is nearly linear.

One reason why the imbalance observed in this work is particularly marked can be attributed to the Ni migration and Ni re-oxidation mechanisms discussed earlier, which significantly shift electrochemical activity towards the inlet region – phenomena that are not modeled in the cited references. By contrast, the present study, being supported by experimental data, is able to account for all the phenomena occurring within the system.

Although current density and voltage are closely related, a higher current density does not necessarily correspond to a higher voltage: for instance, in condition no 1, point 1 exhibits 0.411 A/cm^2 and 1.202 V, while point 11 shows 0.202 A/cm^2 and 1.238 V. This behavior can be attributed to the higher water concentration at point 1 compared to point 11, resulting in a lower voltage for the same current density.

Moreover, regions near the outlet exhibit a higher voltage than those near the inlet, for the same current density, due to concentration losses.

Local cell performance in SOFCs has been previously investigated using segmented cell and impedance-resolved approaches. Extending these approaches, this work introduces model-derived voltage maps validated by multi-sampling in electrolysis mode, representing a novel methodological contribution.

3.1.3 Local temperature distribution – FF variation

The temperature distribution is determined as described in Section 2.1.6.

The experimental temperature measurements inherently account for certain errors due to various factors, including: (i) a sub-optimal insulation of the environment surrounding the cell and a non-uniform temperature distribution caused by thermal resistances within the furnace not being precisely calibrated to the same power level; (ii) non-uniform positioning of thermocouples. To mitigate such systematic errors, a reference measurement was conducted, in which the cell was replaced, in the same test bench, with an insulating material (Thermiculite) of identical dimensions, without applying any gas flow or electrical load. Under these conditions, the recorded temperature reflects only the errors attributable to the furnace and thermocouples. The difference (ΔT) between the temperature measured during the actual experiments (which includes all effects) and that recorded in the reference test thus represents the temperature variation due to fluid dynamic and chemical/electrochemical phenomena. The sum of the nominal operating temperature (750 °C) and ΔT yields a corrected temperature value, effectively compensating for systematic errors introduced by the experimental setup. The temperature values reported in this work are those obtained following the correction.

Based on the defined approach, the calculated values are representative of all local phenomena related to cell operation (e.g., fluid dynamic, chemical and electrochemical processes), but not of boundary-related effects (e.g., cell positioning inside the furnace, non-uniform operation of the furnace's heating elements, etc.).

Table XIV: modelling results for local temperature; as in Table V, condition no.1 (FF = 300 mL/min) and condition no.2 (FF = 500 mL/min)

Sampling point	**Temperature – model / experimental [°C] @ H_2O/H_2 = 50/50, FF = 300 mL/min**	**Temperature – model / experimental [°C] @ H_2O/H_2 = 50/50, FF = 500 mL/min**	**Temperature – model / experimental [°C] @ H_2O/H_2 = 70/30, FF = 500 mL/min**
1	744.8 ± 2 / 747.6 ± 1	743.1 ± 2 / 746.6 ± 1	743.2 ± 2 / 746.4 ± 1
2	745.1 ± 2 / 749.5 ± 1	743.2 ± 2 / 748.5 ± 1	743.1 ± 2 / 748.3 ± 1
3	744.9 ± 2 / 745.9 ± 1	743.3 ± 2 / 745.3 ± 1	743.2 ± 2 / 744.9 ± 1
4	746.5 ± 2 / 751.1 ± 1	744.1 ± 2 / 749.9 ± 1	746.8 ± 2 / 749.7 ± 1
5	746.3 ± 2 / 750.4 ± 1	745.8 ± 2 / 749.4 ± 1	747.1 ± 2 / 749.0 ± 1
6	746.3 ± 2 / 751.8 ± 1	745.7 ± 2 / 750.5 ± 1	747.8 ± 2 / 750.4 ± 1
7	747.5 ± 2 / 752.4 ± 1	746.7 ± 2 / 750.9 ± 1	747.1 ± 2 / 750.8 ± 1
8	747.5 ± 2 / 750.6 ± 1	747.4 ± 2 / 749.6 ± 1	747.4 ± 2 / 749.3 ± 1
9	748.3 ± 2 / 749.8 ± 1	747.3 ± 2 / 748.5 ± 1	747.3 ± 2 / 748.4 ± 1
10	748.5 ± 2 / 733.6 ± 1	747.3 ± 2 / 732.8 ± 1	747.3 ± 2 / 732.3 ± 1
11	748.5 ± 2 / 748.4 ± 1	747.5 ± 2 / 747.7 ± 1	747.6 ± 2 / 747.2 ± 1

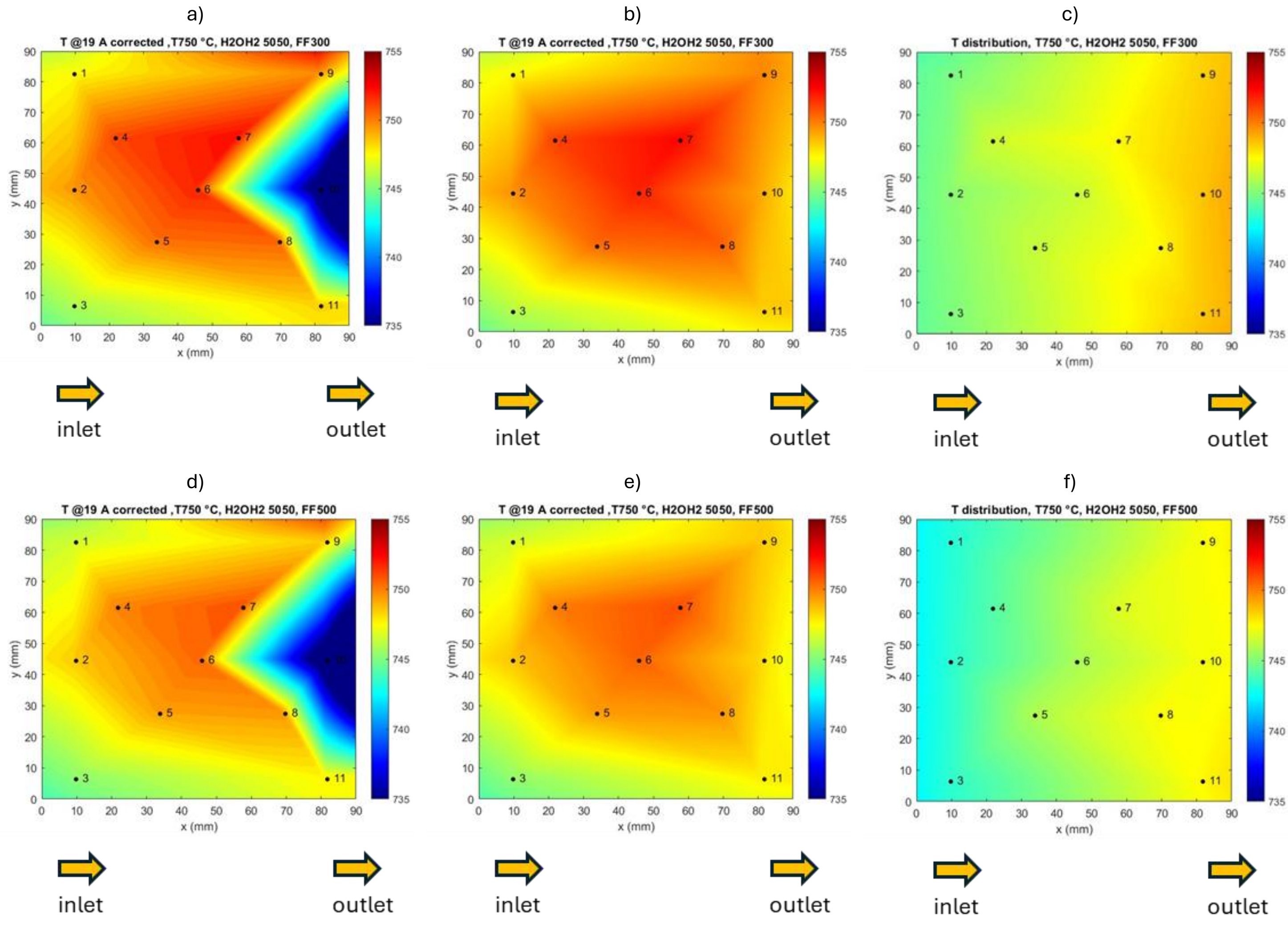

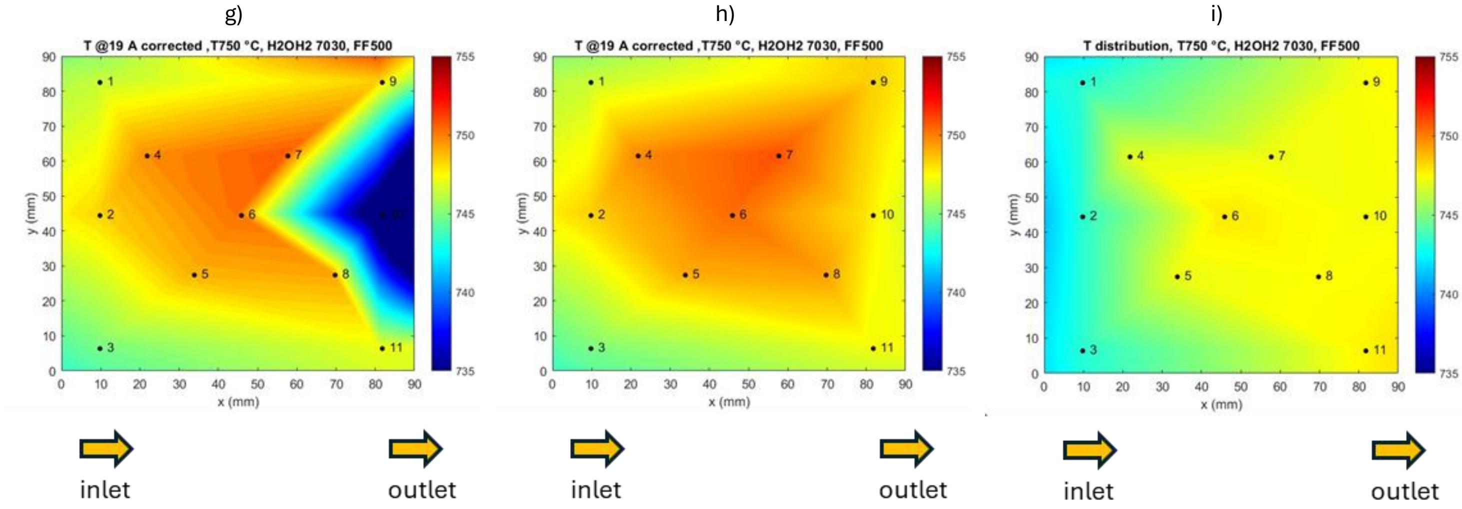

***Figure 29**:* temperature distribution contour plots; a) condition no.1, experimental; b) condition no.1, experimental excluding T10; c) condition no.1, model; d) condition no.2, experimental; e) condition no.2, experimental excluding T10; f) condition no.2, model; g) condition no.3, experimental; h) condition no.3, experimental excluding T10; i) condition no.3, model.

The results of the analysis are reported in Table XIV and Figure 29, highlighting a few key aspects: (i) the temperature in the inlet zone is the lowest across the entire cell: in agreement with the simulations of local voltage and current density (Table XI, Table XII and Table XIII), the high electrochemical activity – combined with operation in endothermic mode ($V < V_{therm}$) – leads to significant heat absorption; (ii) the central and outlet zones exhibit lower electrochemical activity, resulting in reduced heat absorption compared to the inlet sections. Consequently, the gas reaches a temperature lower than that of the surrounding system (750 °C), although it tends to approach it; (iii) experimentally, maximum temperatures slightly higher than that of the furnace are observed. This is not indicative of exothermic operation but rather of imperfect furnace control, which is not precisely centered at 750 °C; (iv) the gas temperature decreases with increasing flow rate, as a higher incoming gas flow – assuming constant cross-sectional area and gas density – results in a higher transit velocity and, therefore, shorter residence time within the furnace; (v) sampling point 10 consistently records lower temperature values compared to the surrounding zones, with differences of up to 15 °C. Given the corrections applied to the experimental data, in principle, no systematic error should be present at that point, although it appears to deviate from the overall trend observed in both the cell and the model. Future developments of this study will aim to investigate this aspect more thoroughly, in order to better understand the underlying cause of the anomaly (e.g., chemical/electrochemical reactions, fluid dynamics specific to the experimental setup, thermocouple measurement error, or other factors); (vi) if temperature point T10 is excluded from the experimental mapping, as highlighted in Figure 29, a very similar trend is observed between the model results and the experimental data – specifically, a cooler inlet zone and warmer central and outlet regions. Deviations between the model and the experimental results are limited – less than 1% - thus confirming the consistency between the two.

Error propagation analysis was also performed for temperature measurements. For the experimental data, the uncertainty is solely attributable to the tolerance of the thermocouples (± 1 °C), whereas the modeled values are affected by the tolerances assigned to the model input parameters. By assuming a conservative tolerance of ± 10 % for two key parameters in the temperature calculation (*h* and c_p), the resulting overall uncertainty on temperature is estimated at approximately ± 2 °C, which is considered applicable to all sampling points.

High thermal gradients on the cell surface are well known to be detrimental, as they are a primary cause of irreversible structural damage, such as rupture and cracking [182], [215], due to uneven thermal expansion across the cell surface. Thermal gradients within the cell have also been documented in the literature: Lim et al [216] report a smoothly increasing simulated temperature profile, with a difference between inlet and outlet of approximately 20 °C for a cell operating in exothermic electrolysis mode at $i = 0.6944$ A/cm^2 and $V = 1.418$ V. Xu et al [108] simulate an SOEC at $i = 0.4$ A/cm^2 and $V = 1.2867$ V, showing a nearly linear profile and a ΔT of about 9 °C between inlet and outlet. However, comparison is limited due to the assumption of uniform voltage and current density across the entire cell surface made by the aforementioned studies – an assumption not adopted in the present work.

To place the obtained temperature results into context, a review of the literature on thermal gradients in SOCs was conducted. Several studies suggest a structural safety limit of 5 K/cm for the cell [217], [218], while Petipas et al. report a value of 10 K/cm [83]. Chen et al. [219] further delineate thresholds by defining a safe range (< 5 K/cm), a hazardous range (5–8 K/cm), and a high-risk range (> 8 K/cm) for evaluating SOEC safety. In comparison, the gradients measured in this study (≤ 4.5 °C across the entire cell surface, corresponding to an average of 0.5 K/cm) fall well below these thresholds and can therefore be considered non-critical from this standpoint.

Moreover, a comparison between the present SOEC investigation and previous studies conducted with a similar setup in SOFC mode ([117], [118], [119]) reveals notable distinctions between the two operating modes. In SOFC mode, the electrochemical activity was more uniformly distributed along the fuel electrode surface, whereas in SOEC a pronounced activity was observed near the gas inlet, with local current densities reaching up to twice the average value. Such behavior is unique to electrolysis operation, as it induces stronger heterogeneities in gas composition and current density than those typically observed under fuel cell operation. Furthermore, the present study indicates that Ni re-oxidation and migration phenomena, likely exacerbated by steep H_2O/H_2 gradients, represent a degradation pathway specific to electrolysis. Overall, these findings demonstrate that extending the multisampling diagnostic approach to electrolysis mode not only confirms its versatility but also reveals degradation mechanisms not evident in fuel cell operation.

3.2 Research Question 2: How does fuel composition affect the performance and efficiency of SOC stacks in stationary CHP configurations, and which metrics are most appropriate for comparative evaluation? Is SOC technology suitable for current and future gas grid scenarios?

From an application-oriented perspective, one of the major potentials of solid oxide cell (SOC) technology lies in its use for stationary combined heat and power (CHP) generation. Assessing the suitability and effectiveness of this technology for such applications requires a thorough evaluation of system performance under operating conditions that are as close as possible to real-world scenarios.

To this end, the short stack described previously, together with the underlying experimental campaign design, was specifically conceived to evaluate the performance of SOC technology under representative CHP operating conditions. The experimental activities were therefore aimed at assessing the performance of the stack, as well as its operational behaviour under different fuel compositions and load conditions, in order to provide a realistic evaluation of its potential for stationary cogeneration applications.

The results in terms of polarization curves and stable power points for each gas composition scenario are collected to compare the stack performance under the different fuel feedstock scenarios. For the polarization curves (Figure 30), only the results of the tests in nominal conditions (30 A full-load, FU 70%, 660°C) are reported, for sake of brevity.

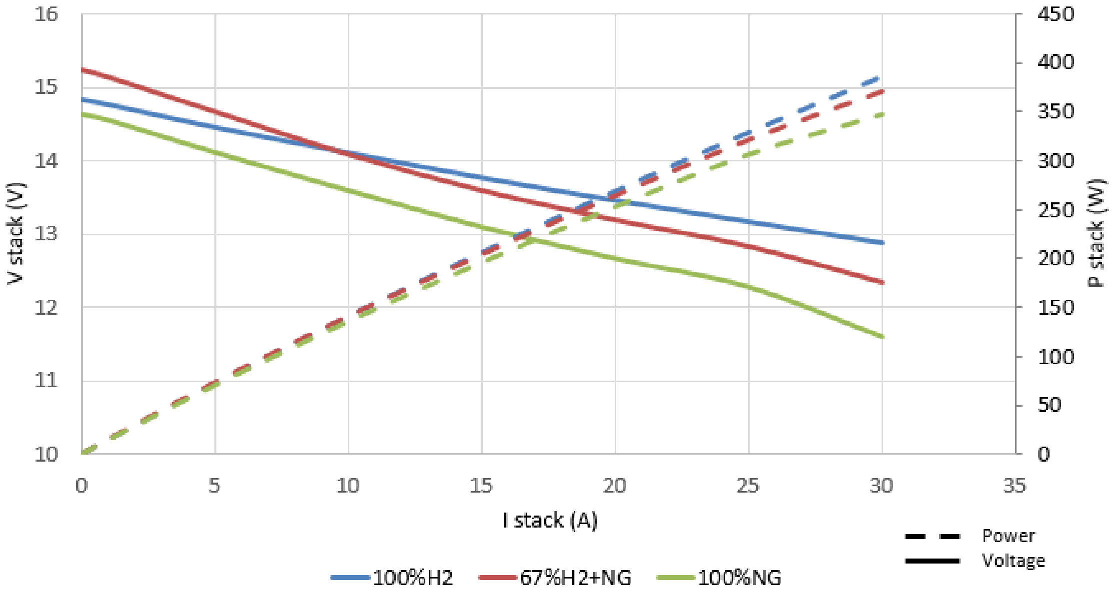

a)

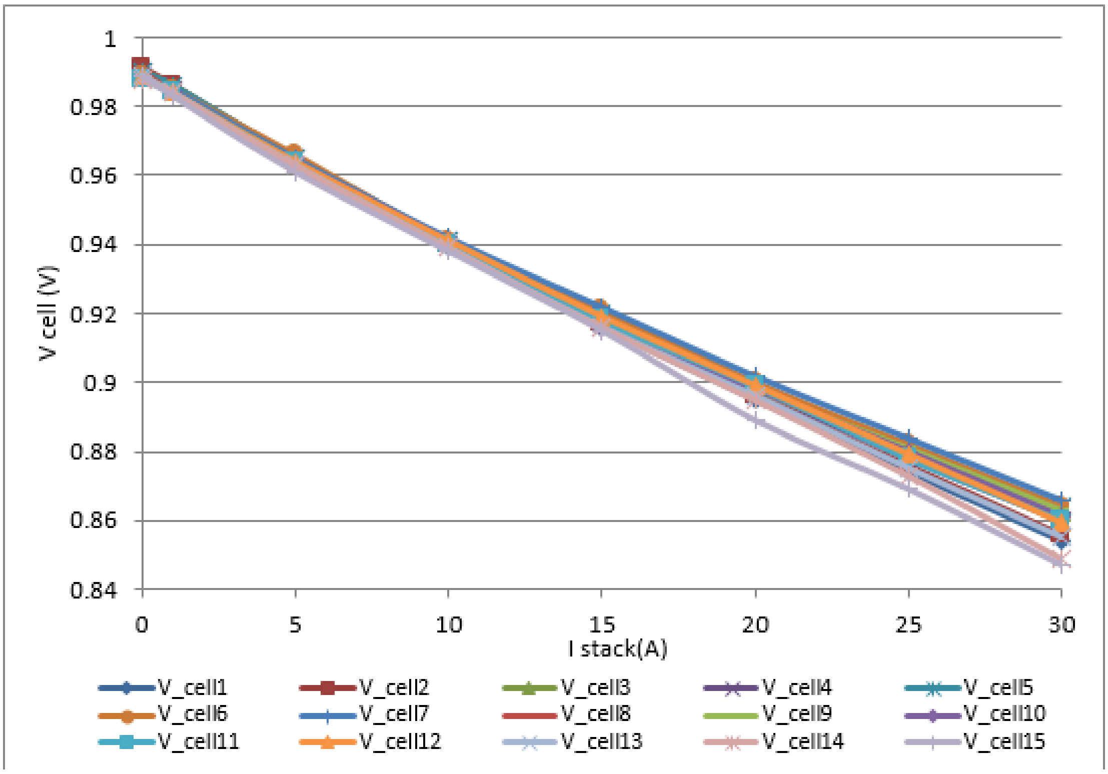

b)

***Figure 30**:* EL350 polarization and power curves in nominal conditions (30 A full load, 660°C, FU 70%) with different fuel compositions (a);

By analyzing the polarization curves, it can be observed that the 67% H_2 + NG composition obtains the highest OCV, respect to the 100% H_2 and 100% NG compositions due to higher H_2O content other than presence of other matrix gases (CO, CO_2, CH_4) in the fuel gas which reduces the Nernst voltage. Under load the slope of the polarization curve is strongly dependent on the gas composition. The 100% H_2 composition obtains the best performance with highest voltage and power (around 13 V and 390 W respectively) at the nominal current (30 A). Instead, a worse performance is obtained under load with the two reformate compositions (around 12.4 V vs. 11.7 V and 375 W vs. 350 W, respectively) with a similar slope throughout the polarization curve, maintaining the offset determined by the different OCV values (around 14.7 V vs 15.3 V respectively).

The performance maps of the short stack at different single-pass FU and temperature conditions are reported in Figure 31. The maps are based on the stable operating points for which a constant power output has been recorded during the short-term stability tests for >2 h to ensure that a stationary thermal, chemical and electro-chemical regime is reached.

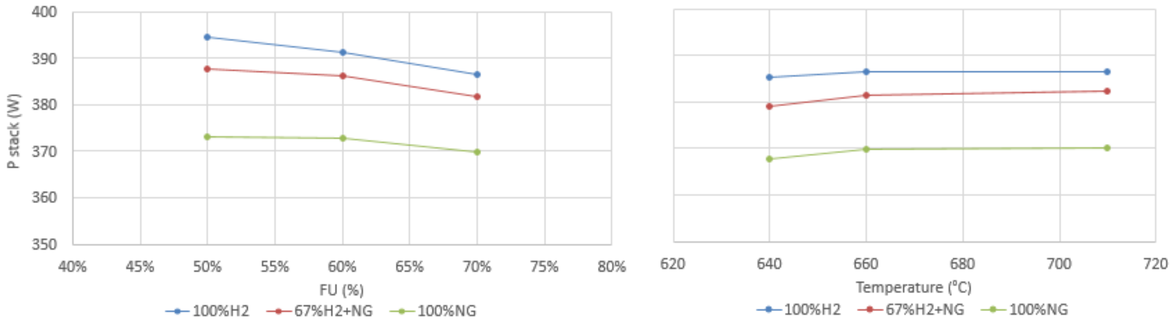

Figure 31: EL350 performance maps with different fuel compositions: (left) var FU (30 A full load, 660°C); (right) var T (30 A full load, FU 70%)

The numerical results of the performance maps (Table XV) confirm that the highest output power is obtained at lower FU (since at equal current less hydrogen is consumed, and the stack and cell voltages are higher) and at higher temperature (which benefits the thermally activated phenomena).

Table XV: Performance map in nominal conditions with different fuel compositions.

Stable operation points - P stack (W) @ 30 A	**100%H2**	**67%H2+NG**	**100%NG**
FU 50%	394.50	387.60	373.20
FU 60%	391.20	386.10	372.90
FU 70%	386.40	381.60	369.90
[640°C - 710°C]	[385.20-386.43]	[379.20-382.50]	[367.80-370.20]

The efficiency trend is repartitioned differently between the gases compositions according to the formulation considered for its calculation. The following tables (Tables IV - IX) report the efficiency results, divided into inlet fuel composition scenario and type of efficiency formulation (stack- or system- level).

Table XVI: Stack-level efficiency map in nominal conditions in the 100% H_2 compositions.

Stable operation points - η_{el} (%) @ 30 A	**FU 50%**	**FU 60%**	**FU 70% [640 °C – 710 °C]**
$\eta_{STACK\ w/o\ FU}$	35.0%	41.7%	48.0% [47.9 - 48.0%]
$\eta_{STACK\ w/FU_{th}}$	70.1%	69.4%	68.6% [68.4 - 68.6%]
$\eta_{STACK\ w/FU_{exp}}$	70.1%	69.4%	68.6% [68.4 - 68.6%]
$\eta_{STACK\ w/o\ FU\ H2\ equivalent}$	-	-	-
$\eta_{STACK\ w/FU_{th}\ H2\ equivalent}$	-	-	-
$\eta_{STACK\ w/FU_{exp}\ H2\ equivalent}$	-	-	-
$\eta_{STACK\ w/o\ FU\ chem\ conv}$	-	-	-
$\eta_{STACK\ w/FU_{th}\ chem\ conv}$	-	-	-
$\eta_{STACK\ w/FU_{exp}\ chem\ conv}$	-	-	-

Table XVII: System-level efficiency map in nominal conditions in the 100% H_2 compositions.

Stable operation points - η_{el} (%) @ 30 A	**FU 50%**	**FU 60%**	**FU 70% [640 °C – 710 °C]**
η_{SYSTEM}	41.4%	49.3%	56.8% [56.6 – 56.8%]
$\eta_{SYSTEM\ w/FU_{th}}$	70.0%	69.5%	68.6% [68.4 – 68.6%]
$\eta_{SYSTEM\ w/FU_{exp}}$	70.0%	69.5%	68.6% [68.4 – 68.6%]
$\eta_{SYSTEM\ H2\ equivalent}$	-	-	-
$\eta_{SYSTEM\ w/FU_{th}\ H2\ equivalent}$	-	-	-
$\eta_{SYSTEM\ w/FU_{exp}\ H2\ equivalent}$	-	-	-
$\eta_{SYSTEM\ chem\ conv}$	-	-	-
$\eta_{SYSTEM\ w/FU_{th}\ chem\ conv}$	-	-	-
$\eta_{SYSTEM\ w/FU_{exp}\ chem\ conv}$	-	-	-

Table XVIII: Stack-level efficiency map in nominal conditions in the 67% H_2 + NG compositions.

Stable operation points - η_{el} (%) @ 30 A	**FU 50%**	**FU 60%**	**FU 70% [640 °C – 710 °C]**
$\eta_{STACK\ w/o\ FU}$	36.7%	43.9%	50.4% [50.1% - 50.5%]
$\eta_{STACK\ w/FU_{th}}$	73.3%	73.1%	72.0% [71.6% - 72.2%]
$\eta_{STACK\ w/FU_{exp}}$	61.3%	63.0%	67.1% [66.1% - 67.9%]
$\eta_{STACK\ w/o\ FU\ H2\ equivalent}$	34.6%	41.3%	47.5% [47.2% - 47.6%]
$\eta_{STACK\ w/FU_{th}\ H2\ equivalent}$	69.1%	68.9%	67.9% [67.5% - 68.0%]
$\eta_{STACK\ w/FU_{exp}\ H2\ equivalent}$	57.8%	59.3%	63.2% [62.3% - 64.0%]
$\eta_{STACK\ w/o\ FU\ chem\ conv}$	41.2%	47.8%	50.9% [51.0% - 50.5%]
$\eta_{STACK\ w/FU_{th}\ chem\ conv}$	82.4%	79.6%	72.8% [72.9% - 72.2%]
$\eta_{STACK\ w/FU_{exp}\ chem\ conv}$	68.8%	68.6%	67.8% [67.3% - 67.9%]

Table XIX: System-level efficiency map in nominal conditions in the 67% H_2 + NG compositions.

Stable operation points - η_{el} (%) @ 30 A	**FU 50%**	**FU 60%**	**FU 70% [640 °C – 710 °C]**
η_{SYSTEM}	43.2%	51.5%	59.5% [59.1% - 59.6%]
$\eta_{SYSTEM\ w/FU_{th}}$	72.7%	72.5%	71.6% [71.2% - 71.8%]
$\eta_{SYSTEM\ w/FU_{exp}}$	62.0%	63.5%	67.2% [66.3% - 68.1%]
$\eta_{SYSTEM\ H2\ equivalent}$	40.8%	48.7%	56.3% [55.9% - 56.4%]
$\eta_{SYSTEM\ w/FU_{th}\ H2\ equivalent}$	68.8%	68.6%	67.8% [67.3% - 67.9%]
$\eta_{SYSTEM\ w/FU_{exp}\ H2\ equivalent}$	58.6%	60.1%	63.6% [62.8% - 64.4%]
$\eta_{SYSTEM\ chem\ conv}$	47.9%	55.6%	60.0% [60.0% - 59.5%]
$\eta_{SYSTEM\ w/FU_{th}\ chem\ conv}$	80.8%	78.2%	72.2% [72.2% - 71.6%]
$\eta_{SYSTEM\ w/FU_{exp}\ chem\ conv}$	68.8%	68.6%	67.8% [67.3% - 67.9%]

Table XX: Stack-level efficiency map in nominal conditions in the 100% NG compositions.

Stable operation points – η_{el} (%) @ 30 A	**FU 50%**	**FU 60%**	**FU 70% [640 °C – 710 °C]**
$\eta_{STACK\ w/o\ FU}$	35.1%	42.0%	48.6% [48.3% - 48.7%]
$\eta_{STACK\ w/FU_{th}}$	70.1%	70.1%	69.5% [69.1% - 69.5%]
$\eta_{STACK\ w/FU_{exp}}$	63.4%	64.4%	63.8% [62.7% - 63.8%]
$\eta_{STACK\ w/o\ FU\ H2\ equivalent}$	33.3%	39.9%	46.2% [45.9% - 46.2%]
$\eta_{STACK\ w/FU_{th}\ H2\ equivalent}$	66.6%	66.6%	66.0% [65.6% - 66.0%]
$\eta_{STACK\ w/FU_{exp}\ H2\ equivalent}$	60.2%	61.1%	60.6% [59.6% - 60.6%]
$\eta_{STACK\ w/o\ FU\ chem\ conv}$	36.6%	43.2%	50.0% [50.3% - 50.2%]
$\eta_{STACK\ w/FU_{th}\ chem\ conv}$	73.3%	72.1%	71.5% [71.9% - 71.7%]
$\eta_{STACK\ w/FU_{exp}\ chem\ conv}$	66.3%	66.2%	65.7% [65.3% - 65.7%]

Table XXI: System-level efficiency map in nominal conditions in the 100% NG compositions.

Stable operation points – η_{el} (%) @ 30 A	**FU 50%**	**FU 60%**	**FU 70% [640 °C – 710 °C]**
η_{SYSTEM}	48.0%	57.6%	65.8% [65.5% - 65.9%]
$\eta_{SYSTEM\ w/FU_{th}}$	72.1%	72.1%	71.5% [71.1% - 71.5%]
$\eta_{SYSTEM\ w/FU_{exp}}$	63.1%	64.3%	63.7% [62.0% - 63.2%]
$\eta_{SYSTEM\ H2\ equivalent}$	44.1%	53.0%	60.5% [60.1% - 60.5%]
$\eta_{SYSTEM\ w/FU_{th}\ H2\ equivalent}$	66.3%	66.2%	65.7% [65.3% - 65.7%]
$\eta_{SYSTEM\ w/FU_{exp}\ H2\ equivalent}$	58.0%	59.1%	58.5% [57.0% - 58.1%]
$\eta_{SYSTEM\ chem\ conv}$	50.4%	59.3%	67.9% [68.9% - 68.5%]
$\eta_{SYSTEM\ w/FU_{th}\ chem\ conv}$	75.7%	74.1%	73.8% [74.8% - 74.4%]
$\eta_{SYSTEM\ w/FU_{exp}\ chem\ conv}$	66.3%	66.2%	65.7% [65.3% - 65.7%]

For the 100% H_2 composition, some formulations of the efficiency (Eq. 65 – 76) are not defined because the contribution given by the carbon-containing gases is non-existent, hence they lead to identical results.

The formulations of the efficiency based on the total inlet-outlet flow rates, which are indicators of the goodness of the total inlet fuel conversion (based on Eq. 59, 62, 65, 68, 71, 74), tend to show lower values especially at stack level (between 35-50%, as shown in the aforementioned tables below) than those obtained only considering the reacting fuel (60 – 75%). 100% NG is the composition with best performance, followed by the 67% H_2 + NG and the 100% H_2. Such values are limited by the single-pass FU since the chemical energy of the unreacted fuel at the outlet is lost. The stack efficiency calculated with this formulation increases with increasing single-pass FU since the amount of unconverted fuel is reduced.

The polarization curves (Figure 30) for the three composition scenarios are all quite linear, denoting a stable operation in the ohmic regime, with the exception of the 100% NG composition around the nominal load current which shows a slightly non-linear voltage drop, possibly related to off-gas management problems of the test bench setup (high content of steam at the exit of the fuel side may cause flooding and incomplete gas evacuation, also denoted by anomalous values of the output pressure). The drop of performance for the reformate compositions with respect to the 100% H_2 composition can be ascribed to the fact that the reformate compositions entail more complex reaction chains, with possible kinetic effects of the chemical reactions (not all the CH_4 and CO is completely converted to H_2). In addition, the SMR reaction is strongly endothermal, causing a reduction of the in-stack temperature (negatively affecting the internal resistance and thermally activated phenomena, which is closely connected to the polarization slope which is the main affected parameter).

In alignment with the results obtained from the polarization tests, the performance maps confirm that the 100% H_2 composition shows the highest power output (385.2-394.5 W) respect to the reformate compositions (379.2-387.6 W and 367.8-373.2 W for 67% H_2 + NG and 100% NG, respectively). The variation of output power with temperature is quite limited since the lower temperature is quite close to the nominal temperature (640°C vs. 660°C) and thermal inertia might limit the performance deviation while at high temperature (710°C) possibly the in-stack optimal temperature window is exceeded, inhibiting the beneficial effect of the increase in temperature. The power variation with FU is stronger (between ± 1-2%) respect to the variation with temperature (between ± 0.5-1%).

Some considerations regarding the efficiencies are now made.

An increase of FU is performed by reducing the fuel chemical inlet power; as reported in the Tables IV – IX, this is followed by an increase in the efficiencies that do not take into account the FU itself, both at stack- and system- level. This is because low FU conditions are penalized by the higher lost chemical energy of the unreacted fuel.

In the definition of the efficiencies that consider the FU, be it theoretical or experimental, the variation of the results is not extremely evident (below 5%), regardless of the FU value: this is because a decrease in inlet chemical power (hence increase of the FU) is to a greater extent than the reduction of electrical power that occurs, and it is such that, overall, $\eta_{w/FU}$ remains quite stable as FU varies. To be more precise, it can be stated that as FU increases, $\eta_{w/FU}$ decreases slightly, since the lower quantity of fuel fed to the stack hinders the chemical and electrochemical reactions.

The results also indicate that the efficiencies that include FU_{th} are always more optimistic than those with FU_{exp}: the latter is always higher than the former, because it takes into account the fact that the inlet fuel is not entirely converted into H_2, hence a lower amount of H_2 to react electrochemically is available. With less H_2 available but equal H_2 reacting, FU increases. Therefore as a certain FU_{th} is fixed, the corresponding FU_{exp} is always higher, thus $\eta_{w/Fuexp}$ is the equivalent of $\eta_{w/Futh}$ calculated with a higher FU. In this case, the best performance is given by the 100% H_2 scenario, with the 67% H_2 + NG and 100% NG with similar values: no significant differences between compositions can be observed, and they do not exceed the 5-6 % range.

With all the three formulations (standard, H_2 equivalent and chemical conversion) similar results are achieved: given a certain composition, the gap between resulted always within the 5-6% range, with the most optimistic definition being the “chemical conversion” (Eq. 71 – 76).

It can also be observed that the highest stack-level efficiency is obtained for the 67%H_2 + NG composition, followed by the 100% NG composition and only lastly by the 100% H_2 composition: that is because the input chemical power contained by the fuel gas in the reformate compositions is lower (ca. 755-760 W) than the one contained in the 100% H_2 composition (ca. 800 W) due to higher H_2O and CO_2 content which dilute the mixture and decrease the calorific value of the fuel. This means that, at the stack level, although the highest power output is obtained with 100% H_2 conditions, the overall energy balance is more advantageous for the reformate compositions since similar electrical output power is obtained with a lower energy quality of the inlet fuel, denoting a better valorization of the processed fuel.

The impact of temperature on the efficiency (in all three formulations) is limited (between ±1%) due to the limited impact on stack performance for the abovementioned reasons.

At system-level the trend of efficiency among the gas composition scenarios is mainly affected by the recirculation of the off-gas to the external pre-reformer, which in turn affects the internal energy balance of the system and determines the requirement of fresh fuel. In fact, considering the higher LHV of CH_4 respect to H_2 on a volume basis (11 kWh/Nm^3 vs. 3 kWh/Nm^3, respectively [220]) and the higher RR and global system, the 100% NG case requires much less fresh fuel respect to the 100% H_2 case (51.64 Nl/h vs. 230.44 Nl/h).

3.3 Research Question 3: What is the potential of rSOC systems for integration with renewable energy sources and for energy storage applications in residential and industrial scenarios?

Another application domain of particular relevance is the integration of different clean and efficient energy production technologies in order to enhance the strengths of each while mitigating their respective limitations. In this context, the coupling of reversible solid oxide cell (rSOC) technology with photovoltaic generation exhibits substantial potential. This aspect is specifically investigated in the present doctoral work through the development of a dedicated experimental test bench and the implementation of a modeling framework, both associated with an ad-hoc experimental study described in detail in Section 2.3.

An electrolyte-supported 5 x 5 cm (active area 16 cm^2) single cell is investigated, and cell performance, prior to the actual test campaign, have been evaluated through polarization curves, both in fuel cell and electrolysis mode. The system includes a temperature-programmed furnace that houses the cell, allowing it to reach and maintain the desired operating temperature consistently throughout the test runs. Pictures of the cell, cell housing and of test station in ENEA facilities can be found in Figure 32.

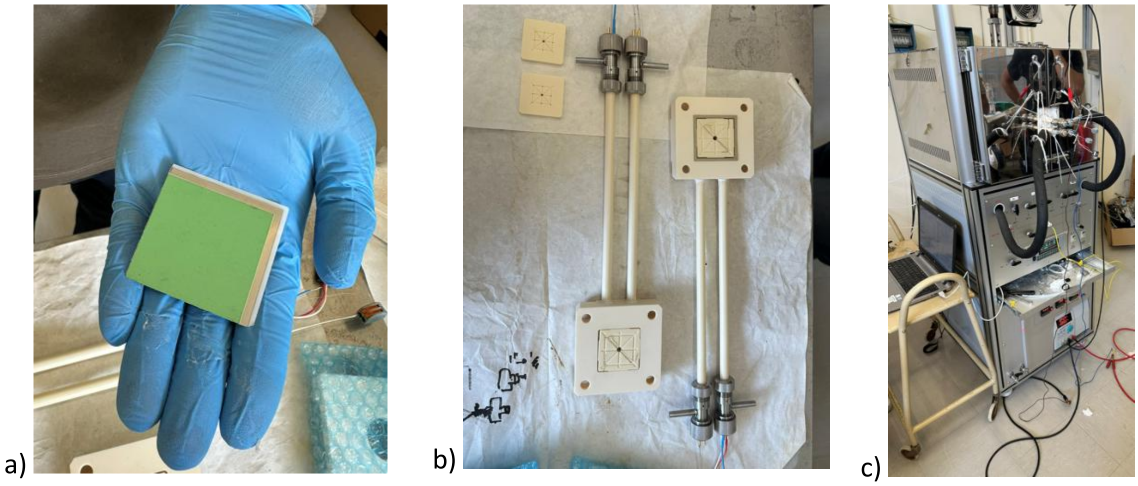

***Figure 32**:* Cell (a), cell housing (b) and single cell test station (c) utilized for the test runs.

After system assembly, the startup procedure and the cell reduction are performed. Subsequently, cell performance is assessed: in SOFC mode, the fuel flow and composition set are H_2/N_2 90/10 %vol, with a total flow of 300 Nml/min and an air flow of 800 Nml/min at the air electrode-side; in SOEC mode, the composition is H_2O/H_2 70/30 %vol, again with a total flow of 300 Nml/min at fuel electrode-side, and 800 Nml/min at air electrode-side. A composition with a higher water content was not obtainable due to test rig limitations. The same compositions and flow rates have been used in the following test campaign itself. The nominal working temperature of the cell was set to 800 °C. Feed-gas compositions, flow rates and other operating parameters are given in Table XXII, and curves in both modes are reported in Figure 33.

***Table XXII**: experimental working conditions for the 16 cm^2 electrode-supported single cell*

Working mode	**Fuel flow rate**	**H_2**	**H_2O**	**N_2**	**Air flow rate**
SOFC	300 Nml/min	270 Nml/min	-	30 Nml/min	800 Nml/min
SOEC	300 Nml/min	210 Nml/min	90 Nml/min	-	800 Nml/min

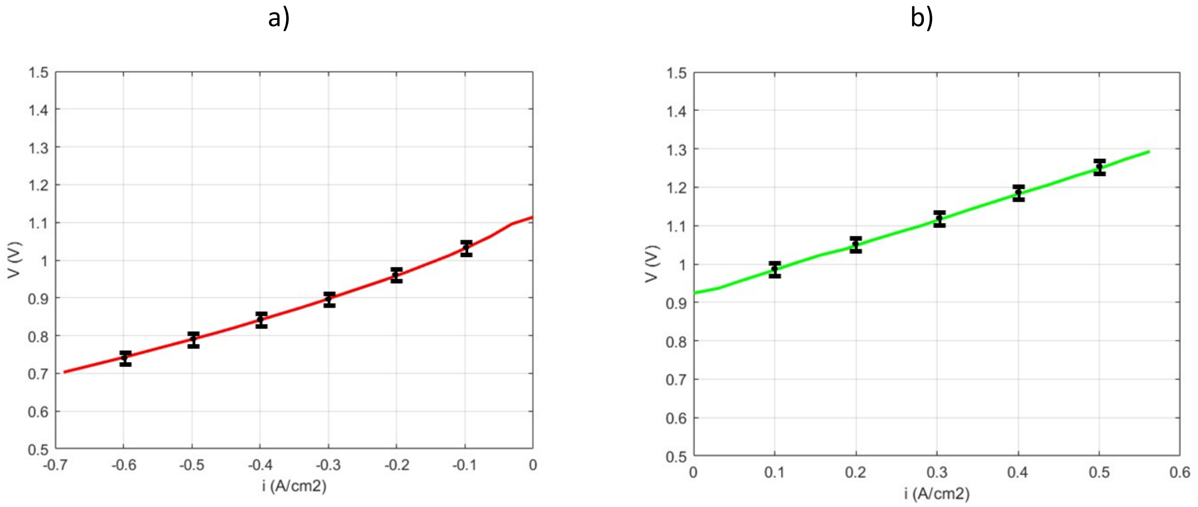

***Figure 33**:* Single cell characterization – IV curves in SOFC (a) and SOEC (b) mode.

The experiments were carried out imposing a 1 A/min current sweep until the voltage of 0.7 V was reached in SOFC mode (1.3 V in SOEC mode). In fuel cell mode, the maximum power delivered by the cell was -7.73 W at 0.69 A/cm^2. The fuel utilization at maximum power was 28.4%. In electrolysis mode, the maximum cell power absorption was 11.64 W at 0.56 A/cm^2, with the 30% steam conversion.

According to the specifications provided by the test station manufacturer, the voltage reading is subject to an uncertainty of ± 1%. Assuming an average operating voltage of 1 V, this corresponds to a measurement error of ± 10 mV. The error bars shown in Figure 33 provide a graphical representation of the propagated uncertainty across the IV curves.

For this experimental campaign, excessively high levels of fuel utilization/steam conversion were intentionally avoided to prioritize achieving higher current densities. To this end, a relatively high inlet gas flow rate was employed relative to the cell size, which allowed a substantial increase in current density (significantly variable during the test runs) in order to focus on maximizing electrical stress on the cell rather than fluid dynamic stress. As shown by the highly stable I-V curves across the entire range of current densities examined in Figure 33, consistent behavior and stable performance across all runs is ensured, and no signs of concentration losses were observed in either SOFC nor SOEC mode, despite the high currents reached. The operating window for both SOFC and SOEC modes was deliberately chosen to avoid concentration polarization, maintaining current densities within regimes dominated by activation and ohmic losses. This approach isolates the degradation mechanisms to electrochemical phenomena, excluding mass transport limitations as a contributing factor.

3.3.1 Typical days definition

To extrapolate typical days from the yearly energy consumption dataset, statistical learning in the form of clustering has been used, that is a type of unsupervised learning [221], [222]. Typical days are then used to run the experimental campaign. In detail, the K-means clustering algorithm has been implemented [223], [224], [225], [226], [227]. The goal of this technique is to find clusters, or subgroups, in a dataset. Each cluster is made of components similar to each other according to a mathematical definition. The algorithm divides the dataset in a predetermined number of clusters and then iteratively rearrange their composition to minimize the cluster variation, as shown in Eq. 95:

$$minimize\left\{\sum_{j=1}^{K} W(C_k)\right\} \tag{95}$$

where $W(C_k)$ is the Euclidean distance between the vectors included in the cluster k, while K is the number of clusters. We apply the algorithm to each month separately looking for two clusters. The two resulting typical days are represented by the two centroids of the clusters. In this way, we can represent each month with two typical days counting for working days and week-end days.

Once the most representative days for each month have been determined (that is, the most demanding on the cell in terms of power out of the two selected by the algorithm for each month), the 12 net profiles at real scale level are obtained, as defined by Eq. 78. The 12 typical days are shown in Table II.

Although not explicitly specified by the test bench manufacturer, a conservative current measurement uncertainty of ± 10 mA has been assumed across all operating points. Combined with the previously stated voltage uncertainty, the resulting propagated error on the power values reported in Table XXIII is estimated to be approximately ± 2 %. This level of uncertainty is sufficiently low to support the reliability of the calculations presented.

***Table XXIII**: Net power profiles of the 12 most representative days of the year, at real-scale level*

	Net power (W)											
Hour of day (h)	**Jan**	**Feb**	**Mar**	**April**	**May**	**Jun**	**Jul**	**Aug**	**Sep**	**Oct**	**Nov**	**Dec**
00 – 1	-103.9	-142.0	-121.1	-100.5	-155.1	-101.9	-176.4	-79.1	-152.6	-74.4	-77.9	-76.6
1 – 2	-214.5	-122.4	-93.9	-180.8	-88.3	-77.6	-143.3	-84.7	-98.1	-120.6	-113.2	-76.1
2 – 3	-75.8	-132.4	-140.6	-120.9	-77.5	-77.2	-78.8	-162.4	-153.3	-137.5	-172.1	-77.8
3 – 4	-78.4	-77.9	-81.3	-81.1	-117.3	-114.2	-79.1	-98.7	-93.6	-154.8	-124.8	-131.6
4 – 5	-100.1	-119.3	-145.4	-94.3	-172.5	-265.4	-56.8	-152.5	-85.2	-109.6	-79.5	-319.1
5 – 6	-205.2	-208.9	-309.6	-288.3	-146.7	112.6	16.0	11.9	-132.1	-177.3	-216.5	-203.6
6 – 7	-642.2	-772.4	-1082.5	365.2	677.3	1043.0	591.8	402.7	66.5	-690.9	-438.4	-1400.1
7 – 8	791.7	543.3	835.9	1383.6	1962.7	1691.3	1078.9	1765.9	1396.8	1006.1	772.3	112.5
8 – 9	2380.3	2452.2	3027.3	3074.6	2890.3	2946.7	3243.0	1471.6	1395.9	1008.4	2251.5	1893.6
9 – 10	2746.7	3080.9	3844.4	3296.3	2999.6	2897.6	4280.1	3088.3	3910.3	2846.5	3835.0	2866.1
10 – 11	3213.6	4456.2	3723.2	4984.5	4154.1	3680.1	4559.5	3996.9	3311.4	2942.5	3840.8	4001.7
11 – 12	5051.6	4436.4	5235.6	4601.6	4979.3	3832.8	4427.0	4267.1	4466.9	3577.3	3374.0	4216.9
12 – 13	4792.7	4009.8	4627.5	4199.5	4692.5	3649.6	4830.6	4438.4	3530.6	3548.0	3415.4	4232.9
13 – 14	2608.6	3351.1	4418.5	3854.6	3562.7	3800.8	3836.3	3785.6	2813.8	2746.8	2289.3	3553.3

14 – 15	1474.7	2941.0	3032.5	2678.9	2504.4	1931.1	3283.2	2916.5	774.9	2045.8	2312.9	1483.2
15 – 16	-157.3	1587.3	2396.3	1016.5	1557.3	2172.6	1616.3	1844.8	-73.9	740.8	183.4	-1128.3
16 – 17	-306.7	-123.7	341.9	754.6	835.8	666.8	745.6	791.4	178.5	-732.6	-621.1	-421.3
17 – 18	-1330.1	-378.3	-790.4	-227.5	-48.4	111.1	-150.6	-1056.4	-431.4	-916.6	-333.0	-343.3
18 – 19	-458.6	-513.4	-158.5	-397.1	-206.2	226.8	-440.4	-959.9	-1058.7	-646.3	-1501.7	-150.8
19 – 20	-125.1	-752.7	-319.4	-308.5	-696.9	-176.6	-716.6	-706.2	-696.2	-888.6	-857.4	-292.1
20 – 21	-314.9	-198.1	-473.8	-645.1	-190.3	-248.8	-723.6	-1720.6	-236.9	-1110.8	-569.8	-1009.2
21 – 22	-213.4	-246.9	-170.1	-164.3	-144.6	-161.7	-2313.9	-334.5	-242.4	-199.5	-475.6	-889.1
22 – 23	-99.3	-163.7	-118.5	-187.2	-154.1	-196.4	-2644.2	-191.0	-224.2	-353.6	-199.7	-428.8
23 – 24	-77.6	-77.5	-77.5	-224.8	-132.6	-111.3	-1948.2	-100.1	-123.9	-126.9	-174.6	-132.4

Despite the simplification of the case study and its target to bring out the most challenging working condition for the rSOC single cell, some of the main characteristics of the real net power profile (Figure 22) have remained quite unaltered: the maximum power absorbed in SOEC mode is 5.23 kW, recorded in March’s most representative day at 11 a.m., not far from the actual maximum power in SOEC, which the simulation estimates to be 5.66 kW (see Section 2.3).

In fuel cell mode, the approximation with 12 representative days identifies a maximum power production of -2.64 kW, whereas the simulation over the entire year was -4.54 kW. The difference between these values is to be attributed to the low frequency of occurrence of particularly high levels of power production (e.g. < -3 kW).

The final step prior to the definition of the experimental campaign consists of the downscaling of the values obtained at real scale level. Two scaling factors are defined, as in Eq. 96 and Eq. 97.

$$scaling\ factor\ in\ SOEC\ (SFE) = \left|\frac{max\ power\ stack\ in\ SOEC}{max\ power\ single\ cell\ in\ SOEC}\right| = \frac{5240\ W}{11.64\ W} = 450 \tag{96}$$

$$scaling\ factor\ in\ SOFC\ (SFFC) = \left|\frac{max\ power\ stack\ SOFC}{max\ power\ single\ cell\ SOFC}\right| = \frac{2640\ W}{7.73\ W} = 341 \tag{97}$$

SFE is considered, as it is the largest of the two and therefore it is an indicator of the limiting condition. Dividing the real scale level values by the scaling factor in electrolysis mode enables the cell to work in its operating power window: the maximum real scale SOEC and SOFC power correspond to 11.64 W and -5.88 W at single cell level respectively, within the 11.64 W ÷ -7.73 W range identified in Section 3.3.

After these considerations, the 12 net power profiles are split into SOEC and SOFC mode, and ultimately correspond to the power profiles imposed to the laboratory rSOC. It must be noted that the trends remain the same, the power magnitude has been downscaled at single cell level.

3.3.2 CUSUM approach and cell characterization

The Cumulative Sum (CUSUM) method is a sequential analysis technique used for change detection monitoring. It takes as input a reference value of a specific variable and its observed values over time. The algorithm accumulates the deviations between the current value and the reference value over time, thus providing the magnitude of the variations of the examined variable. Each point on the CUSUM chart represents the cumulative sum of deviations observed up to that moment. This method allows for a deeper analysis of the system's energy behavior [228], [229].

In the specific case under consideration, the reference variable used to monitor the system's performance was the cell efficiency, defined according to the cell's operating mode (SOFC or SOEC) as indicated in Eq. 98 and Eq. 99.

$$\eta_{cell,SOFC} = \frac{P}{Q_{H_2} \cdot LHV_{H_2}} \tag{98}$$

$$\eta_{cell,SOEC} = \frac{Q_{H_2} \cdot LHV_{H_2}}{P} \tag{99}$$

$$P = V \cdot I \tag{100}$$

$$Q_{H_2} = \frac{I}{2 \cdot F} \tag{101}$$

Where $\eta_{cell,\,SOFC}$ e $\eta_{cell,\,SOEC}$ [-] are the cell efficiencies in SOFC and SOEC modes, respectively, P [W] is the power produced (SOFC) or absorbed (SOEC), Q_{H2} [mol/s] is the flow rate of hydrogen electrochemically converted (SOFC) or produced (SOEC), F is the Faraday's constant [96487 C/mol], V [V] and I [A] are cell voltage and current. As observed, the considered reference parameter was the single-pass cell efficiency, which accounts only for the amount of fuel/water electrochemically converted and not the total supplied to the cell, following the definition given by [196].

Using this definition, the cell efficiency was mapped across the entire range of current densities explored during the performance characterization analysis shown in Figure 34, both in SOFC and SOEC mode.

Based on the specifications provided by the manufacturer, the flow meters are subject to a measurement uncertainty of ±0.5%. Under these conditions, the resulting propagated error on the calculated efficiency is estimated at approximately ± 2.3 %.

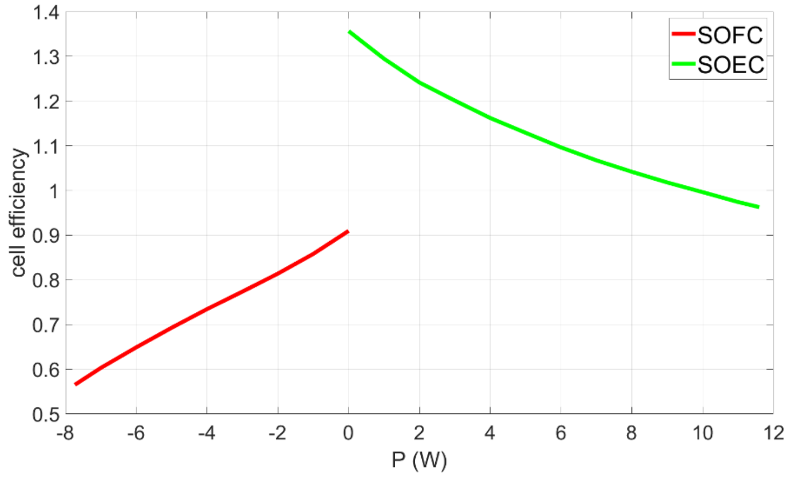

Figure 34: plots of the cell efficiencies defined in Eq. 98 and Eq. 99, in SOFC and SOEC mode.

Figure 34 shows the reference efficiency values, calculated at the beginning of the campaign using the definitions provided in Eq. 98 and 99. These efficiency values are hereinafter referred to as the *expected cell efficiency*, or $\eta_{exp}(i)$ [-]. The efficiency will be evaluated at each time step of the experimental campaign (1 min), and any deviation of the instantaneous efficiency from the reference value for a given current density will be considered by the CUSUM method.

The efficiency ratio (ER) is now defined:

$$ER = \frac{\eta_{curr}(i)}{\eta_{exp}(i)} \tag{102}$$

Where $\eta_{curr}(i)$ [-] is the current cell efficiency.

Given that the study's resolution is 1 minute, the *efficiency ratio difference* (*ERD*) is calculated at each time interval (t). The *ERD* represents the difference between the efficiency ratio (*ER*) and the reference efficiency ratio (*RER*), which is set to 1, assuming the ideal scenario where the cell maintains the same efficiency as at the beginning of the campaign for a given current density.

Negative *ERD* values indicate a decline in cell performance during that interval, with larger negative values corresponding to more significant performance drops. Conversely, positive values suggest improved performance.

$$ERD(t) = ER(t) - RER(i) \tag{103}$$

Finally, the CUSUM efficiency ratio difference (CUSUM) is defined as the sum of all ERD values accumulated throughout the campaign:

$$CUSUM = \sum_t ERD(t) \tag{104}$$

It is important to emphasize that *CUSUM* is a dimensionless parameter whose absolute value alone is meaningful only when compared with the same parameter calculated under identical conditions in a different experimental campaign. Therefore, its absolute value is useful for comparing SOFC and SOEC campaigns, while its trend and the slope of its curve plotted over time during each campaign represent the cell's performance decline and, consequently, the degradation it is experiencing.

Moreover, since CUSUM is a dimensionless parameter whose absolute value is meaningful only when compared across different operating modes, its direct interpretation in terms of cell performance degradation remains limited. Given that the measurement uncertainties on voltage, current, and flow rate are identical for both SOFC and SOEC modes, the propagated error on CUSUM is effectively the same in each case. As the focus of the analysis lies in the comparative evaluation of CUSUM between these two modes, assessing the uncertainty propagation on CUSUM itself is not considered particularly relevant.

Following the initial characterization tests, the cell was operated following the procedure described in Section 2.3 and illustrated in Table XXII. The first set of tests was conducted in SOFC mode, followed by the SOEC phase of the campaign.

Due to an instrumental limitation, the electronic load was unable to absorb (in SOFC mode) or supply (in SOEC mode) and maintain an electrical load below 0.28 W, corresponding to a minimum current of 0.25 A (0.015 A/cm^2) in SOFC operation and 0.65 A (0.04 A/cm^2) in SOEC operation. In practice, this means that no power was absorbed or supplied whenever the minimum power limit was not met. Power analysis showed that all power levels below 3.62 % of the maximum power in SOFC mode and 2.41 % in SOEC mode were therefore excluded. As a result, the unaccounted energy during the entire experimental campaign represented approximately 10 % of the total energy produced by the cell in SOFC mode and 0.31 % of the total energy consumed in SOEC mode. Even if the electronic load had been capable of imposing any current value, operating below 0.015 A/cm^2 (SOFC) or 0.04 A/cm^2 (SOEC) would have subjected the cell to an electrochemical load so low as to be practically negligible. Such low current densities are not expected to cause any measurable electrochemical stress or degradation. For comparison, Shen et al [230] observed virtually no degradation in SOEC operation at 0.3 A/cm^2 after 2000 h, confirming that degradation effects are still insignificant at much higher current densities than those excluded here.

Although in SOFC mode the unaccounted energy represents about the 10 % of the total, this value is determined mainly by the long duration of low-load periods rather than by the negligible magnitude of the excluded currents (below 2 % of the maximum). Consequently, these omitted operating points have a marginal impact on cell degradation, as electrochemical activity in that range is minimal.

While this condition may slightly reduce the representativeness of the imposed load cycles, it has no effect on the cell degradation behavior, given the irrelevance of the excluded current range. Since the main objective of this experimental campaign was to investigate the cell's response and degradation under realistic, highly dynamic, and electrically stressful conditions, the exclusion of such low-load periods had virtually no influence on the final outcome.

Minimal voltage fluctuations were observed in SOFC mode, with a maximum deviation (under load) between the highest and lowest voltage of 14 mV (1.44%) between 17:00 and 18:00 in January. The highest standard deviation of the voltage was 4 mV. In SOEC mode, the fluctuations were more pronounced: Table XXIV reports the number of times the voltage oscillation (i.e., the difference between the current voltage and the maximum voltage) exceeded 5% and 10%, respectively, within a given time range, for each representative day. Over the course of the entire campaign, the 5% and 10% thresholds were exceeded on 404 and 145 occasions respectively, corresponding to 2.36% and 0.84% of the total SOEC operating time. This phenomenon certainly contributed to an accelerated degradation of the cell; however, given the low frequency of occurrence, it does not compromise the validity of the test.

Table XXIV: *count of voltage exceedances above 5% and 10% thresholds during the SOEC campaign*

Typical day	Number of 5% exceedances (% of time)	Number of 10% exceedances (% of time)
Jan	10 (0.7%)	3 (0.21%)
Feb	39 (2.71%)	9 (0.62%)
Mar	30 (2.08%)	8 (0.55%)
Apr	49 (3.4%)	23 (1.6%)
May	40 (2.78%)	13 (0.9%)
Jun	43 (2.99%)	21 (1.46%)
Jul	48 (3.33%)	16 (1.11%)
Aug	43 (2.99%)	14 (0.97%)
Sep	25 (1.74%)	9 (0.62%)
Oct	17 (1.18%)	8 (0.55%)
Nov	34 (2.36%)	13 (0.9%)
Dec	26 (1.8%)	8 (0.55%)
TOT	404 (2.34%)	145 (0.84%)

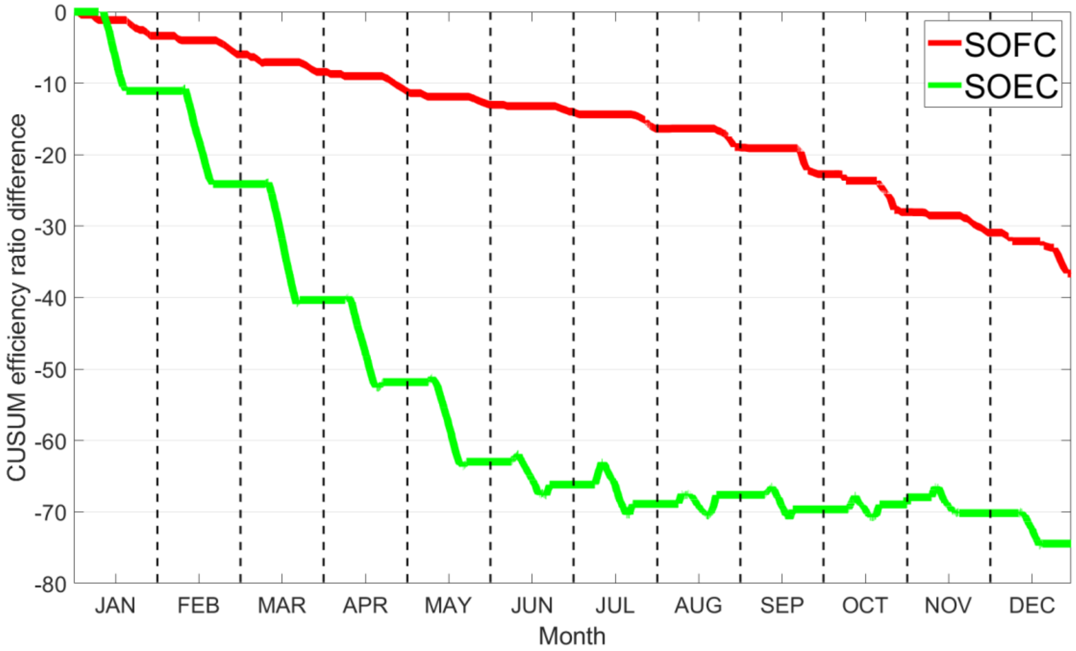

Figure 35: CUSUM trend across the entire test campaign, in SOFC and SOEC mode.

Figure 35 presents the CUSUM function trends (defined in Eq. 104) for both testing modes, which are used to analyze the drop in cell performance. As explained previously, the absolute CUSUM values for the two modes are compared only because they are calculated using the same method and time step. It is immediately evident that the test runs in SOEC mode have a more significant impact on degradation than those in SOFC mode, with a final CUSUM value of 36 for SOFC and 74 for SOEC. Electrolysis is thus responsible for 67% of the overall efficiency reduction, indicating double the degradation compared to fuel cell operation.

In SOFC mode, the degradation appears almost perfectly linear from minute 0 to minute 17280, with a slightly more pronounced deterioration towards the last quarter of the experimental campaign. This trend aligns with expectations: during the initial phase (when the cell is not degraded), a steady performance decay is observed. After several hours of load cycling, the accumulated degradation leads to a drop in cell voltage under the same current density, resulting in an increased current density absorbed by the electronic load to maintain the same power output. This loop accelerates the degradation rate, as observed in the final days of testing. For instance, the analysis for December shows that at 6:00, with a power output of 3.11 W, the initial IV curve (Figure 33) suggests an expected voltage of 957 mV and a current of 3.25 A. However, the cell operated at 945 mV and 3.29 A instead.

The analysis performed using the CUSUM approach also allowed the quantification of the degradation observed in the cell under both operating modes. A calculation in terms of voltage drop percentage, as commonly reported in the literature, could not be carried out due to the absence of constant load operation throughout the testing campaign. In this context, even a comparison between the IV curves obtained at the beginning and at the end of each test run would not have yielded meaningful results. Such a comparison would only reflect the performance deviation of the cell at the final state of each testing block (e.g., it would misleadingly suggest negligible degradation in SOEC, since – as shown in

Figure 35 – the cell's performance at the end of the SOEC campaign is very close to its initial values, thus neglecting any intermediate variations).

Therefore, the determination of the percentage performance decay was performed by evaluating the average deviation in cell efficiency from the reference value over the entire test duration. In SOFC mode, a performance degradation rate of 0.73 %/1000 h was observed, while in SOEC mode this value increased to 1.5 %/1000 h. This further confirms that the degradation observed in SOEC is approximately double that of SOFC. These values are quite consistent with the experimental literature on rSOC cells under variable load conditions, such as the work by Sampathkumar et al [165] in which a voltage degradation rate of 1.64 %/1000h in SOEC mode and 0.65 %/1000h in SOFC mode is observed, under fuel and steam utilization of 52%. Similarly, Riegraf et al. [166] instead report voltage degradation rates of +0.58 %/1000h in electrolysis mode and −1.23 %/1000h in fuel cell mode. The higher degradation rate during SOFC operation was attributed to a more pronounced relative increase in ohmic resistance, which was hypothesized to result from the complex interaction between temperature and electrical bias affecting the oxygen electrode contact.

Table XXIII shows that the temporal distribution of SOFC and SOEC operation is relatively balanced throughout the year, with about 12 hours of operation per mode daily. The electrical load curve in SOEC mode is more sensitive to monthly variations, with March-April reaching up to 1.5 times higher power levels than October-November. Additionally, in SOEC mode, power values are generally 2 to 3 times higher than those in SOFC, resulting in current densities and voltages closer to their respective limits. Current densities in SOEC mode exceed 0.50 A/cm^2, whereas in SOFC, except for the July outlier (-0.45 A/cm^2), they never exceed -0.26 A/cm^2. This phenomenon can also be observed in Figure 22, where the higher amplitude of power peaks in SOEC mode compared to SOFC is clearly visible, contributing more significantly to overall degradation.

This maximum current density ratio of *i_max_SOEC / i_max_SOFC* = 2 aligns well with the contributions to performance degradation from each mode, suggesting that, under equivalent loads, more similar overall CUSUM values – and thus similar degradation levels – can be expected, making the different load peaks one of the reasons why a higher degradation in SOEC was observed. The results obtained in this study therefore fall in between previous studies that identify SOFC mode as the most detrimental [63], [87], [163] and those that report greater degradation in SOEC [138], [164], [165], cited in previous sections, ultimately pointing out that, in absolute terms, the operation that proved to be the most demanding for the cell was electrolysis.

A theoretical review of the literature indicates that the higher degradation rate observed in SOEC operation arises from several mechanisms intrinsic to electrolysis conditions. In SOFC mode, the most common degradation processes include nickel coarsening and carbon deposition at the fuel electrode, chromium poisoning at the air electrode, and thermomechanical stresses [231], [232], [233], [234].

In the present system, many of these are negligible: carbon deposition is absent due to the lack of carbonaceous fuels, chromium poisoning is avoided in the absence of metallic interconnects, thermal stresses are minimized by the controlled operating temperature, and nickel coarsening is limited by the relatively low current densities. Conversely, during SOEC operation, the dominant degradation mechanisms reported in the literature are nickel coarsening and migration at high current densities and steam contents, delamination of the LSM oxygen electrode – significantly accelerated compared to SOFC mode – electrolyte (YSZ) degradation under the strongly corrosive environment of electrolysis, and thermal cycling effects [71], [73], [89], [217], [235], [236], [237].

Overall, degradation phenomena are markedly more pronounced under electrolysis conditions, explaining the experimentally observed degradation rate being approximately twice that of fuel cell operation.

Other factors contributing to the higher degradation rate in SOEC mode have been identified: (i) As previously mentioned, the previous SOFC campaign partially deteriorated the cell, which resulted into higher operating voltages than anticipated under any condition; (ii) The non-ideal water feed supply caused voltage spikes (voltage scattering), temporarily pushing voltage to higher levels, further exacerbating the degradation.

To further strengthen the validity of the CUSUM-based approach, the IV curves acquired at the end of each experimental campaign have now been included and are presented in Figure 36. It can be observed that, in SOFC mode, the IV curve obtained at the end of the campaign shows lower voltage values than the one recorded at the beginning of the test, corresponding to an average voltage decrease of approximately 1.14 % per 1000 h. Since efficiency and voltage are linked by a proportional relationship (see Eq. 98 and Eq. 100), the efficiency and voltage degradation trends appear to be well aligned.

A similar comparison was carried out for the SOEC mode. To avoid a direct comparison between the pre-test IV curve and the post-SOEC curve – which would include the degradation already accumulated during the preceding SOFC operation – an additional IV curve was acquired in SOEC mode immediately after the SOFC campaign. This intermediate measurement allowed to estimate the degradation contribution from the SOFC operation and to correct the final SOEC IV curve accordingly. The resulting SOEC curve therefore accounts solely for the degradation contribution (approximately 1.52 % per 1000 h, in terms of voltage) associated with the SOEC campaign, confirming the strong correlation between the CUSUM-based analysis and the conventional IV curve-based approach.

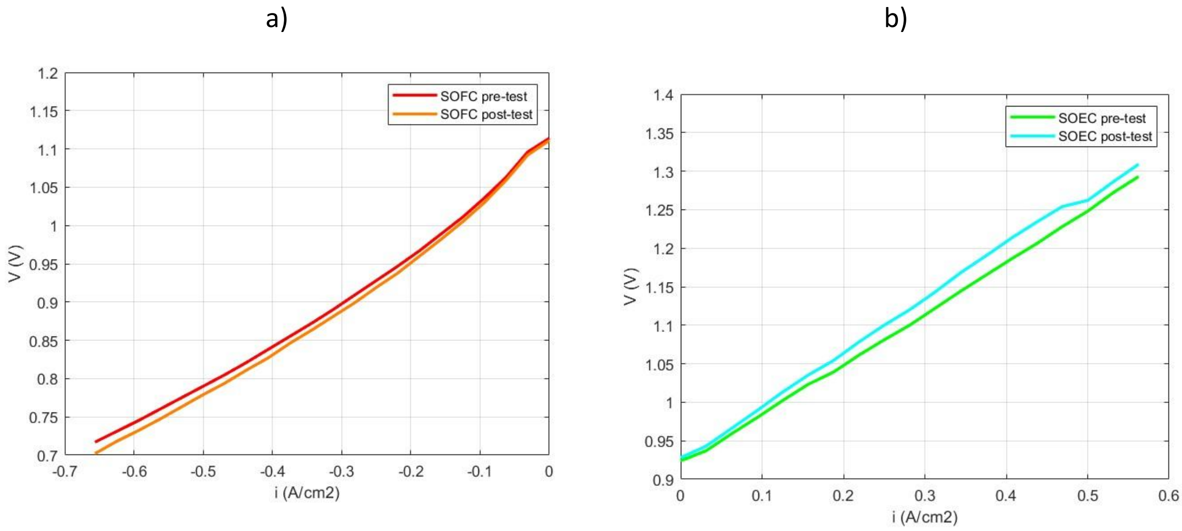
a)

b)

***Figure 36**:* Single cell characterization – comparison of IV curves pre- and post-experimental campaign, in SOFC (a) and SOEC (b) mode.

Unlike the main references in the literature, the electrical load imposed on the cell was, on average, lower, yet a higher average degradation was observed. This result highlights the tangible – though not dramatic – impact of variable load operation on the performance decay of the cell.

Lastly, the graph in Figure 35 highlights an initially higher degradation rate during the early operational hours, which stabilizes over time. In this specific case, there is a clear distinction between the January-May period (the first 120 hours of testing, during which the CUSUM value reaches 65) and the June-December period. The first 120 hours of testing account for over 86% of the cell degradation in SOEC mode, suggesting that the degradation rate was largely unaffected by the applied current densities or the cycling schedule. Instead, a significant decrease in the degradation rate occurred only after a sufficient amount of time had passed (break-in period), during which microstructural and electrochemical adjustments lead to accelerated degradation rates. After this transient phase, the degradation stabilizes, confirming the long-term impact of sustained SOEC cycling on cell performance. Some studies in the literature report a significant slowdown in performance decay after the first 500-1000 hours in SOEC mode [150], [238], most probably due to several factors: (i) changes in the active material (e.g., complete reduction) following electrochemical reactions in the early stages, (ii) electrode activation through the re-distribution of Nickel and Oxygen vacancies, and the progressive equilibration of the electrode-electrolyte interfaces under electrolysis polarization, (iii) potential exposure to impurities and contaminants that are gradually burnt off and removed from the cell housing over time, or (iv) stabilization of the initial degradation attributed to the deactivation of LSM (air electrode) [239]. Break-in period thus represents another cause of the markedly more pronounced degradation in SOEC.

Overall, the dynamic load tests confirmed that degradation was more pronounced in SOEC than in SOFC mode, in agreement with long-term stationary studies reported in the literature. However, under variable load conditions, the observed degradation rates were generally higher than those typically measured at constant current, even when compared to tests performed at higher average current densities. This indicates that, while solid oxide technology ensures a fast electrochemical response and stability to highly dynamic operating conditions, it also experiences an enhanced degradation rate when subjected to such fluctuating loads.

3.4 Research Question 4: What design strategies can be implemented to maximize the efficiency of rSOC stacks, and how do systems scaled for real-world applications respond in terms of performance and operational reliability?

The final key element of the present doctoral work addresses the investigation of solid oxide technology at an increased system scale. In particular, this part of the thesis focuses on the analysis of SOC-based systems operating at quasi-real, pre-commercial power levels, in order to assess how design choices, thermal management strategies, and system integration affect overall performance and operational reliability. This element of the doctoral thesis is intended to serve as a bridging link between the analyses focused on the electrochemical phenomena discussed in the previous sections and the design of a potential real-world, large-scale system intended to perform a specific operational function.

Figure 37 presents the evolution of the enthalpy flow of both the fuel and air streams across the main components of the system. A pronounced peak can be observed at the locations corresponding to the highest operating temperatures, reflecting the strong dependence of the enthalpy content on thermal energy input. For the air stream, the maximum enthalpy flow reaches approximately 5.2 kW, while for the fuel it is about 1.6 kW. This difference arises primarily from the different inlet volumetric flow rates, namely 329 Nl/min for the air and approximately 94 Nl/min for the fuel. The observed distribution highlights the importance of gas flow balancing in maintaining appropriate heat exchange and stable thermal gradients within the system.

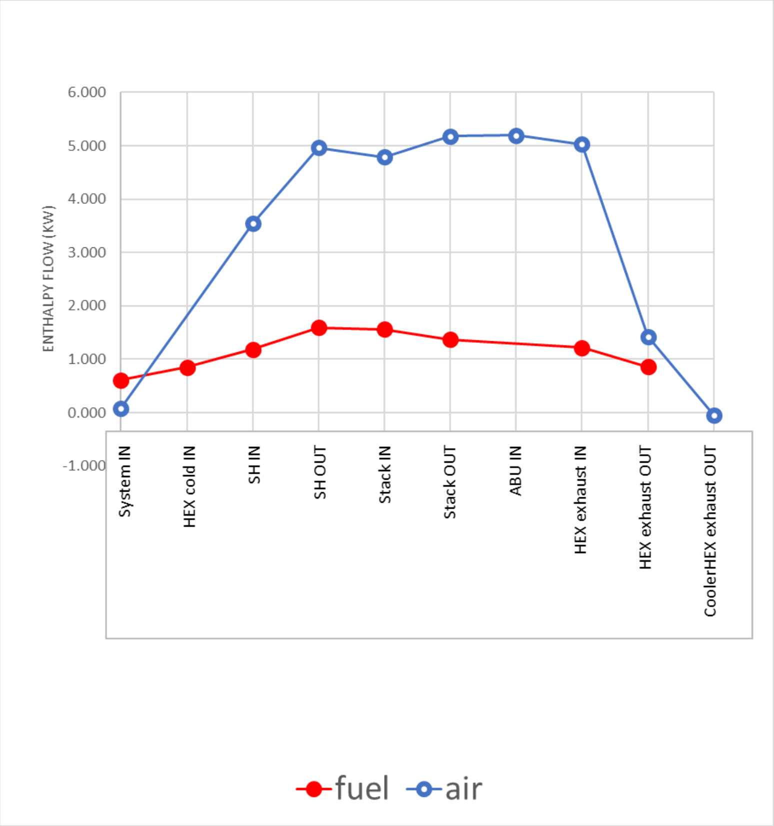

Figure 37: *Enthalpy flows for air and fuel in the 10 kW rSOC system*

Table XXV: *efficiencies of the 10 kW solid oxide stack system*

η	Value
η_{stack}	95.45%
η_{system}	57.99%
$\eta_{system,RAD}$	72.82%
$\eta_{system,RAD+EVAP}$	91.60%

Table XXV summarizes the results obtained from the efficiency calculations defined from Eq. 86 to Eq. 89. From the conducted tests and subsequent data analysis, it was found that the stack efficiency is remarkably high – exceeding 95%, according to the definition in Eq. 86. Such a value is, however, consistent with expectations for solid oxide cells operating in SOEC mode, which in the literature have been reported to achieve efficiencies in the range of 90–100% [240], [241], [242], and in some cases even above 100% [243], when accounting for the thermodynamic contribution of endothermic steam electrolysis reactions.

The overall system efficiency, on the other hand, is strongly dependent on the definition adopted. If the useful effect is considered solely as the chemical power stored in the produced hydrogen, together with the enthalpy flow of the outlet gas streams, an efficiency of approximately 58% is obtained. However, when the recoverable thermal energy from the FCHEX and ACHEX (the same heat currently lost to the environment through the radiator) is hypothetically exploited for district heating purposes, the system performance improves significantly, reaching about 73%.

In this analysis, the thermal energy assumed to be recovered at the radiator corresponds to 75% of the heat extracted from the process gases by the coolant, thus representing a conservative assumption of 75% heat recovery efficiency for a potential heat integration network. Considering a total input power – accounting for the stack, evaporator, fuel and air superheaters (FSH, ASH) and auxiliary systems – of approximately 15 kW, the effective useful energy output is estimated to be around 11 kW, while the residual losses amount to roughly 4 kW. Under the assumption of 75% thermal recovery efficiency, the net unrecoverable loss distributed across the system components reduces to about 3 kW.

It is reasonable to attribute the majority of these losses to the limited effectiveness of the evaporator in converting electrical power into thermal energy for steam generation, as well as to thermal dissipation through the hot box to the surrounding environment. Losses associated with the ACHEX and FCHEX are comparatively marginal, while those originating from intermediate components – such as FHEX, AHEX, ASH, and FSH – are encompassed within the overall heat losses of the insulated chamber.

Finally, according to the definition of efficiency provided by Eq. 89 – which assumes the availability of free steam at the system inlet – the overall efficiency rises to approximately 92%, corresponding to a further 19% improvement relative to the definition in Eq. 88. This result clearly underscores the dominant influence of the evaporator on the overall system performance and highlights the substantial efficiency gains that can be achieved in configurations where the steam supply is externally provided or thermally integrated with other industrial processes.

3.5 Cross-Scale Integration of Results and Knowledge Transfer Across SOC Platforms

The research activities presented in this thesis were deliberately structured across multiple experimental and modelling scales – ranging from localized single-cell diagnostics to stack-level operation and system-scale performance analysis – to generate complementary layers of knowledge and enable cross-scale interpretation. Although the individual studies were documented in separate publications, they do not represent isolated investigations. Instead, they constitute interconnected steps within a unified research pathway aimed at advancing the understanding, operation, and optimization of SOC and rSOC technologies under realistic conditions.

The ***first study*** focuses on localized diagnostics at the single-cell level, employing spatially resolved measurements of reactant conversion and product distribution. Beginning at this scale is essential for moving beyond globally averaged indicators and examining how electrochemical conversion is distributed across the active area. This approach reveals local gradients, non-uniform reactant utilization, and critical zones that cannot be detected through integral electrical measurements alone. The outcomes of this activity establish a mechanistic foundation for understanding conversion phenomena and emphasize the importance of spatial uniformity, fuel distribution, and local operating margins.

This first study connects directly with the ***third***, which extends the investigation by addressing the reversibility of SOCs and their coupling with external energy sources. At the same time, it provides a tangible demonstration of how the local phenomena observed at single-cell level manifest at the scale of a real system designed for a specific application. The study shows how local non-uniformities and cell-level degradation mechanisms propagate through the stack and ultimately influence the performance and efficiency of integrated systems.

The ***second study*** lays the groundwork for the transition to the next scale (short-stack), focusing on the suitability of SOC technology for a specific application – combined heat and power (CHP). The definitions, efficiency metrics, and methodological framework developed here are subsequently employed in both the third and fourth studies. Moreover, the third study includes experimental SOFC-mode operation, providing cell-level phenomena that are then examined at a different system scale, enabling an analysis of how these effects propagate as system size increases. The second and third studies therefore form a reciprocal link: one establishes the conceptual and methodological basis, while the other validates and extends it experimentally.

The ***fourth study*** represents an additional step toward larger system scales (10 kW), with the aim of assessing the applicability of SOC technology in real operational contexts. It provides a concrete perspective on what it means, in practice, to design and operate an energy-storage system of the type hypothesized in the third study for example. Through enthalpy and efficiency analyses, it offers a global view of how the phenomena observed at smaller scales translate into system-level behavior, thereby closing the loop between localized diagnostics, stack operation, and full-scale application.

Taken together, these studies form a research trajectory aimed at propagating the insights gained at the cell level to stack and system levels, ultimately enabling a comprehensive understanding of SOC and rSOC technologies across their full operational spectrum.

4. CONCLUSION AND ANSWERS TO RESEARCH QUESTIONS

Solid Oxide Cell (SOC) technology stands today as one of the most promising candidates for high-efficiency energy conversion and long-duration energy storage, especially within the framework of renewable energy integration and decarbonization strategies. The studies presented in this thesis have addressed both the cell-level and the system-level perspectives, providing a multi-scale experimental and analytical framework aimed at deepening the knowledge on the physico-chemical phenomena and evaluating the real-world applicability of SOCs under dynamic and realistic operating conditions.

At single-cell level, the development of an innovative multisampling test bench enabled the in-operando characterization of local gas composition and temperature across the fuel electrode surface. This setup, featuring eleven sampling points and integrated gas chromatography, allowed the detection of spatial gradients in electrochemical activity and thermal distribution – phenomena that are typically overlooked in conventional inlet-outlet analyses. The results revealed a peak current density of 0.45 A/cm^2 near the inlet and a thermal gradient of approximately 4.5 °C across the cell surface, underscoring the importance of localized diagnostics in understanding degradation mechanisms and optimizing cell design. Furthermore, the integration of experimental data with a simplified electrochemical-thermal model provided predictive insights into the distribution of voltage, current density, and temperature across the cell. This modeling approach, validated against empirical measurements, offers a valuable tool for future design and optimization of SOC systems, particularly in applications involving fluctuating loads and variable fuel compositions.

The implementation of advanced localized diagnostic techniques represents a significant step forward in the understanding and optimization of SOC electrochemical behavior. Traditional characterization methods, typically based on global inlet-outlet measurements or average impedance spectra, are inevitably limited in their ability to resolve spatially distributed phenomena occurring within the cell during operation.

The introduction of multisampling setups, capable of simultaneously acquiring gas composition and temperature data at multiple points across the fuel electrode surface, enables the identification of localized gradients in reactant distribution, steam conversion, and thermal conditions. These gradients are directly correlated with variations in electrochemical activity and degradation rates, offering a more accurate and detailed picture of the internal dynamics of the cell.

Such spatially resolved data are crucial for the validation of predictive models and for the development of optimized operating strategies, particularly in systems subjected to dynamic loads or coupled with variable renewable energy sources. Moreover, the ability to detect localized anomalies – such as hot spots, fuel starvation zones, or contaminant-induced deactivation – provides a powerful tool for the design of more robust materials and architectures.

In this context, the integration of localized experimental diagnostics with simplified electrochemical-thermal models allows for the reconstruction of current density, voltage, and temperature distributions across the cell. This approach not only enhances the comprehension of degradation mechanisms but also supports the formulation of targeted mitigation strategies aimed at extending the operational lifetime and improving the overall efficiency of SOC-based systems.

The results of the present thesis confirm the scientific value of localized multisampling diagnostics while also showing opportunities for refinement through higher-resolution mapping, complementary sensing approaches and deeper integration with multi-physics models. These developments may enable diagnostic systems capable of reconstructing, with high precision, SOC internal behavior under real operating conditions.

The performance evaluation of a short-stack SOFC operating with different fuel blends – natural gas, hydrogen, and their mixtures – demonstrated the fuel flexibility and adaptability of SOC technology in the context of evolving gas grid scenarios. The experimental results, supported by system-level simulations, confirmed that while pure hydrogen yields the highest voltage and power output, blended and natural gas scenarios may offer superior efficiency due to the lower energy content of the input fuel. These findings are particularly relevant for the deployment of SOC-based Combined Heat and Power (CHP) systems in residential and industrial sectors.

The composition of the fuel supplied to Solid Oxide Cell (SOC) stacks plays a pivotal role in determining both electrochemical performance and energy conversion efficiency, particularly in stationary Combined Heat and Power (CHP) configurations. The chemical characteristics of the fuel – such as lower heating value (LHV), reforming behavior, and contaminant profile – directly influence the voltage output, power density, and thermal balance of the system.

To enable robust comparative evaluation across different operating scenarios, the following metrics are proposed:

Stack-level electrical efficiency (η_{stack}): defined as the ratio between electrical power output and chemical power input at the stack inlet, this metric isolates the electrochemical conversion performance of the SOC module.

System-level efficiency (η_{system}): incorporates auxiliary components, off-gas recirculation, and thermal recovery, providing a holistic view of the integrated CHP system.

In the context of evolving gas grid scenarios, SOC technology demonstrates strong potential for compatibility and adaptability. The high operating temperature and catalytic properties of the fuel electrode enable the processing of a wide range of fuels, including natural gas, hydrogen, biogas, and their mixtures. This fuel flexibility is particularly relevant in light of the progressive transition of gas networks towards hydrogen-enriched blends and, ultimately, pure hydrogen distribution.

Recent studies have confirmed the ability of SOC stacks to operate stably under H_2/NG mixtures, with tailored operating strategies – such as external reforming and optimized thermal integration – allowing for efficient performance across a spectrum of feedstocks. Moreover, the modularity and scalability of SOC systems support their integration into decentralized energy infrastructures, making them suitable for both current natural gas-based grids and future hydrogen-oriented networks.

In conclusion, SOC technology not only offers high efficiency and fuel flexibility in stationary CHP applications, but also aligns with the strategic direction of gas grid decarbonization, positioning itself as a viable and future-ready solution for distributed power generation.

From a system-level standpoint, the coupling of a reversible SOC (rSOC) with a domestic load and a photovoltaic (PV) plant has been experimentally demonstrated, from the rSOC point of view, as a viable solution for seasonal energy storage. The reversible operation of the cell – electrolysis mode during surplus PV generation and fuel cell mode during demand peaks – has proven to be effective in avoiding grid dependency and enhancing local energy self-consumption. The experimental campaign, lasted over 576 hours, highlighted the cell's ability to respond to rapid load variations and maintain stable operation once a new set point is imposed. Notably, the degradation trend observed during electrolysis mode, although initially pronounced, showed a progressive attenuation, suggesting a possible stabilization of the cell's internal chemistry of its materials over time.

Experimental validation of rSOC integration with photovoltaic (PV) generation and residential loads has demonstrated the feasibility of autonomous microgrids capable of achieving year-round energy self-sufficiency. The dynamic response of the cell to rapid load variations, coupled with its operational stability under fluctuating conditions, confirms its suitability for real-world deployment. In particular, the ability to shift between SOEC and SOFC modes in response to renewable availability and load demand allows rSOC systems to mitigate the temporal mismatch between generation and consumption.

In industrial contexts, rSOC systems can be scaled and coupled with larger renewable installations, offering grid balancing services, peak shaving, and enhanced energy independence. Their modular architecture and fuel flexibility further extend their applicability across diverse sectors, including manufacturing, chemical processing, and distributed generation.

To fully exploit the potential of rSOC systems, the following aspects must be addressed: (i) accurate modeling of renewable generation and load profiles, to ensure optimal sizing and operational scheduling; (ii) proper sizing of hydrogen storage and compression subsystems, to accommodate seasonal fluctuations and ensure continuity of supply; (iii) implementation of real-time control strategies, capable of managing mode transitions, minimizing degradation, and maximizing system efficiency.

A key aspect to consider for real-world deployment is the intrinsic impact of SOEC-SOFC cycling on cell durability. Repeated mode transitions can accelerate degradation through oxygen-electrode delamination, redox-driven Ni restructuring, and thermal–mechanical stresses, indicating that long-term stability must be addressed in parallel with performance optimization for rSOC-based energy storage systems.

By integrating these elements, rSOC technology can evolve into a cornerstone of future energy infrastructures, enabling efficient, flexible, and low-carbon energy storage solutions tailored to both residential and industrial needs.

Finally, from a system-level point of view, the experimental validation of the 10 kW rSOC system operated in SOEC mode confirmed its ability to reach high efficiency and operational stability, highlighting the crucial role of integrated thermal management in determining and improving global performance. These findings show the technological readiness level and effectiveness of solid oxide systems for potential coupling with renewables, supporting their transition from laboratory-scale prototypes to industrial energy conversion and storage applications.

This specific part of the work presented in this thesis contributes to bridging the gap between laboratory-scale investigations and real-world applications of SOC technology. By combining advanced experimental setups and system-level integration strategies, it lays the groundwork for the development of robust, efficient, and scalable SOC systems capable of supporting the transition towards a low-carbon energy paradigm.

For the maximization of the efficiency of reversible Solid Oxide Cell (rSOC) systems, an *ad-hoc* design approach is required. At system-level, efficiency can be significantly improved through heat management and integration, which include: (i) the implementation of multi-stage heat exchangers, (ii) high-performance insulation, (iii) internal heat recovery loops to enable the reuse of exhaust thermal energy for preheating inlet gases, thereby reducing auxiliary power consumption, (iv) superheaters for thermal integration. The evaporator, identified as a source of energy losses, plays a decisive role in determining global performance, and its integration with external steam sources – possible at industrial level – can lead to overall system efficiencies exceeding 90%.

In the 10 kW rSOC system object of study, these design strategies translate into single-pass stack-level efficiencies above 95% and system-level efficiencies ranging from 58% to 92%, depending on the degree of thermal recovery and steam integration.

These results confirm that the intrinsic electrochemical advantages and efficiency of SOC technology can be preserved at larger scales, provided that the Balance of Plant (BoP) is engineered to minimize external losses and thermal dissipation.

Author’s Specific Contributions to the Research Activities

This doctoral research is based on a combination of experimental, modeling, and system-level investigations on solid oxide cell (SOC) and reversible solid oxide cell (rSOC) technologies, carried out across multiple test stations. This section explicitly summarizes the specific contributions of the PhD candidate to the development of the methods, experimental platforms, test campaigns, data analysis, and modeling activities.

The candidate played a primary and active role in the design, implementation, execution, and interpretation of the majority of the experimental and numerical work presented in this thesis. In particular, the contributions can be summarized as follows.

With respect to the multi-sampling single-cell experimental platform, the candidate contributed to the conceptual definition of the measurement approach, participated in the design and assembly of the test bench modifications, and directly conducted the experimental campaigns. The candidate was responsible for test execution, operating condition definition, calibration procedures, data acquisition, and post-processing of the spatially resolved gas composition measurements, as well as for the interpretation of the electrochemical and transport phenomena observed. Scientific guidance, collaboration with the testing (especially the GC analysis) and supervision were provided by Dr. Davide Pumiglia and Dr. Francesca Santoni, supervisors of the research activity.

Regarding the short-stack SOFC CHP platform and gas-blend experimental campaigns, the candidate contributed to the design of the experimental methodology and assembly of the test bench. The candidate directly conducted the majority of the experiments, performed the performance analysis under different fuel compositions, and developed the data processing and efficiency evaluation procedures at both stack and system level. Scientific guidance, collaboration with the testing (especially the GC analysis) and supervision were provided by Dr. Francesca Santoni, supervisor of the research activity.

For the rSOC dynamic operation and PV-coupled scenario study, the candidate designed the experimental test strategy aimed at reproducing realistic variable load profiles derived from residential renewable energy systems. The candidate implemented the load profiles, executed the experimental campaigns under switching and variable operation, and carried out the degradation and transient performance analysis. The candidate also developed the associated modeling and simulation framework used to generate and validate the operating scenarios, except for the determination of the typical days, done with the strong collaboration of the coworker Dr. Gabriele Loreti. Scientific guidance and supervision were provided by Dr. Massimiliano Della Pietra.

Concerning the system-scale (>10 kW) rSOC installation analyzed within an international research collaboration, the candidate contributed to the performance assessment methodology, system efficiency evaluation, and thermodynamic and enthalpy flow analysis. The candidate performed the main data analysis and interpretation activities based on the experimental datasets provided within the project framework, and contributed to the definition of performance indicators and evaluation criteria. Experimental operation of the system was conducted by the host research institution, while the candidate focused on analysis, interpretation and methodological development under the supervision of Dr. Ville Saarinen, supervisor of the activity.

References

[1] Energy Institute - Statistical Review of World Energy (2025) – with major processing by Our World in Data, “energy-consumption-by-source-and-country”.

[2] 2025. https://www.2degreesinstitute.org/ 2 Degrees Institute. 2 Degrees Institute. Accessed September 21, “chart”.

[3] Z. Zhong, Y. Ding, Y. Chen, P. Liao, and Q. Chen, “Improving commercial-scale alkaline water electrolysis systems for fluctuating renewable energy: Unsteady-state thermodynamic analysis and optimization,” *Appl. Energy*, vol. 395, Oct. 2025, doi: 10.1016/j.apenergy.2025.126183.

[4] Y. Liu, W. Liu, J. Liu, H. Zhang, Z. Li, and M. Ban, “Optimal operation strategy for multi-energy systems considering renewable energy fluctuation and carbon emission,” *International Journal of Electrical Power and Energy Systems*, vol. 169, Aug. 2025, doi: 10.1016/j.ijepes.2025.110794.

[5] V. J. Reddy, N. P. Hariram, R. Maity, M. F. Ghazali, and S. Kumarasamy, “Sustainable E-Fuels: Green Hydrogen, Methanol and Ammonia for Carbon-Neutral Transportation,” Dec. 01, 2023, *Multidisciplinary Digital Publishing Institute (MDPI)*. doi: 10.3390/wevj14120349.

[6] F. R. Bianchi *et al.*, “Feasibility analysis of e-Hydrogen, e-Ammonia and e-Methanol synthesis compared with methane to fuel production,” *Fuel*, vol. 384, Mar. 2025, doi: 10.1016/j.fuel.2024.133938.

[7] C. Schnuelle, J. Thoeming, T. Wassermann, P. Thier, A. von Gleich, and S. Goessling-Reisemann, “Socio-technical-economic assessment of power-to-X: Potentials and limitations for an integration into the German energy system,” *Energy Res. Soc. Sci.*, vol. 51, pp. 187–197, May 2019, doi: 10.1016/j.erss.2019.01.017.

[8] A. Nemmour, A. Inayat, I. Janajreh, and C. Ghenai, “Green hydrogen-based E-fuels (E-methane, E-methanol, E-ammonia) to support clean energy transition: A literature review,” Sep. 01, 2023, *Elsevier Ltd*. doi: 10.1016/j.ijhydene.2023.03.240.

[9] Y. Ji *et al.*, “Development and Application of Hydrogen-Based Direct Reduction Iron Process,” Sep. 01, 2024, *Multidisciplinary Digital Publishing Institute (MDPI)*. doi: 10.3390/pr12091829.

[10] A. Hasanbeigi, C. Springer, and H. Irish, “Green H_2-DRI Steelmaking: 15 Challenges and Solutions,” 2024. [Online]. Available: www.globalefficiencyintel.com

[11] R. Khakimov, A. Moskvin, and O. Zhdaneev, “Hydrogen as a key technology for long-term & seasonal energy storage applications,” May 28, 2024, *Elsevier Ltd*. doi: 10.1016/j.ijhydene.2024.04.066.

[12] "Clean Hydrogen Observatory, Cost of Hydrogen Production, accessed September 24, 2025, https://observatory.clean-hydrogen.europa.eu/index.php/hydrogen-landscape/production-trade-and-cost/cost-hydrogen-production".

[13] "Burnertec, Hydrogen Plant Cost Analysis: SMR Vs. Electrolysis Vs. Biomass, accessed September 24, 2025, https://burnertec.com/hydrogen-plant-cost-analysis/".

[14] "Trading Economics, EU Natural Gas, accessed September 24, 2025, https://tradingeconomics.com/commodity/eu-natural-gas".

[15] James. Larminie and Andrew. Dicks, *Fuel cell systems explained*. J. Wiley, 20062003.

[16] H. Vaghari, H. Jafarizadeh-Malmiri, A. Berenjian, and N. Anarjan, "Recent advances in application of chitosan in fuel cells," *Sustainable Chemical Processes*, vol. 1, no. 1, Dec. 2013, doi: 10.1186/2043-7129-1-16.

[17] "U.S. Department of Energy, 'Comparison of Fuel Cell Technologies.' Accessed September 24, 2025. https://www.energy.gov/eere/fuelcells/comparison-fuel-cell-technologies".

[18] D. Manzo, R. Thai, H. T. Le, and G. K. Venayagamoorthy, "Fuel cell technology review: Types, economy, applications, and vehicle-to-grid scheme," Mar. 01, 2025, *Elsevier Ltd*. doi: 10.1016/j.seta.2025.104229.

[19] M. Irshad *et al.*, "A brief description of high temperature solid oxide fuel cell's operation, materials, design, fabrication technologies and performance," 2016, *MDPI AG*. doi: 10.3390/app6030075.

[20] "EcoSense World. Electrolyzer Technologies Explained: Alkaline vs. PEM vs. SOEC vs. AEM. Accessed September 25, 2025. https://www.ecosenseworld.com/blog/electrolyzer-technologies-explained-alkaline-vs-pem-vs-soec-vs-aem".

[21] "GRZ Technologies. Electrolyzer Comparison. Accessed September 25, 2025. https://grz-technologies.com/wiki/brief-electrolyzer-comparison/".

[22] "Comparison of the various kinds of electrolyzers for hydrogen production." [Online]. Available: https://www.enectiva.com/en/blog/2023/08/comparison-of-the-various-kinds-of-electrolyzers-for-hydrogen-production/?utm_source=chatgpt.com

[23] A. Marie Esposito *et al.*, "Hydrogen Shot: Water Electrolysis Technology Assessment."

[24] C. Klose *et al.*, "All-Hydrocarbon MEA for PEM Water Electrolysis Combining Low Hydrogen Crossover and High Efficiency," *Adv. Energy Mater.*, vol. 10, no. 14, Apr. 2020, doi: 10.1002/aenm.201903995.

[25] J. R. Varcoe *et al.*, "Anion-exchange membranes in electrochemical energy systems," Oct. 01, 2014, *Royal Society of Chemistry*. doi: 10.1039/c4ee01303d.

[26] K. Zhang *et al.*, "Status and perspectives of key materials for PEM electrolyzer," Dec. 01, 2022, *Tsinghua University Press*. doi: 10.26599/NRE.2022.9120032.

[27] M. E. Şahin, "An Overview of Different Water Electrolyzer Types for Hydrogen Production," Oct. 01, 2024, *Multidisciplinary Digital Publishing Institute (MDPI)*. doi: 10.3390/en17194944.

[28] J. Wang *et al.*, "Comparative experimental study of alkaline and proton exchange membrane water electrolysis for green hydrogen production," *Appl. Energy*, vol. 379, Feb. 2025, doi: 10.1016/j.apenergy.2024.124936.

[29] D. Tapiero, N. Tzabar, and L. Tartakovsky, “Performance of solid-oxide fuel cells operating with different sustainable fuel reformates,” *J. Power Sources*, vol. 611, Aug. 2024, doi: 10.1016/j.jpowsour.2024.234761.

[30] Y. Du *et al.*, “The development of solid oxide electrolysis cells: Critical materials, technologies and prospects,” Jul. 01, 2024, *Elsevier B.V.* doi: 10.1016/j.jpowsour.2024.234608.

[31] cubhash cinghal and K. Kendal, “High Temperature Solid Oxide Fuel Cells Fun dam en tals.”

[32] “Fuel Cell Handbook (Seventh Edition),” 2004.

[33] M. A. Laguna-Bercero, “Recent advances in high temperature electrolysis using solid oxide fuel cells: A review,” Apr. 01, 2012. doi: 10.1016/j.jpowsour.2011.12.019.

[34] J. C. Ruiz-Morales, D. Marrero-López, J. Canales-Vázquez, and J. T. S. Irvine, “Symmetric and reversible solid oxide fuel cells,” Nov. 21, 2011. doi: 10.1039/c1ra00284h.

[35] J. Stempien, S. Chan, J. Pawel Stempien, Q. Sun, and S. Hwa Chan, “Solid Oxide Electrolyzer Cell Modeling: A Review Journal of Power Technologies 93 (4) (2013) 216-246 Solid Oxide Electrolyzer Cell Modeling: A Review,” 2016. [Online]. Available: https://www.researchgate.net/publication/268461818

[36] W. Chanpeng and Y. Khunatorn, “The effect of the input load current changed to a 1.2 kW PEMFC performance,” in *Energy Procedia*, Elsevier Ltd, 2011, pp. 316–325. doi: 10.1016/j.egypro.2011.09.034.

[37] Y. Yang, J. Lei, X. Huang, Z. Liao, Y. Liu, and Z. Tu, “Recent Development in Reversible Solid Oxide Fuel Cells: Theory, Integration and Prospective,” Mar. 15, 2024, *John Wiley and Sons Inc*. doi: 10.1002/celc.202300593.

[38] S. P. Jiang and S. H. Chan, “A review of anode materials development in solid oxide fuel cells,” *J. Mater. Sci.*, vol. 39, no. 14, pp. 4405–4439, Jul. 2004, doi: 10.1023/b:jmsc.0000034135.52164.6b.

[39] M. V. Yusenko *et al.*, “Performance of Single-Chamber Solid Oxide Fuel Cells Based on Ni and Ni–Cu Alloy Anodes and Fed with a Methane–Air Mixture,” *Kinetics and Catalysis*, vol. 63, no. 1, pp. 123–128, Feb. 2022, doi: 10.1134/S0023158422010116.

[40] A. Azim Jais *et al.*, “Performance of Ni/10Sc1CeSZ anode synthesized by glycine nitrate process assisted by microwave heating in a solid oxide fuel cell fueled with hydrogen or methane”, doi: 10.1007/s10008-020-04512-6/Published.

[41] M. Mogensen, T. Lindegaard, U. R. Hansen, and G. Mogensen, “Physical Properties of Mixed Conductor Solid Oxide Fuel Cell Anodes of Doped CeO2,” *J. Electrochem. Soc.*, vol. 141, no. 8, pp. 2122–2128, Aug. 1994, doi: 10.1149/1.2055072.

[42] P. H. Tu *et al.*, “Paper-structured catalyst containing CeO2–Ni flowers for dry reforming of methane,” *Int. J. Hydrogen Energy*, vol. 45, no. 36, pp. 18363–18375, Jul. 2020, doi: 10.1016/j.ijhydene.2019.10.247.

[43] N. Zhang *et al.*, “Design of core-shell structured YSZ@Cu cermet powders with thermal conductivity anisotropy by electroless deposition,” *Ceram. Int.*, vol. 46, no. 11, pp. 18832–18841, Aug. 2020, doi: 10.1016/j.ceramint.2020.04.201.

[44] Y. C. Lin and W. C. J. Wei, “Porous Cu–Ni-YSZ cermets using CH4 fuel for SOFC,” *Int. J. Hydrogen Energy*, vol. 45, no. 46, pp. 24253–24262, Sep. 2020, doi: 10.1016/j.ijhydene.2020.05.281.

[45] C. Sanna, P. Costamagna, and P. Holtappels, “Electrochemical Impedance Spectroscopy of Core-Shell Nanofiber Cathodes, with Ce0.9Gd0.1O1.95 (Core) and Cu-Doped La0.6Sr0.4MnO3 (Shell), for Application in Solid Oxide Fuel Cells,” *ChemElectroChem*, vol. 10, no. 14, Jul. 2023, doi: 10.1002/celc.202300101.

[46] L. Shu, J. Sunarso, S. S. Hashim, J. Mao, W. Zhou, and F. Liang, “Advanced perovskite anodes for solid oxide fuel cells: A review,” Nov. 29, 2019, *Elsevier Ltd*. doi: 10.1016/j.ijhydene.2019.09.220.

[47] Z. Zakaria and S. K. Kamarudin, “Advanced modification of scandia-stabilized zirconia electrolytes for solid oxide fuel cells application—A review,” Mar. 25, 2021, *John Wiley and Sons Ltd*. doi: 10.1002/er.6206.

[48] T. Cui *et al.*, “Identification of Electrode Process in Large-Size Solid Oxide Fuel Cell,” *Chinese Journal of Inorganic Chemistry*, vol. 38, no. 8, 2022, doi: 10.3866/PKU.WHXB202011009.

[49] “Peng, S. (2023). Solid Oxide Electrolysis. In: Electrochemical Hydrogen Production from Water Splitting. Springer, Singapore. https://doi.org/10.1007/978-981-99-4468-2_6”.

[50] N. Danilov, J. Lyagaeva, G. Vdovin, and D. Medvedev, “Multifactor performance analysis of reversible solid oxide cells based on proton-conducting electrolytes,” *Appl. Energy*, vol. 237, pp. 924–934, Mar. 2019, doi: 10.1016/j.apenergy.2019.01.054.

[51] G. Liu *et al.*, “Modeling and control-oriented thermal safety analysis for mode switching process of reversible solid oxide cell system,” *Energy Convers. Manag.*, vol. 255, Mar. 2022, doi: 10.1016/j.enconman.2022.115318.

[52] Y. Sun *et al.*, “Dynamic simulation of a reversible solid oxide cell system for efficient H2 production and power generation,” *Energy*, vol. 263, Jan. 2023, doi: 10.1016/j.energy.2022.125725.

[53] Z. Ouyang, Y. Komatsu, A. Sciazko, J. Onishi, K. Nishimura, and N. Shikazono, “Operando observations of active three phase boundary of patterned nickel - Yttria stabilized zirconia electrode in solid oxide cell,” *J. Power Sources*, vol. 529, May 2022, doi: 10.1016/j.jpowsour.2022.231228.

[54] G. Zheng *et al.*, “A promising Bi-doped La0.8Sr0.2Ni0.2Fe0.8O3-δ oxygen electrode for reversible solid oxide cells,” *Int. J. Hydrogen Energy*, vol. 48, no. 34, pp. 12571–12580, Apr. 2023, doi: 10.1016/j.ijhydene.2022.12.195.

[55] M. B. Hanif *et al.*, “Proton-conducting solid oxide electrolysis cells: Relationship of composition-structure-property, their challenges, and prospects,” Jun. 07, 2023, *Cell Press*. doi: 10.1016/j.matt.2023.04.013.

[56] M. Mogensen, N. M. Sammes, and G. A. Tompsett, “Physical, chemical and electrochemical properties of pure and doped ceria,” 2000. [Online]. Available: www.elsevier.com/locate/ssi

[57] C. Su *et al.*, “Effects of a YSZ porous layer between electrolyte and oxygen electrode in solid oxide electrolysis cells on the electrochemical performance and stability,” *Int. J. Hydrogen Energy*, vol. 44, no. 29, pp. 14493–14499, Jun. 2019, doi: 10.1016/j.ijhydene.2019.04.092.

[58] T. Chen *et al.*, “Application of CuNi–CeO2 fuel electrode in oxygen electrode supported reversible solid oxide cell,” *Int. J. Hydrogen Energy*, vol. 48, no. 26, pp. 9565–9573, Mar. 2023, doi: 10.1016/j.ijhydene.2022.11.236.

[59] H. J. Men, N. Tian, Y. M. Qu, M. Wang, S. Zhao, and J. Yu, “Improved performance of a lanthanum strontium manganite–based oxygen electrode for an intermediate-temperature solid oxide

electrolysis cell realized via ionic conduction enhancement," *Ceram. Int.*, vol. 45, no. 6, pp. 7945–7949, Apr. 2019, doi: 10.1016/j.ceramint.2019.01.107.

[60] Y. Tan, S. Gao, C. Y. Xiong, and B. Chi, "Nano-structured LSM-YSZ refined with PdO/ZrO2 oxygen electrode for intermediate temperature reversible solid oxide cells," *Int. J. Hydrogen Energy*, vol. 45, no. 38, pp. 19823–19830, Jul. 2020, doi: 10.1016/j.ijhydene.2020.05.116.

[61] Z. Zhao, S. Tang, Z. Liu, L. Cao, M. Cheng, and Z. Shao, "Efficient and stable heterostructured air electrode for solid oxide steam electrolysis," *Int. J. Hydrogen Energy*, vol. 48, no. 15, pp. 5764–5773, Feb. 2023, doi: 10.1016/j.ijhydene.2022.11.117.

[62] C. Chen, Z. Wang, X. Miao, C. Sun, X. Ye, and Z. Wen, "Cycling performance and interface stability research of tubular protonic reversible solid oxide cells with air electrodes by different manufacturing processes," *Electrochem. commun.*, vol. 151, Jun. 2023, doi: 10.1016/j.elecom.2023.107507.

[63] X. Sun, B. R. Sudireddy, X. Tong, M. Chen, K. Brodersen, and A. Hauch, "Optimization and Durability of Reversible Solid Oxide Cells," *ECS Trans.*, vol. 91, no. 1, pp. 2631–2639, Jul. 2019, doi: 10.1149/09101.2631ecst.

[64] S. U. Rehman *et al.*, "Designing the nano-scale architecture of the air electrode for high-performance and robust reversible solid oxide cells," *Appl. Catal. B*, vol. 333, Sep. 2023, doi: 10.1016/j.apcatb.2023.122784.

[65] X. Tong, S. Ovtar, K. Brodersen, P. V. Hendriksen, and M. Chen, "Large-area solid oxide cells with La0.6Sr0.4CoO3-δ infiltrated oxygen electrodes for electricity generation and hydrogen production," *J. Power Sources*, vol. 451, Mar. 2020, doi: 10.1016/j.jpowsour.2020.227742.

[66] N. Q. Minh, "Solid oxide fuel cell technology - Features and applications," Oct. 29, 2004. doi: 10.1016/j.ssi.2004.07.042.

[67] "Fergus, Jeffrey W. 'Materials Challenges for Solid-Oxide Fuel Cells.' Journal of the Minerals, Metals & Materials Society (JOM) 59, no. 9 (2007): 56–62. https://doi.org/10.1007/s11837-007-0102-1".

[68] B. Wei, K. Chen, L. Zhao, Z. Lü, and S. P. Jiang, "Chromium deposition and poisoning at la0.6Sr0.4Co0.2Fe0.8O3-δ oxygen electrodes of solid oxide electrolysis cells," *Physical Chemistry Chemical Physics*, vol. 17, no. 3, pp. 1601–1609, Jan. 2015, doi: 10.1039/c4cp05110f.

[69] B. Talic, "Metallic Interconnects for Solid Oxide Fuel Cells High Temperature Corrosion and Protective Spinel Coatings,"

[70] "DOITPoMS. 'High Temperature Solid Oxide Fuel Cells.' University of Cambridge – Department of Materials Science & Metallurgy, accessed October 23, 2025. https://www.doitpoms.ac.uk/tlplib/fuel-cells/high_temp_sofc.php".

[71] S. J. McPhail *et al.*, "Addressing planar solid oxide cell degradation mechanisms: A critical review of selected components," Oct. 01, 2022, *John Wiley and Sons Inc*. doi: 10.1002/elsa.202100024.

[72] X. Shao, R. A. Budiman, T. Sato, M. Yamaguchi, T. Kawada, and K. Yashiro, "Review of factors affecting the performance degradation of Ni-YSZ fuel electrodes in solid oxide electrolyzer cells," Jul. 30, 2024, *Elsevier B.V.* doi: 10.1016/j.jpowsour.2024.234651.

[73] Y. Wang, W. Li, L. Ma, W. Li, and X. Liu, "Degradation of solid oxide electrolysis cells: Phenomena, mechanisms, and emerging mitigation strategies—A review," Oct. 15, 2020, *Chinese Society of Metals*. doi: 10.1016/j.jmst.2019.07.026.

[74] G. Schiller, A. Ansar, M. Lang, and O. Patz, “High temperature water electrolysis using metal supported solid oxide electrolyser cells (SOEC),” *J. Appl. Electrochem.*, vol. 39, no. 2, pp. 293–301, Feb. 2009, doi: 10.1007/s10800-008-9672-6.

[75] P. Hjalmarsson, X. Sun, Y. L. Liu, and M. Chen, “Durability of high performance Ni-yttria stabilized zirconia supported solid oxide electrolysis cells at high current density,” *J. Power Sources*, vol. 262, pp. 316–322, Sep. 2014, doi: 10.1016/j.jpowsour.2014.03.133.

[76] R. P. W. J. Struis, T. J. Schildhauer, I. Czekaj, M. Janousch, S. M. A. Biollaz, and C. Ludwig, “Sulphur poisoning of Ni catalysts in the SNG production from biomass: A TPO/XPS/XAS study,” *Appl. Catal. A Gen.*, vol. 362, no. 1–2, pp. 121–128, Jun. 2009, doi: 10.1016/j.apcata.2009.04.030.

[77] R. Wang Saint-Gobain, “Chromium Poisoning of Cathode in Solid Oxide Fuel Cells: Mechanisms and Mitigation Strategies.” [Online]. Available: https://www.researchgate.net/publication/325464626

[78] A. Hauch *et al.*, “Recent advances in solid oxide cell technology for electrolysis,” *Science (1979).*, vol. 370, no. 6513, Oct. 2020, doi: 10.1126/science.aba6118.

[79] O. Posdziech, K. Schwarze, and J. Brabandt, “Efficient hydrogen production for industry and electricity storage via high-temperature electrolysis,” *Int. J. Hydrogen Energy*, pp. 19089–19101, Jul. 2019, doi: 10.1016/j.ijhydene.2018.05.169.

[80] M. C. Williams, S. D. Vora, and G. Jesionowski, “Worldwide Status of Solid Oxide Fuel Cell Technology,” *ECS Trans.*, vol. 96, no. 1, pp. 1–10, Jan. 2020, doi: 10.1149/09601.0001ecst.

[81] J. Mougin, “MULTIPLHY Multimegawatt high-temperature electrolyser to generate green hydrogen for production of high-quality biofuels.” [Online]. Available: https://multiplhy-project.eu

[82] X. Zhang *et al.*, “Thermal Stress in Full-Size Solid Oxide Fuel Cell Stacks by Multi-Physics Modeling,” *Energies (Basel).*, vol. 17, no. 9, May 2024, doi: 10.3390/en17092025.

[83] Y. Kim, K. Lim, H. Salihi, S. Heo, and H. Ju, “The Effects of Stack Configurations on the Thermal Management Capabilities of Solid Oxide Electrolysis Cells,” *Energies (Basel).*, vol. 17, no. 1, Jan. 2024, doi: 10.3390/en17010125.

[84] H. Choi, J. Lim, W. Lee, and J. Hong, “The effect of internal manifold configuration on thermal and electrochemical distributions in commercial scale solid oxide fuel cell stacks fueled by hydrogen and hydrocarbon,” *J. Power Sources*, vol. 645, Jul. 2025, doi: 10.1016/j.jpowsour.2025.237148.

[85] S. E. Wolf *et al.*, “Solid oxide electrolysis cells - current material development and industrial application,” Jul. 10, 2023, *Royal Society of Chemistry*. doi: 10.1039/d3ta02161k.

[86] S. Pirou *et al.*, “Production of a monolithic fuel cell stack with high power density,” *Nat. Commun.*, vol. 13, no. 1, Dec. 2022, doi: 10.1038/s41467-022-28970-w.

[87] M. Lang *et al.*, “Analysis of electrochemical degradation phenomena of a 60-cell SOC stack operated in reversible SOFC/SOEC cycling mode,” *Appl. Energy*, vol. 386, May 2025, doi: 10.1016/j.apenergy.2025.125565.

[88] Q. Ma *et al.*, “Electrochemical Performances of a Solid Oxide Electrolysis Short Stack Under Multiple Steady-State and Cycling Operating Conditions,” *Inorganics (Basel).*, vol. 12, no. 11, Nov. 2024, doi: 10.3390/inorganics12110288.

[89] J. Beyrami, R. Nogueira Nakashima, A. Nemati, and H. Lund Frandsen, "Degradation modeling in solid oxide electrolysis systems: A comparative analysis of operation modes," *Energy Conversion and Management: X*, vol. 23, Jul. 2024, doi: 10.1016/j.ecmx.2024.100653.

[90] F. Alenazey *et al.*, "Degradation Behaviors of Solid Oxide Fuel Cell Stacks in Steady-State and Cycling Conditions," *Energy and Fuels*, vol. 34, no. 11, pp. 14864–14873, Nov. 2020, doi: 10.1021/acs.energyfuels.0c02920.

[91] L. Blum *et al.*, "Solid Oxide Fuel Cell, Stack and System Development Status at Forschungszentrum Jülich," *ECS Trans.*, vol. 68, no. 1, pp. 157–169, Jun. 2015, doi: 10.1149/06801.0157ecst.

[92] Q. Fang, L. Blum, and N. H. Menzler, "Performance and Degradation of Solid Oxide Electrolysis Cells in Stack," *J. Electrochem. Soc.*, vol. 162, no. 8, pp. F907–F912, 2015, doi: 10.1149/2.0941508jes.

[93] J. Beyrami, R. N. Nakashima, A. Nemati, and H. L. Frandsen, "Lifetime and performance of solid oxide electrolysis stacks and systems under different operation modes and conditions," *Int. J. Hydrogen Energy*, vol. 102, pp. 980–995, Feb. 2025, doi: 10.1016/j.ijhydene.2025.01.028.

[94] T. Skafte, ; Løye, J. ; Hjelm, P. ; Blennow, and C. R. Graves, *General rights Quantitative review of degradation and lifetime of solid oxide cells and stacks*. 2025. [Online]. Available: www.EFCF.com/Lib

[95] X. Zhang, J. E. O'Brien, R. C. O'Brien, J. J. Hartvigsen, G. Tao, and G. K. Housley, "Improved durability of SOEC stacks for high temperature electrolysis," *Int. J. Hydrogen Energy*, vol. 38, no. 1, pp. 20–28, Jan. 2013, doi: 10.1016/j.ijhydene.2012.09.176.

[96] F. Tietz, D. Sebold, A. Brisse, and J. Schefold, "Degradation phenomena in a solid oxide electrolysis cell after 9000 h of operation," *J. Power Sources*, vol. 223, pp. 129–135, Feb. 2013, doi: 10.1016/j.jpowsour.2012.09.061.

[97] B. Königshofer *et al.*, "Development of test protocols for solid oxide electrolysis cells operated under accelerated degradation conditions," *J. Power Sources*, vol. 497, Jun. 2021, doi: 10.1016/j.jpowsour.2021.229875.

[98] V. N. Nguyen, Q. Fang, U. Packbier, and L. Blum, "Long-term tests of a Jülich planar short stack with reversible solid oxide cells in both fuel cell and electrolysis modes," *Int. J. Hydrogen Energy*, vol. 38, no. 11, pp. 4281–4290, Apr. 2013, doi: 10.1016/j.ijhydene.2013.01.192.

[99] M. S. Sohal, A. V Virkar, S. N. Rashkeev, and M. V Glazoff, "Modeling Degradation in Solid Oxide Electrolysis Cells," 2010. [Online]. Available: http://www.inl.gov

[100] G. Ju and K. Reifsnider, "IMECE2006-13874 DRAFT Infrared thermography and thermoelectrical study of a solid oxide fuel cell," 2006. [Online]. Available: https://proceedings.asmedigitalcollection.asme.org

[101] X. Zhang, J. E. O'Brien, R. C. O'Brien, and G. K. Housley, "Durability evaluation of reversible solid oxide cells," *J. Power Sources*, vol. 242, pp. 566–574, 2013, doi: 10.1016/j.jpowsour.2013.05.134.

[102] S. E. Wolf, V. Vibhu, E. Tröster, I. C. Vinke, R. A. Eichel, and L. G. J. de Haart, "Steam Electrolysis vs. Co-Electrolysis: Mechanistic Studies of Long-Term Solid Oxide Electrolysis Cells," *Energies (Basel).*, vol. 15, no. 15, Aug. 2022, doi: 10.3390/en15155449.

[103] X. Tong, S. Ovtar, K. Brodersen, P. V. Hendriksen, and M. Chen, "A 4 × 4 cm2 Nanoengineered Solid Oxide Electrolysis Cell for Efficient and Durable Hydrogen Production," *ACS Appl. Mater. Interfaces*, vol. 11, no. 29, pp. 25996–26004, Jul. 2019, doi: 10.1021/acsami.9b07749.

[104] J. Schefold, A. Brisse, and H. Poepke, “23,000 h steam electrolysis with an electrolyte supported solid oxide cell,” *Int. J. Hydrogen Energy*, vol. 42, no. 19, pp. 13415–13426, May 2017, doi: 10.1016/j.ijhydene.2017.01.072.

[105] H. Chen, J. Wang, and X. Xu, “Parametric Study of Operating Conditions on Performances of a Solid Oxide Electrolysis Cell,” *Journal of Thermal Science*, vol. 32, no. 6, pp. 1973–1988, Nov. 2023, doi: 10.1007/s11630-023-1772-4.

[106] Q. Hou, C. Guan, G. Xiao, J. Q. Wang, and Z. Zhu, “Effect of oxygen partial pressure on solid oxide electrolysis cells,” *Wuli Huaxue Xuebao/ Acta Physico - Chimica Sinica*, vol. 35, no. 3, pp. 284–291, 2019, doi: 10.3866/PKU.WHXB201804171.

[107] “Thermal-fluid and Electrochemical Modeling and Performance Study of a Planar Solid Oxide Electrolysis Cell: Analysis on SOEC Resistances, Size, and Inlet Flow Conditions.” [Online]. Available: www.anl.gov.

[108] Z. Xu, X. Zhang, G. Li, G. Xiao, and J. Q. Wang, “Comparative performance investigation of different gas flow configurations for a planar solid oxide electrolyzer cell,” *Int. J. Hydrogen Energy*, vol. 42, no. 16, pp. 10785–10801, Apr. 2017, doi: 10.1016/j.ijhydene.2017.02.097.

[109] Y. Xu, J. Zhang, and Z. Tu, “Numerical simulation of flow channel geometries optimization for the planar solid oxide electrolysis cell,” *Int. J. Hydrogen Energy*, vol. 52, pp. 288–301, Jan. 2024, doi: 10.1016/j.ijhydene.2023.07.242.

[110] C. Schluckner, V. Subotić, S. Preißl, and C. Hochenauer, “Numerical analysis of flow configurations and electrical contact positions in SOFC single cells and their impact on local effects,” *Int. J. Hydrogen Energy*, vol. 44, no. 3, pp. 1877–1895, Jan. 2019, doi: 10.1016/j.ijhydene.2018.11.132.

[111] G. Schiller, W. G. Bessler, K. A. Friedrich, S. Gewies, and C. Willich, “Spatially Resolved Electrochemical Performance in a Segmented Planar SOFC,” *ECS Trans.*, vol. 17, no. 1, pp. 79–87, May 2009, doi: 10.1149/1.3142737.

[112] Y. Wu, H. Liu, Y. Wang, L. An, and X. Xu, “Spatially resolved electrochemical performance and temperature distribution of a segmented solid oxide fuel cell under various hydrogen dilution ratios and electrical loadings,” *J. Power Sources*, vol. 536, Jul. 2022, doi: 10.1016/j.jpowsour.2022.231477.

[113] M. W. Kim, M. J. Son, H. Park, J. Y. Park, and H. T. Lim, “Experimental Investigation of In-plane Performance Variation on Anode Supported Solid Oxide Fuel Cells Using Segmented Cathodes and Reference Electrodes,” *Fuel Cells*, vol. 20, no. 2, pp. 212–219, Apr. 2020, doi: 10.1002/fuce.201900214.

[114] M. Lang, C. Bohn, M. Henke, G. Schiller, C. Willich, and F. Hauler, “Understanding the Current-Voltage Behavior of High Temperature Solid Oxide Fuel Cell Stacks,” *J. Electrochem. Soc.*, vol. 164, no. 13, pp. F1460–F1470, 2017, doi: 10.1149/2.1541713jes.

[115] H. Moussaoui, A. Wesoly, S. Diethelm, Z. Wuillemin, D. Montinaro, and J. Van herle, “Local electrochemical and thermal investigation of a segmented reversible solid oxide fuel cell and electrolyzer,” *Electrochim. Acta*, vol. 475, Jan. 2024, doi: 10.1016/j.electacta.2023.143627.

[116] B. Königshofer, M. Höber, N. H. Menzler, H. Schröttner, C. Hochenauer, and V. Subotić, “Experimental investigation of segmented SOECs: Locally-resolved impedance and degradation characteristics,” *Int. J. Hydrogen Energy*, vol. 48, no. 10, pp. 3740–3758, Feb. 2023, doi: 10.1016/j.ijhydene.2022.10.265.

[117] F. Santoni *et al.*, “In-situ study of the gas-phase composition and temperature of an intermediate-temperature solid oxide fuel cell anode surface fed by reformate natural gas,” *J. Power Sources*, vol. 370, pp. 36–44, Dec. 2017, doi: 10.1016/j.jpowsour.2017.09.078.

[118] D. Pumiglia *et al.*, “SOFC Anode Process Characterization by Means of a Spot-Sampling Set-up for in-Operando Gas Analysis,” *ECS Trans.*, vol. 75, no. 49, pp. 1–8, Jan. 2017, doi: 10.1149/07549.0001ecst.

[119] B. Conti, B. Bosio, S. J. McPhail, F. Santoni, D. Pumiglia, and E. Arato, “A 2-D model for intermediate temperature solid oxide fuel cells preliminarily validated on local values,” *Catalysts*, vol. 9, no. 1, Jan. 2019, doi: 10.3390/catal9010036.

[120] A. Weber, “Fuel flexibility of solid oxide fuel cells,” *Fuel Cells*, vol. 21, no. 5, pp. 440–452, Oct. 2021, doi: 10.1002/fuce.202100037.

[121] K. Eguchi, H. Kojo, T. Takeguchi, R. Kikuchi, and K. Sasaki, “Fuel flexibility in power generation by solid oxide fuel cells.” [Online]. Available: www.elsevier.com/locate/ssi

[122] Q. Xu *et al.*, “A comprehensive review of solid oxide fuel cells operating on various promising alternative fuels,” Feb. 01, 2022, *Elsevier Ltd*. doi: 10.1016/j.enconman.2021.115175.

[123] J. Sánchez-Laínez *et al.*, “Enabling the injection of hydrogen in high-pressure gas grids: Investigation of the impact on materials and equipment,” *Int. J. Hydrogen Energy*, vol. 52, pp. 1007–1018, Jan. 2024, doi: 10.1016/j.ijhydene.2023.05.220.

[124] Z. Chen, D. Yang, and H. Bian, “Peridynamic modeling of crack propagation driven by hydrogen embrittlement,” *Eng. Fract. Mech.*, vol. 293, Dec. 2023, doi: 10.1016/j.engfracmech.2023.109687.

[125] M. Sofian, M. B. Haq, D. Al Shehri, M. M. Rahman, and N. S. Muhammed, “A review on hydrogen blending in gas network: Insight into safety, corrosion, embrittlement, coatings and liners, and bibliometric analysis,” Mar. 22, 2024, *Elsevier Ltd*. doi: 10.1016/j.ijhydene.2024.02.166.

[126] Z. Chen, D. Yang, and H. Bian, “Peridynamic modeling of crack propagation driven by hydrogen embrittlement,” *Eng. Fract. Mech.*, vol. 293, Dec. 2023, doi: 10.1016/j.engfracmech.2023.109687.

[127] S. A. Shirazi *et al.*, “Erosion-Corrosion in Oil and Gas Pipelines,” in *Oil and Gas Pipelines: Integrity and Safety Handbook*, wiley, 2015, pp. 399–422. doi: 10.1002/9781119019213.ch28.

[128] A. Groysman, “Corrosion problems and solutions in oil, gas, refining and petrochemical industry,” *Koroze a Ochrana Materialu*, vol. 61, no. 3, pp. 100–117, Jul. 2017, doi: 10.1515/kom-2017-0013.

[129] Entsog, “Decarbonising the gas value chain: Challenges, solutions and recommendations.”

[130] L. Jin, A. Monforti Ferrario, V. Cigolotti, and G. Comodi, “Evaluation of the impact of green hydrogen blending scenarios in the Italian gas network: Optimal design and dynamic simulation of operation strategies,” *Renewable and Sustainable Energy Transition*, vol. 2, Aug. 2022, doi: 10.1016/j.rset.2022.100022.

[131] S. J. McPhail, A. Aarva, H. Devianto, R. Bove, and A. Moreno, “SOFC and MCFC: Commonalities and opportunities for integrated research,” in *International Journal of Hydrogen Energy*, Aug. 2011, pp. 10337–10345. doi: 10.1016/j.ijhydene.2010.09.071.

[132] K. H. Ng, H. A. Rahman, and M. R. Somalu, “WITHDRAWN: Review: Enhancement of composite anode materials for low-temperature solid oxide fuels,” *Int. J. Hydrogen Energy*, Feb. 2018, doi: 10.1016/j.ijhydene.2018.01.073.

[133] S. Ma, G. Loreti, L. Wang, F. Maréchal, J. Van herle, and C. Dong, “Comparison and optimization of different fuel processing options for biogas-fed solid-oxide fuel cell plants,” *Int. J. Hydrogen Energy*, vol. 47, no. 1, pp. 551–564, Jan. 2022, doi: 10.1016/j.ijhydene.2021.10.025.

[134] H. Zhu and R. J. Kee, “Thermodynamics of SOFC efficiency and fuel utilization as functions of fuel mixtures and operating conditions,” *J. Power Sources*, vol. 161, no. 2, pp. 957–964, Oct. 2006, doi: 10.1016/j.jpowsour.2006.05.006.

[135] V. Liso, M. P. Nielsen, and S. K. Kær, “Influence of anodic gas recirculation on solid oxide fuel cells in a micro combined heat and power system,” *Sustainable Energy Technologies and Assessments*, vol. 8, pp. 99–108, 2014, doi: 10.1016/j.seta.2014.08.002.

[136] tanatpon, “Net Zero Roadmap A Global Pathway to Keep the 1.5 °C Goal in Reach,” 2023. [Online]. Available: www.iea.org/t&c/

[137] S. Y. Zheng, K. Liu, Y. Li, B. Li, and A. Usman, “How does hydrogen energy technology help to achieve carbon neutrality targets?,” *Renew. Energy*, vol. 227, Jun. 2024, doi: 10.1016/j.renene.2024.120465.

[138] A. Hauch, A. Ploner, S. Pylypko, G. Cubizolles, and J. Mougin, “Test and characterization of reversible solid oxide cells and stacks for innovative renewable energy storage,” *Fuel Cells*, vol. 21, no. 5, pp. 467–476, Oct. 2021, doi: 10.1002/fuce.202100046.

[139] D. A. Elalfy, E. Gouda, M. F. Kotb, V. Bureš, and B. E. Sedhom, “Comprehensive review of energy storage systems technologies, objectives, challenges, and future trends,” Jul. 01, 2024, *Elsevier Ltd*. doi: 10.1016/j.esr.2024.101482.

[140] F. Nadeem, S. M. S. Hussain, P. K. Tiwari, A. K. Goswami, and T. S. Ustun, “Comparative review of energy storage systems, their roles, and impacts on future power systems,” 2019, *Institute of Electrical and Electronics Engineers Inc.* doi: 10.1109/ACCESS.2018.2888497.

[141] S. Ould Amrouche, D. Rekioua, T. Rekioua, and S. Bacha, “Overview of energy storage in renewable energy systems,” *Int. J. Hydrogen Energy*, vol. 41, no. 45, pp. 20914–20927, Dec. 2016, doi: 10.1016/j.ijhydene.2016.06.243.

[142] E. Hossain, H. M. R. Faruque, M. S. H. Sunny, N. Mohammad, and N. Nawar, “A comprehensive review on energy storage systems: Types, comparison, current scenario, applications, barriers, and potential solutions, policies, and future prospects,” Jul. 01, 2020, *MDPI AG*. doi: 10.3390/en13143651.

[143] C. Zhang, C. Chen, D. Streimikiene, and T. Balezentis, “Intuitionistic fuzzy MULTIMOORA approach for multi-criteria assessment of the energy storage technologies,” *Applied Soft Computing Journal*, vol. 79, pp. 410–423, Jun. 2019, doi: 10.1016/j.asoc.2019.04.008.

[144] International Energy Agency (IEA), “Global installed energy storage capacity by scenario, 2023 and 2030.” Accessed: Apr. 24, 2025. [Online]. Available: https://www.iea.org/data-and-statistics/charts/global-installed-energy-storage-capacity-by-scenario-2023-and-2030

[145] S. Sabihuddin, A. E. Kiprakis, and M. Mueller, “A numerical and graphical review of energy storage technologies,” 2015, *MDPI AG*. doi: 10.3390/en8010172.

[146] M. Götz *et al.*, “Renewable Power-to-Gas: A technological and economic review,” Jan. 01, 2016, *Elsevier Ltd*. doi: 10.1016/j.renene.2015.07.066.

[147] M. Bailera, P. Lisbona, L. M. Romeo, and S. Espatolero, “Power to Gas projects review: Lab, pilot and demo plants for storing renewable energy and CO2,” Mar. 01, 2017, *Elsevier Ltd*. doi: 10.1016/j.rser.2016.11.130.

[148] D. Ferrero, A. Lanzini, P. Leone, and M. Santarelli, “Reversible operation of solid oxide cells under electrolysis and fuel cell modes: Experimental study and model validation,” *Chemical Engineering Journal*, vol. 274, pp. 143–155, Aug. 2015, doi: 10.1016/j.cej.2015.03.096.

[149] H. del Pozo Gonzalez *et al.*, “Power transition cycles of reversible solid oxide cells and its impacts on microgrids,” *Appl. Energy*, vol. 352, Dec. 2023, doi: 10.1016/j.apenergy.2023.121887.

[150] J. Hong, J. Grimes, D. Cox, and S. A. Barnett, “Life testing of 10 cm × 10 cm fuel-electrode-supported solid oxide cells in reversible operation,” *Appl. Energy*, vol. 355, Feb. 2024, doi: 10.1016/j.apenergy.2023.122275.

[151] S. H. Jensen *et al.*, “Large-scale electricity storage utilizing reversible solid oxide cells combined with underground storage of CO2 and CH4,” *Energy Environ. Sci.*, vol. 8, no. 8, pp. 2471–2479, 2015, doi: 10.1039/c5ee01485a.

[152] A. V. Virkar, “Mechanism of oxygen electrode delamination in solid oxide electrolyzer cells,” *Int. J. Hydrogen Energy*, vol. 35, no. 18, pp. 9527–9543, Sep. 2010, doi: 10.1016/j.ijhydene.2010.06.058.

[153] O. Schmidt, A. Gambhir, I. Staffell, A. Hawkes, J. Nelson, and S. Few, “Future cost and performance of water electrolysis: An expert elicitation study,” *Int. J. Hydrogen Energy*, vol. 42, no. 52, pp. 30470–30492, Dec. 2017, doi: 10.1016/j.ijhydene.2017.10.045.

[154] T. D. Hutty, S. Dong, and S. Brown, “Suitability of energy storage with reversible solid oxide cells for microgrid applications,” *Energy Convers. Manag.*, vol. 226, Dec. 2020, doi: 10.1016/j.enconman.2020.113499.

[155] G. Flis, “Solid Oxide Electrolysis: A Technology Status Assessment.”

[156] B. D. James and J. H. Prosser, “HTE Stack Manufacturing Cost and Analysis,” 2022.

[157] M. B. Mogensen *et al.*, “Ni migration in solid oxide cell electrodes: Review and revised hypothesis,” *Fuel Cells*, vol. 21, no. 5, pp. 415–429, Oct. 2021, doi: 10.1002/fuce.202100072.

[158] Q. Liu, H. Wang, D. Kennouche, C. Riscoe, D. Butts, and S. A. Barnett, “Effect of Reversing-Current Operation on the Structure and Electrochemical Performance Evolution of Ni-YSZ Fuel Electrodes,” *J. Electrochem. Soc.*, vol. 165, no. 10, pp. F870–F875, 2018, doi: 10.1149/2.1231810jes.

[159] C. Graves, “Reversing and Repairing Microstructure Degradation in Solid Oxide Cells during Operation,” *ECS Trans.*, vol. 57, no. 1, pp. 3127–3136, Oct. 2013, doi: 10.1149/05701.3127ecst.

[160] S. J. Heo, J. Hong, A. Aphale, B. Hu, and P. Singh, “ Chromium Poisoning of La 1-x Sr x MnO 3±δ Cathodes and Electrochemical Validation of Chromium Getters in Intermediate Temperature-Solid Oxide Fuel Cells ,” *J. Electrochem. Soc.*, vol. 166, no. 13, pp. F990–F995, 2019, doi: 10.1149/2.0931913jes.

[161] T. Matsui, R. Kishida, J.-Y. Kim, H. Muroyama, and K. Eguchi, “Performance Deterioration of Ni–YSZ Anode Induced by Electrochemically Generated Steam in Solid Oxide Fuel Cells,” *J. Electrochem. Soc.*, vol. 157, no. 5, p. B776, 2010, doi: 10.1149/1.3336830.

[162] M. Chen, X. Sun, C. Chatzichristodoulou, S. Koch, P. V. Hendriksen, and M. B. Mogensen, “Thermoneutral Operation of Solid Oxide Electrolysis Cells in Potentiostatic Mode,” *ECS Trans.*, vol. 78, no. 1, pp. 3077–3088, May 2017, doi: 10.1149/07801.3077ecst.

[163] M. Trini, A. Hauch, S. De Angelis, X. Tong, P. V. Hendriksen, and M. Chen, “Comparison of microstructural evolution of fuel electrodes in solid oxide fuel cells and electrolysis cells,” *J. Power Sources*, vol. 450, Feb. 2020, doi: 10.1016/j.jpowsour.2019.227599.

[164] M. Yu, X. Tong, B. R. Sudireddy, and M. Chen, “Performance and Durability of Reversible Solid Oxide Cells with Nano-electrocatalysts Infiltrated Electrodes,” *JOM*, vol. 74, no. 12, pp. 4495–4505, Dec. 2022, doi: 10.1007/s11837-022-05540-5.

[165] S. Nuggehalli Sampathkumar *et al.*, “Degradation study of a reversible solid oxide cell (rSOC) short stack using distribution of relaxation times (DRT) analysis,” *Int. J. Hydrogen Energy*, vol. 47, no. 18, pp. 10175–10193, Feb. 2022, doi: 10.1016/j.ijhydene.2022.01.104.

[166] M. Riegraf *et al.*, “Reversible Long-Term Operation of a MK35x Electrolyte-Supported Solid Oxide Cell-Based Stack,” *J. Electrochem. Soc.*, vol. 171, no. 10, p. 104505, Oct. 2024, doi: 10.1149/1945-7111/ad8036.

[167] J. Aicart, S. Di Iorio, M. Petitjean, P. Giroud, G. Palcoux, and J. Mougin, “Transition Cycles during Operation of a Reversible Solid Oxide Electrolyzer/Fuel Cell (rSOC) System,” *Fuel Cells*, vol. 19, no. 4, pp. 381–388, 2019, doi: 10.1002/fuce.201800183.

[168] Ro. Peters *et al.*, “Long-Term Experience with a 5/15kW-Class Reversible Solid Oxide Cell System,” *J. Electrochem. Soc.*, vol. 168, no. 1, p. 014508, Jan. 2021, doi: 10.1149/1945-7111/abdc79.

[169] D. M. Silva-Mosqueda, F. Elizalde-Blancas, D. Pumiglia, F. Santoni, C. Boigues-Muñoz, and S. J. McPhail, “Intermediate temperature solid oxide fuel cell under internal reforming: Critical operating conditions, associated problems and their impact on the performance,” *Appl. Energy*, vol. 235, pp. 625–640, Feb. 2019, doi: 10.1016/j.apenergy.2018.10.117.

[170] M. A. Laguna-Bercero, Ed., *High Temperature Electrolysis*, vol. 95. in Lecture Notes in Energy, vol. 95. Cham: Springer International Publishing, 2023. doi: 10.1007/978-3-031-22508-6.

[171] F. R. Bianchi, A. Baldinelli, L. Barelli, G. Cinti, E. Audasso, and B. Bosio, “Multiscale modeling for reversible solid oxide cell operation,” *Energies (Basel).*, vol. 13, no. 19, Oct. 2020, doi: 10.3390/en13195058.

[172] A. Alzahrani, I. Dincer, and X. Li, “A performance assessment study on solid oxide fuel cells for reduced operating temperatures,” *Int. J. Hydrogen Energy*, vol. 40, no. 24, pp. 7791–7797, Jun. 2015, doi: 10.1016/j.ijhydene.2014.11.115.

[173] M. Ni, M. K. H. Leung, and D. Y. C. Leung, “A modeling study on concentration overpotentials of a reversible solid oxide fuel cell,” *J. Power Sources*, vol. 163, no. 1 SPEC. ISS., pp. 460–466, Dec. 2006, doi: 10.1016/j.jpowsour.2006.09.024.

[174] S. Youcef, Z. Bariza, H. Ben Moussa, Y. Sahli, B. Zitouni, and H. Ben-Moussa, “Solid Oxide Fuel Cell Thermodynamic Study,” 2017. [Online]. Available: https://www.researchgate.net/publication/321851052

[175] I. Celik, S. R. Pakalapati, and M. D. Salazar-Villalpando, “Theoretical calculation of the electrical potential at the electrode/electrolyte interfaces of solid oxide fuel cells,” *J. Fuel Cell Sci. Technol.*, vol. 2, no. 4, pp. 238–245, Nov. 2005, doi: 10.1115/1.2039956.

[176] Y. Sun *et al.*, “Solid oxide electrolysis cell under real fluctuating power supply with a focus on thermal stress analysis,” *Energy*, vol. 261, Dec. 2022, doi: 10.1016/j.energy.2022.125096.

[177] M. Naeij, A. Bahari, H. Rajaei Litkohi, and M. Soleimani Moghaddam, “The role of cerium-based metal-organic frameworks in enhancing palladium nanoparticles for formic acid electrooxidation,” *Int. J. Hydrogen Energy*, vol. 156, Aug. 2025, doi: 10.1016/j.ijhydene.2025.150438.

[178] M. Soleimani Moghaddam, A. Bahari, and H. Rajaei Litkohi, “Designing and modeling fuel cells made of mixed transition metal dichalcogenide and carbon-based nanostructure electrodes for renewable energy storage,” *J. Power Sources*, vol. 604, Jun. 2024, doi: 10.1016/j.jpowsour.2024.234514.

[179] C. Yang, Z. Li, Y. Wang, H. Miao, and J. Yuan, “Multiphysics analysis of flow uniformity and stack/manifold configuration in a kilowatt-class multistack solid oxide electrolysis cell module,” *Energy*, vol. 307, Oct. 2024, doi: 10.1016/j.energy.2024.132627.

[180] G. Min, S. Choi, and J. Hong, “A review of solid oxide steam-electrolysis cell systems: Thermodynamics and thermal integration,” Dec. 15, 2022, *Elsevier Ltd*. doi: 10.1016/j.apenergy.2022.120145.

[181] D. Sánchez, A. Muñoz, and T. Sánchez, “An assessment on convective and radiative heat transfer modelling in tubular solid oxide fuel cells,” *J. Power Sources*, vol. 169, no. 1, pp. 25–34, Jun. 2007, doi: 10.1016/j.jpowsour.2007.01.076.

[182] Y. N. Magar and R. M. Manglik, “Modeling of convective heat and mass transfer characteristics of anode-supported planar solid oxide fuel cells,” *J. Fuel Cell Sci. Technol.*, vol. 4, no. 2, pp. 185–193, May 2007, doi: 10.1115/1.2713781.

[183] J. H. Lienhard, “A Heat Transfer Textbook Fifth Edition.” [Online]. Available: http://ahtt.mit.edu

[184] YUNUS A. ÇENGEL and AFSHIN J. GHAJAR, “Heat and mass transfer,” 2015.

[185] S. Ma, G. Loreti, L. Wang, F. Maréchal, J. Van herle, and C. Dong, “Comparison and optimization of different fuel processing options for biogas-fed solid-oxide fuel cell plants,” *Int. J. Hydrogen Energy*, vol. 47, no. 1, pp. 551–564, 2022, doi: 10.1016/j.ijhydene.2021.10.025.

[186] L. Del Zotto, A. Monforti Ferrario, A. Hatunoglu, A. Dell’era, S. McPhail, and E. Bocci, “Experimental procedures & first results of an innovative solid oxide fuel cell test rig: Parametric analysis and stability test,” *Energies (Basel).*, vol. 14, no. 8, pp. 1–19, 2021, doi: 10.3390/en14082038.

[187] IEC, “IEC 62282-7-2:2021 Fuel cell technologies - Part 7-2: Test methods - Single cell and stack performance tests for solid oxide fuel cells (SOFCs),” pp. 21–22, 2021.

[188] U.S. Department of Energy, “Fuel Cell Handbook (7th edition),” 2004. doi: 10.1016/s0031-9422(00)82398-5.

[189] W. Winkler and P. Nehter, *Modeling Solid Oxide Fuel Cells Methods, Procedures and Techniques - Chapter 2 - Thermodynamics of Fuel Cells*. Springer, 2008.

[190] F. Maschinenbau, “Modellierung von Wasser-und Energieverbräuchen in Haushalten.”

[191] N. Pflugradt, P. Stenzel, L. Kotzur, and D. Stolten, “LoadProfileGenerator: An Agent-Based Behavior Simulation for Generating Residential Load Profiles,” *J. Open Source Softw.*, vol. 7, no. 71, p. 3574, Mar. 2022, doi: 10.21105/joss.03574.

[192] I. Renewable Energy Agency, *RENEWABLE POWER GENERATION COSTS IN 2023 2 R E N E WAB LE P OWE R G E N E R ATI O N COS TS I N 202 3*. 2024. [Online]. Available: www.irena.org

[193] “Projected Costs of Generating Electricity,” 2020.

[194] T. Huld, R. Müller, and A. Gambardella, “A new solar radiation database for estimating PV performance in Europe and Africa,” *Solar Energy*, vol. 86, no. 6, pp. 1803–1815, Jun. 2012, doi: 10.1016/j.solener.2012.03.006.

[195] S. Zong, X. Zhao, L. L. Jewell, Y. Zhang, and X. Liu, “Advances and challenges with SOEC high temperature co-electrolysis of CO2/H2O: Materials development and technological design,” Sep. 01, 2024, *Elsevier Ltd*. doi: 10.1016/j.ccst.2024.100234.

[196] F. Marino *et al.*, “Performance Evaluation of an Anode-Supported SOFC Short-Stack Operating with Different Fuel Blends as Stationary-CHP System,” *J. Electrochem. Soc.*, vol. 171, no. 5, p. 054511, May 2024, doi: 10.1149/1945-7111/ad4783.

[197] J. Andersson and S. Grönkvist, “Large-scale storage of hydrogen,” May 03, 2019, *Elsevier Ltd*. doi: 10.1016/j.ijhydene.2019.03.063.

[198] “DOE Hydrogen and Fuel Cells Program Record 9013: Energy requirements for hydrogen gas compression and liquefaction as related to vehicle storage needs,” 2009. [Online]. Available: http://www.eere.energy.gov/hydrogenandfuelcells/hydrogen_publications.html#h2_storage

[199] “CLEAN HYDROGEN JOINT UNDERTAKING Strategic Research and Innovation Agenda 2021 – 2027”.

[200] J. Apt, A. Newcomer, L. B. Lave, S. Douglas, and L. Morris Dunn, “An Engineering-Economic Analysis of Syngas Storage Final Report,” 2008. [Online]. Available: www.netl.doe.gov

[201] H. K. Shin and S. K. Ha, “A Review on the Cost Analysis of Hydrogen Gas Storage Tanks for Fuel Cell Vehicles,” Jul. 01, 2023, *Multidisciplinary Digital Publishing Institute (MDPI)*. doi: 10.3390/en16135233.

[202] P. Muthukumar *et al.*, “Review on large-scale hydrogen storage systems for better sustainability,” Oct. 15, 2023, *Elsevier Ltd*. doi: 10.1016/j.ijhydene.2023.04.304.

[203] V. Saarinen *et al.*, “Design, manufacturing, and operation of movable 2 × 10 kW size rSOC system,” *Fuel Cells*, vol. 21, no. 5, pp. 477–487, Oct. 2021, doi: 10.1002/fuce.202100021.

[204] J. Fleig, “Solid Oxide Fuel Cell Cathodes: Polarization Mechanisms and Modeling of the Electrochemical Performance,” 2003. doi: 10.1146/annurev.matsci.33.022802.093258.

[205] S. B. Adler, “Factors governing oxygen reduction in solid oxide fuel cell cathodes,” *Chem. Rev.*, vol. 104, no. 10, pp. 4791–4843, Oct. 2004, doi: 10.1021/cr020724o.

[206] Evgenij Barsoukov, “Impedance Spectroscopy Theory, Experiment, and Applications,” Wiley, 2005. doi: 10.1002/0471716243.fmatter.

[207] D. D. MacDonald, “Reflections on the history of electrochemical impedance spectroscopy,” in *Electrochimica Acta*, Jan. 2006, pp. 1376–1388. doi: 10.1016/j.electacta.2005.02.107.

[208] Q. Shao *et al.*, “Performance evolution analysis of solid oxide electrolysis cells operating at high current densities,” *Int. J. Hydrogen Energy*, vol. 57, pp. 709–716, Feb. 2024, doi: 10.1016/j.ijhydene.2024.01.096.

[209] X. Sun, P. V. Hendriksen, M. B. Mogensen, and M. Chen, “Degradation in Solid Oxide Electrolysis Cells During Long Term Testing,” *Fuel Cells*, vol. 19, no. 6, pp. 740–747, Dec. 2019, doi: 10.1002/fuce.201900081.

[210] T. Le Cheng *et al.*, “Oxidation of nickel in solid oxide cells during electrochemical operation: Experimental evidence, theoretical analysis, and an alternative hypothesis on the nickel migration,” *J. Power Sources*, vol. 569, Jun. 2023, doi: 10.1016/j.jpowsour.2023.232991.

[211] M. Hubert, J. Laurencin, P. Cloetens, B. Morel, D. Montinaro, and F. Lefebvre-Joud, “Impact of Nickel agglomeration on Solid Oxide Cell operated in fuel cell and electrolysis modes,” *J. Power Sources*, vol. 397, pp. 240–251, Sep. 2018, doi: 10.1016/j.jpowsour.2018.06.097.

[212] Z. Jiao *et al.*, “Integrated 3D modeling unravels the measures to mitigate nickel migration in solid oxide fuel/electrolysis cells,” *J. Mater. Chem. A Mater.*, vol. 12, no. 1, pp. 162–173, Nov. 2023, doi: 10.1039/d3ta06563d.

[213] Y. Wang *et al.*, “Ni migration of Ni-YSZ electrode in solid oxide electrolysis cell: An integrated model study,” *J. Power Sources*, vol. 516, Dec. 2021, doi: 10.1016/j.jpowsour.2021.230660.

[214] Á. Triviño-Peláez, D. Cademartori, M. Hubert, L. Rorato, M. Prioux, and J. Laurencin, “Modelling the impact of Ni migration and coarsening on the Ni-YSZ electrodes performances based on three-dimensional microstructures,” *Electrochim. Acta*, vol. 520, Apr. 2025, doi: 10.1016/j.electacta.2025.145791.

[215] H. Wang *et al.*, “Performance and Thermal Stress Evaluation of Full-Scale SOEC Stack Using Multi-Physics Modeling Method,” *Energies (Basel).*, vol. 16, no. 23, Dec. 2023, doi: 10.3390/en16237720.

[216] K. Lim, Y. Kim, H. Salihi, and H. Ju, “Integrated modeling of electrochemical, thermal, and structural behavior in solid oxide electrolysis cells,” *Int. J. Heat Mass Transf.*, vol. 224, Jun. 2024, doi: 10.1016/j.ijheatmasstransfer.2024.125235.

[217] Z. Liang, S. Chen, M. Ni, J. Wang, and M. Li, “A novel control strategy to neutralize internal heat source within solid oxide electrolysis cell (SOEC) under variable solar power conditions,” *Appl. Energy*, vol. 371, Oct. 2024, doi: 10.1016/j.apenergy.2024.123669.

[218] Y. Wang, A. Banerjee, and O. Deutschmann, “Dynamic behavior and control strategy study of CO2/H2O co-electrolysis in solid oxide electrolysis cells,” *J. Power Sources*, vol. 412, pp. 255–264, Feb. 2019, doi: 10.1016/j.jpowsour.2018.11.047.

[219] H. Chen, T. Wu, S. Luo, Y. Wang, and X. Xu, “Operating strategy investigation of a solid oxide electrolysis cell under large scale transient electrical inputs,” *Energy Convers. Manag.*, vol. 294, Oct. 2023, doi: 10.1016/j.enconman.2023.117596.

[220] L. Jin, A. Monforti Ferrario, V. Cigolotti, and G. Comodi, “Evaluation of the impact of green hydrogen blending scenarios in the Italian gas network: Optimal design and dynamic simulation of operation strategies,” *Renewable and Sustainable Energy Transition*, vol. 2, no. March, p. 100022, 2022, doi: 10.1016/j.rset.2022.100022.

[221] Gareth. James, Daniela. Witten, Trevor. Hastie, and Robert. Tibshirani, *An introduction to statistical learning : with applications in R*. Springer : Springer Science+Business Media, 2017.

[222] Sebastian. Raschka and Vahid. Mirajalili, *Python machine learning : machine learning and deep learning with Python, scikit-learn, and TensorFlow*. Packt Publishing, 2018.

[223] G. Chicco, “Overview and performance assessment of the clustering methods for electrical load pattern grouping,” *Energy*, vol. 42, no. 1, pp. 68–80, 2012, doi: 10.1016/j.energy.2011.12.031.

[224] C. Flath, D. Nicolay, T. Conte, C. Van Dinther, and L. Filipova-Neumann, “Cluster analysis of smart metering data: An implementation in practice,” *Business and Information Systems Engineering*, vol. 4, no. 1, pp. 31–39, 2012, doi: 10.1007/s12599-011-0201-5.

[225] E. C. Bobric, G. Cartina, and G. Grigoraş, “Clustering techniques in load profile analysis for distribution stations,” *Advances in Electrical and Computer Engineering*, vol. 9, no. 1, pp. 63–66, 2009, doi: 10.4316/aece.2009.01011.

[226] I. Prahastono, D. King, and C. S. Özveren, “A review of electricity load profile classification methods,” in *Proceedings of the Universities Power Engineering Conference*, 2007, pp. 1187–1191. doi: 10.1109/UPEC.2007.4469120.

[227] L. Guivant Viola, “Segmentation of household load-profiles with K-means clustering algorithm,” 2016. [Online]. Available: https://www.researchgate.net/publication/304717810

[228] G. Jeon and Y. Kim, “Model-based fault detection algorithm for liquid hydrogen refueling system using CUSUM method,” *Comput. Chem. Eng.*, vol. 192, Jan. 2025, doi: 10.1016/j.compchemeng.2024.108878.

[229] M. Benedetti, F. Bonfà, V. Introna, A. Santolamazza, and S. Ubertini, “Real time energy performance control for industrial compressed air systems: Methodology and applications †,” *Energies (Basel).*, vol. 12, no. 20, Oct. 2019, doi: 10.3390/en12203935.

[230] M. Shen, F. Ai, H. Ma, H. Xu, and Y. Zhang, “iScience Progress and prospects of reversible solid oxide fuel cell materials,” 2006, doi: 10.1016/j.isci.

[231] P. Zhu *et al.*, “Ni coarsening and performance attenuation prediction of biomass syngas fueled SOFC by combining multi-physics field modeling and artificial neural network,” *Appl. Energy*, vol. 322, Sep. 2022, doi: 10.1016/j.apenergy.2022.119508.

[232] Y. Wang, C. Wu, Q. Du, M. Ni, K. Jiao, and B. Zu, “Morphology and performance evolution of anode microstructure in solid oxide fuel cell: A model-based quantitative analysis,” *Applications in Energy and Combustion Science*, vol. 5, Mar. 2021, doi: 10.1016/j.jaecs.2020.100016.

[233] B. Hou, C. C. Wang, X. Cui, and Y. Chen, “Chromium deposition and poisoning of La2NiO4 cathode of solid oxide fuel cell,” *R. Soc. Open Sci.*, vol. 5, no. 10, Oct. 2018, doi: 10.1098/rsos.180634.

[234] L. Zhou, J. H. Mason, W. Li, and X. Liu, “Comprehensive review of chromium deposition and poisoning of solid oxide fuel cells (SOFCs) cathode materials,” Dec. 01, 2020, *Elsevier Ltd*. doi: 10.1016/j.rser.2020.110320.

[235] H. Choi *et al.*, “Unveiling the high-temperature degradation mechanism of solid oxide electrolysis cells through direct imaging of nanoscale interfacial phenomena,” *Energy Environ. Sci.*, vol. 17, no. 15, pp. 5410–5420, May 2024, doi: 10.1039/d4ee00896k.

[236] C. E. Frey, Q. Fang, D. Sebold, L. Blum, and N. H. Menzler, “A Detailed Post Mortem Analysis of Solid Oxide Electrolyzer Cells after Long-Term Stack Operation,” *J. Electrochem. Soc.*, vol. 165, no. 5, pp. F357–F364, 2018, doi: 10.1149/2.0961805jes.

[237] J. Laurencin *et al.*, “Degradation mechanism of La0.6Sr0.4Co0.2Fe0.8O3-δ/Gd0.1Ce0.9O2-δ composite electrode operated under solid oxide electrolysis and fuel cell conditions,” *Electrochim. Acta*, vol. 241, pp. 459–476, Jul. 2017, doi: 10.1016/j.electacta.2017.05.011.

[238] A. Hauch *et al.*, “A Decade of Solid Oxide Electrolysis Improvements at DTU Energy,” *ECS Trans.*, vol. 75, no. 42, pp. 3–14, Jan. 2017, doi: 10.1149/07542.0003ecst.

[239] J. Kim *et al.*, “Degradation mechanism of electrolyte and air electrode in solid oxide electrolysis cells operating at high polarization,” *Int. J. Hydrogen Energy*, vol. 38, no. 3, pp. 1225–1235, Feb. 2013, doi: 10.1016/j.ijhydene.2012.10.113.

[240] S. Shiva Kumar and V. Himabindu, “Hydrogen production by PEM water electrolysis – A review,” Dec. 01, 2019, *KeAi Communications Co.* doi: 10.1016/j.mset.2019.03.002.

[241] M. Lang, S. Raab, M. S. Lemcke, C. Bohn, and M. Pysik, “Long-Term Behavior of a Solid Oxide Electrolyzer (SOEC) Stack ▲,” *Fuel Cells*, vol. 20, no. 6, pp. 690–700, Dec. 2020, doi: 10.1002/fuce.201900245.

[242] S. Y. Gómez and D. Hotza, “Current developments in reversible solid oxide fuel cells,” Aug. 01, 2016, *Elsevier Ltd*. doi: 10.1016/j.rser.2016.03.005.

[243] F. Wang, L. Wang, H. Zhang, L. Xia, H. Miao, and J. Yuan, “Design and optimization of hydrogen production by solid oxide electrolyzer with marine engine waste heat recovery and ORC cycle,” *Energy Convers. Manag.*, vol. 229, Feb. 2021, doi: 10.1016/j.enconman.2020.113775.

The PhD research includes three publications, two of which have been accepted and published in international journals, and one manuscript accepted with minor revisions, thus currently under review. These works are cited in the text:

I. **Francesco Marino**, Davide Pumiglia, Francesca Santoni, Maria Anna Murmura, Luca Simonetti, Viviana Cigolotti, Giulia Monteleone, Elio Jannelli. "Evaluation of SOEC Segmented Performance through Experimental Localized Fuel Electrode Multisampling Technique." Journal of Power Sources 660 (2025): 238573. https://doi.org/10.1016/j.jpowsour.2025.238573

II. **Francesco Marino**, Andrea Monforti Ferrario, Francesca Santoni, Antonio Alfano, Matti Noponen, Raphael Neubauer, Viviana Cigolotti, Elio Jannelli. "Performance Evaluation of an Anode-Supported SOFC Short-Stack Operating with Different Fuel Blends as Stationary-CHP System." Journal of The Electrochemical Society 171, no. 5 (2024): 054511. https://doi.org/10.1149/1945-7111/ad4783

III. **Francesco Marino**, Gabriele Loreti, Massimiliano Della Pietra, Viviana Cigolotti, Giulia Monteleone, Elio Jannelli. "Experimental Investigation of Reversible Solid Oxide Fuel Cells Coupled with a Domestic Load and a Photovoltaic System for Seasonal Storage Purposes." Submitted to International Journal of Hydrogen Energy and currently under review after a minor revision was assigned

A supplementary manuscript detailing the operational performance of the system exceeding 10 kW is currently under preparation.

Participations in conferences and contributions:

- **Francesco Marino**, Massimiliano Della Pietra, Andrea Monforti Ferrario, Francesca Santoni, Viviana Cigolotti, Elio Jannelli. "Scenario Evaluation of Reversible Solid Oxide Cells Integrated with Local Renewable Energy Sources: Assessment of Different Coupling Applications." ECS Transactions 111, no. 6 (2023): 393–411. https://doi.org/10.1149/11106.0393ecst

- **Francesco Marino**, Lorenzo Arcidiacono, Francesca Santoni, Andrea Monforti Ferrario, Luca Simonetti, Antonio Scotini, Arda Hatunoglu. "Validation of Solid Oxide Fuel Cell Short Stack Test Bench in SO-FREE Project." Proceedings of EFC23 – European Fuel Cell and Hydrogen, Piero Lunghi Conference, Capri, Italy, 13 – 15 September 2023.

- **Francesco Marino**, Francesca Santoni, Andrea Monforti Ferrario, Michał Wierzbicki, Piotr Ostrowski. "Performance Evaluation of Two SOFC Stack Technologies Operated Under CHP System Relevant Conditions: Replicability Study." Proceedings of EFC23 – European Fuel Cell and Hydrogen, Piero Lunghi Conference, Capri, Italy, 13 – 15 September 2023.

- **Francesco Marino**, Davide Pumiglia, Francesca Santoni, Maria Anna Murmura, Luca Simonetti, Viviana Cigolotti, Elio Jannelli. "In-Depth Analysis of a SOEC through Localized Fuel Electrode

Multisampling Technique." Proceedings of EFCF 2024 – 16th European SOFC & SOE Forum, Lucerne, Switzerland, 2 – 5 July 2024.

Participations in summer schools:

Second StoRIES Summer School 2024: Hybrid Energy Storage and Application-Oriented Solutions in Europe. Rome, Italy, 3 – 6 June 2024.